Pollutant Transport and Dispersion in Large Indoor Spaces: A Status Report for the Large Space Effort of the Interiors Project

A.J. Gadgil, E.U. Finlayson, M.L. Fischer, P.N. Price,
T.L. Thatcher, M.J. Craig, K.H. Hong, J. Housman,
C.A. Schwalbe, D. Wilson, J.E. Wood, and R.G. Sextro

Environmental Energy Technologies Division
Indoor Environment Department
Lawrence Berkeley National Laboratory
Berkeley, CA 94720

June 2000

TABLE OF CONTENTS

I. INTRODUCTION AND PROJECT OVERVIEW

It is of scientific and practical interest to understand the transient transport and dispersion of airborne pollutants in large indoor spaces (such as atriums, auditoriums, theaters, airport lounges, and subway stations). The problem is of scientific interest since it addresses an airflow and pollutant transport regime (low Reynolds number turbulent mixed-convection in enclosures) that has not been fully studied or well characterized. The problem is of practical interest since improved understanding will facilitate the assessment of the risk to occupants from an accidental release of airborne toxic pollutant in the space, and identification and evaluation of ways to reduce occupant exposures in the event of such release.

Scientific research on air flows and pollutant transport in large interior spaces is an emerging field. The literature is relatively sparse compared to, say, pollutant transport processes outdoors in atmospheric boundary layers. While there are many experimental and computational studies of air flow and temperature distribution in indoor spaces, most of them focused on occupant comfort. In these studies, mostly the long term average air flow patterns have been of interest. For non-isothermal flows, the attention has been focused on achieving comfort conditions, rather than on transporting thermal energy as a scalar variable. We present a summary of the published research through 1997 (when we initiated our research planning) in Table 1. References at the end of this section refer to papers cited in Table 1.

Only a few researchers have investigated pollutant transport, and those have been mostly limited to studies of steady pollutant sources (so transient effects are not investigated), and sparse spatial sampling (so spatial distribution of the pollutant cannot be measured in detail). However, with open-path rapid optical scanning instrumentation, and inversion of the collected data with computed tomography (as reported here), we now can experimentally measure rapid dispersion of transient plumes in indoor spaces in the presence of realistic ventilation rates.

An airborne pollutant released in the space is transported by the flow of air (advection), and also disperses in the opposite direction of concentration gradients (diffusion). The air flow in large spaces is driven primarily by mechanical ventilation, and thermal buoyancy caused by surface temperature differences and heat sources. Natural ventilation and infiltration are negligible or secondary effects in most circumstances. Based on the floor area and mechanical ventilation rate, the Reynolds number characterizing the air flow is of the order of 10^6. Thus the flow is in the turbulent regime. The Rayleigh number characterizes the strength of buoyancy forces relative to viscous forces in natural convection. In most indoor spaces of interest, this can be of the order of 10^{12} leading to buoyancy-induced turbulence even in the absence of mechanical ventilation.

This report describes the experimental and computational research conducted under the Large Space project in the Indoor Environment Department from mid-1998 through January 2000.

The transport of a pollutant (or its surrogate: a tracer gas) can be measured throughout the space by several commonly used research instruments (e.g., pump-and-tube samplers). However, these

measurements techniques are relatively slow, and highly intrusive, which can disturb the air flows and pollutant concentrations that they aim to measure. In **Sections II and III**, we report on a novel and powerful measurement method for airborne tracer gas concentrations that is both rapid and non-intrusive.

Under some circumstances, the dispersion of pollutants in a large indoor space can be investigated rapidly and accurately by conducting experiments with scaled-down models. In **Section IV**, we report on a successful effort to study the dispersion of a neutrally-buoyant pollutant in an isothermal large indoor space by investigating the dispersion of dye in water in a scale model. Postprocessing of digital video and still images of the dye concentration allowed us to obtain qualitative and quantitative information that assisted with the design of the full scale experiments, as well as provided early verification of the accuracy of our computational approach (summarized below).

The air velocities throughout the space can also be determined by solving the differential equations governing the motion of air: the Navier-Stokes equations, and the equations of continuity and conservation of thermal energy. Under all practical indoor conditions, the air can be treated as an incompressible fluid, and the thermal buoyancy effects from air temperature differences can be accommodated using the Boussinesq approximation. An appropriate model of turbulence must be incorporated into the governing equations for the air flow. Depending on the relative density of the pollutant-bearing air, it can be treated as a passive or active scalar. In the latter case, buoyancy effects must be taken into account in the governing equations for pollutant transport. In the period covered by this report, we limited our investigations, described in **Section V**, to passive scalar pollutants, i.e., those which are sufficiently dilute to neglect buoyancy effects on their transport and dispersion.

Even under the simplest of practical situations, solving the Navier-Stokes equations requires large computational resources. Depending on the algorithms and approximations introduced in the solution process, the results of the calculations will contain errors of various magnitudes. These can be acceptably small, or unacceptably large. Comparing CFD predictions to experimental data offers an opportunity to assess the effects of modeling decisions.

Once verified against high quality experimental data, such mathematical models of air flow and pollutant transport offer the only practical means of exploring the details of pollutant dispersion in realistic complex occupied indoor spaces without excessively disrupting the occupants. The computational approach also allows effective exploration of alternate methods for pollutant containment (air curtains, alterations in ventilation inlet and outlet positions and flow rates) that would be prohibitively expensive, slow, or simply impossible if based solely on experimental investigation.

REFERENCES

Baughman, A. V., Gadgil, A. J. and Nazaroff, W. W., 1994, "Mixing of a point source pollutant by natural convection flow within a room." *Indoor Air **4**,* pp. 114-122.

Bhattacharyya R. and Todd, L. A., 1997, "Spatial and temporal visualization of gases and vapors in air using computed tomography. Numerical studies." *Am. Occup. Hyg. **41**,* pp. 105-122.

Chen, Q. and Chao, N.-T., 1996, "Prediction of buoyant plume and displacement ventilation with different turbulence models." *Proceedings of Indoor Air '96* **1**, pp. 782-792, Nagoya.

Chen, Q., 1997, "Computational fluid dynamics for HVAC: Successes and failures." *ASHRAE Trans.* **103(l),** pp. 178-187.

Chow, W. K. and Fung, W. Y., 1997, "Experimental studies on the airflow characteristics of spaces with mechanical ventilation." *ASHRAE Trans.* **103(l),** pp**.** 31-41.

Chow, W. K., 1995, "Ventilation design: Use of computational fluid dynamics as a study tool." *Building Serv. Eng. Res. Technol.* **16**, pp. 63-76.

Cook, M. J. and Lomas, K. J., 1998, "Buoyancy-driven displacement ventilation flows: Evaluation of two eddy viscosity turbulence models for prediction." *Building Serv. Eng. Res. Technol.* **19**, pp. 15-2 1.

Drescher, A. C., Gadgil, A. J., Price, P. N. and Nazaroff, W. W., 1996, "Novel approach for tomographic reconstruction of gas concentration distributions in air: Use of smooth basis functions; and simulated annealing." *Atmospheric Environment* **30**, pp. 929-940.

Drescher, A. C., Lobascio, C., Gadgil, A. J. and Nazaroff, W. W., 1995, "Mixing of a point-source indoor pollutants by forced convection." *Indoor Air* **5**, pp. 204-214.

Drescher, A. C., Park, D. Y., Yost, M. G., Gadgil, A. J., Levine, S. P. and Nazaroff, W. W., 1996, "Stationary and time dependent tracer-gas concentration measured by OPFTIR remote sensing and SBFM computed tomography." *Atmospheric Environment* **31**, pp. 727-740.

Drivas, P. J., Valberg, P. A., Murphy, B. L. and Wilson R., 1996, "Modeling indoor air exposure from short-term point source releases." *Indoor Air* **6***,* pp. 271-277.

Fissors, A. A. and Liebecq, G. A., 1991, "A simple empirical model for predicting velocity distributions and comfort in a large slot-ventilated space" *ASHRAE Trans.* **97(2),** pp. 1087-1095.

Furtaw, E. J., Jr. Pandian, M. D., Nelson, D.R. and Behar, J. V., 1996, "Modeling indoor air concentrations near emission sources in imperfectly mixed rooms." J *Air & Waste Manage. Assoc.* **46**, pp. 861-868.

Grimitlyn, M. 1. and Pozin, G. M., 1993, "Fundamentals of optimum air distribution in ventilated spaces." *ASHRAE Trans. **99(1)**,* pp. 1128-1138 Haghighat, F., Wang, J. C. Y. and

Jiang, Z., 1990, "Three-dimensional analysis of airflow pattern and contaminant dispersion in a ventilated two-zone enclosure." *ASHRAE Trans.* **96(1)**, pp. 831-839.

Hassani, V. T., Malmstrom, T. and Kirkpatrick, A. T., 1993, "Indoor thermal environment of cold air distribution systems.*"ASHRAE Trans.* **99(1)**, pp. 1359-1364.

Heber, A. J. and Boon, C. R., 1993, "Air velocity characteristics in an experimental livestock building with nonisothermal jet ventilation." *ASHRAE Trans.* **99(l)***,* pp. 1139-1151.

Heiselberg, P., 1996, "Room air and contaminant distribution in mixing ventilation." *ASHRAE Trans.* **102(2)***,* pp. 332-339.

Hosni, M. H., Abu-El-Hassan, M. B. and Miller, P. L., 1996, "Airflow characteristics of jet expansion for non-isothermal flow conditions." *ASHRAE Trans.* **102(2)***,* pp. 301-312.

Jin, Y. and Ogilvie, J. R., 1992, "Isothermal airflow characteristics in a ventilated room with a slot inlet opening." *ASHRAE Trans. **98(2)**,* pp. 296-306.

Klote, J. H., 1997, "Simulating the effects of HVAC-induced airflow from slot diffusers on detector response." *ASHRAE Trans.* **103(2)***,* pp. 418-435.

Klote, J. H., 1997, "Prediction of smoke movement in atria: Part I-Physical concepts." *ASHRAE Trans.* **103(2)***,* pp. 545-553.

Klote, J. H., 1997, "Prediction of smoke movement in atria: Part II-Application to smoke management." *ASHRAE Trans.* **103(2)***,* pp. 534-544.

Miller S. L., Leiserson, K. and Nazaroff, W. W., 1997, "Nonlinear least-square minimization applied to tracer gas decay for determining airflow rates in a two-zone building." *Indoor Air* **7***,* pp. 64-75.

Mizuno, T. and Warfield, M. J., 1992,"Development of three-dimensional thermal airflow analysis computer program and verification test." *ASHRAE Trans.* **98(2)** pp. 329-338.

Murakami, S., Kato, S. and Nakagawa, H., 1991, "Numerical prediction of horizontal non-isothermal 3-D jet in room based on the *k-e* model." *ASHRAE Trans.* **97(l)***,* pp. 3848.

Murakami, S., Kato, S. and Ooka, R., 1994, "Comparison of numerical predictions of horizontal nonisothermal jet in a room with three turbulence models-*k-e* EVM, ASM, and DSM." *ASHRAE Trans.* **100(2***),* pp. 697-704.

Nicas, M., 1996, "Estimation Exposure Intensity in an Imperfectly Mixed Room. " *Am. Ind Hyg. Assoc. J* **57**, pp. 542-550.

Rasouli, F. and Williams, T. A., 1995, "Application of dispersion modeling to indoor gas release scenarios." *J Air & Waste Manage. Assoc.* **45***,* pp. 191-195.

Rodes, C. E., Kamens, R. M. and Wiener, R. W., 1995, "Experimental Considerations for the Study of Contaminant Dispersion Near the Body " *Am Ind. Hyg, Assoc. J.* **56**, pp. 535-545.

Rodes, C. E., Kamens, R. M. and Wiener, R. W., 1995, "The significance and characteristics of the personal cloud on exposure assessment measurements for indoor." *Indoor Air* **2**, pp. 123-145.

Samanta, A. and Todd, L. A., 1996, "Mapping air contaminants indoor using a prototype computed tomography system." *Am. Occup. Hyg.* **40**, pp. 675-691.

Shankar, V., Davidson, L. and Olsson, E., 1995, "Numerical Investigation of Turbulent Plumes in both Ambient and Stratified Surroundings. *Indoor Air* **5**, pp. 136-146.

Shimada, M., Okuyarna, K., Okazaki, S., Asai, T., Matsukura, M. and Ishizu, Y., 1996, "Numerical simulation and experiment on the transport of fine particles in a ventilated room." *Aerosol Sci. & Tech.* **25**, pp. 242-255.

Tavakkol, S., Hosni, M. H., Miller, P. L. and Straub, H. E., 1994, "A study of isothermal throw of air jets with various room sizes and outlet configurations." *ASHRAE Trans.* **100(l),** pp. 1679-1686.

Todd, L. and Ramachandran, G., 1994, " Evaluation of algorithms for tomographic reconstruction of chemical concentrations in indoor." *Am. Ind Hyg. Assoc. J.* **55**, pp. 403-417.

Wang, J. and Ogilvie, J. R., 1996." Airflow distributions at floor level in a slot-outlet and slot-inlet ventilated room." *ASHRAE Trans.* **102(l)**, pp. 347-358.

Yaghoubi, M. A., Knappmiller, K. D. and Kirkpatrick, A. T., 1995, "Three-dimensional numerical simulation of air contamination dispersion in a room." *ASHRAE Trans.* **101(2)**, pp. 1031-1040.

Yost, M. G., Gadgil, A. J., Drescher, A. C., Zhou, Y., Simonds, M. A., Levine, S. P., Nazaroff, W. W. and Saisan, P. A., 1994, "Imaging indoor tracer-gas concentrations with computed tomography: experimental results with a remote sensing FTIR system." *Am. Ind Hyg. Assoc. J* **55,** pp. 395-402.

Zhang, J. S., Christianson, L. L. and Riskowski, G. L., 1990," Regional airflow characteristics in a mechanically ventilated room under non-isothermal conditions." *ASHRAE Trans.* **96(l)**, pp. 751-759.

Zhang, J. S., Wu, G. J. and Christianson, L. L., 1992," Full-scale experimental results on the mean and turbulent behavior of room ventilation flows." *ASHRAE Trans.* **98(2)**, pp. 307-316.

Zhivov, A., 1993, "Theory and practice of air distribution with inclined jets." *ASHRAE Trans.* **99(l)**, pp. 1152-1159.

Authors	Experiment	Calculation	Temperature (_T=T_{jet}-T_{room})	Room Size (L x W x H) (L x H) [m]	Supply Flow Rate	Room Air Supply	Room Air Exhaust	
Haghighat et al. (1990)		Flow (O) Particle(O) κ-_ model of turbulence		10.0x4.0x3.0		Infiltration Side wall slot	Ceiling slot	Two Zone Different location of exhaust and contaminant source
Heiselberg (1996)	Flow (X) Particle (O) Tracer gas (CO_2) decay method		-5.6K (cooling) 0.0K (isothermal) 6.4K (heating)	4.2x3.6x2.4	1,0, 1.5, 3.0 and 6.0 ACH	Side wall slot	Side wall slot	Local mean Age & ventilation effectiveness
Shimada et al. (1996)	Ultrasonic anemometer (flow) Laser particle counter -0.14_m polystyren latex particles (concentration)	FLUENT *k*-_ model Gravity, inertia and thermal effect is neglected	Isothermal	3.3x2.7x2.0		Ceiling slot	Side wall slot	Clean room type Effects of position & height of emission port CPU 48hr (HR735/125) 138,600 grid

Authors	Experiment	Calculation	Temperature (_T=T_{jet}-T_{room})	Room Size (L x W x H) (L x H) [m]	Supply Flow Rate	Room Air Supply	Room Air Exhaust	
Heber & Boon. (1990)	Flow (O) ultrasonic anemometer Particle (X)		T_{jet}=14.9 $T_{exhaust}$=17.7¡ C	5.88x3.33		Ceiling slot	Side wall slot	Livestock building
Jin & Ogilvie (1996)	Flow (O) Particle (X)		Isothermal	4.8x3.0	0.5-10 m/s	Side wall slot	Side wall slot	Correlation between the velocity in the occupied zone and supply jet
Zhang et al. (1990)	Flow (O) Particle (X)		_T=0.0-9.8¡C	11.5x9.1x2.1	5-10 ACH	Side wall slot	Side wall slot	Subfield modeling
Zhang et al. (1992)	Hot wire (flow) Thermocouple (temperature) Smoke titanium tetrachloride (flow visualization)		-1.3K (cooling) 0.0K (isothermal) 8.8 & 19.6K (heating)	5.5x7.3x2.4 except near the wall because of a long slot	Supply air velocity 45.5, 106, 152 m/min	Side wall slot	Side wall slot	Velocity fluctuations Turbulence intensity & kinetic energy of turbulence

Authors	Experiment	Calculation	Temperature ($\Delta T = T_{jet} - T_{room}$)	Room Size (L x W xH) (L x H) [m]	Supply Flow Rate	Room Air Supply	Room Air Exhaust	
Wang & Ogilvie (1996)	Flow (O) Particle (X)		T_{jet}=22.0 T_{room}=27-35¡C	4.9x(2.6-3.2)		Side wall slot	Side wall slot	$U_{floor\text{-}level,max} = \alpha \sqrt{R_M} + \Delta (H\_T)$
Chow (1995)		Flow (O) *k*-_ model Particle (X)	Non-isothermal	Waiting hall (61x25x20) Parking lot (40x20x4)	(1/4, 1.0, 2.0 & 4.0) x 33.4 ACH	Side wall slot	Side wall slot	CFD package -FLOVENT
Fissor & Liebecq (1991)	Flow (O) Particle (X)		Ar=-2.5-24.9	4.3x2.7 long and narrow with a high triangular roof	Re=1474-5151	Side wall slot	Side wall slot	Relation Between mean velocity of air in the occupied zone and jet velocity
Chow & Fung (1997)	Flow (O) Particle (O)		T_{jet}=20.4-22.5 T_{room}=20.6-22.7¡C	(20-76.2) x(15-25.2) x(4.7x20)	3.3-1-/9 ACH	Side wall long slot	Side wall rectang-ular slot	Any design yardstick used should correlate with the local ventilation effect

Authors	Experiment	Calculation	Temperature (˜T= T_{jet}- T_{room})	Room Size (L x W x H) (L x H) [m]	Supply Flow Rate	Room Air Supply	Room Air Exhaust	
Tavakol et al. (1994)	Flow (O) Particle (X)		Isothermal	3.7 x(3.6-11.0) x2.7	206-316 L/s	Ceiling (4way & Circular)		Jet flow characteristics
Dresher et al. (1995)	Flow (X) Paticle (O)		Maximum temperature difference in the room (0.25-1.0…C)	3.53x3.74 x2.36	Mixing pump flow rate: 6-60 m^3/hr			Time constant for mixing for a forced convection
Baughman et al. (1994)	Flow (O) Particle (X)		Maximum temperature difference in the room (0.4-1.15¡C)	3.53x3.74 x2.36				Time constant for mixing for a natural convection
Grimitlyn & Pozin (1993)	Flow (O) Particle (X)		Buoyancy effect (O)					Jet flow characteristics including wall and jet interaction
Mizuno & Warfield (1992)	Flow (O) Particle (O)	INS3D (with buoyance effect and dispersion including obstruction		Airplane Cabin		Ceiling mounted nozzle	Inboard, outboard exhaust & lower lobe grill	Originally developed by NASA

Authors	Experiment	Calculation	Temperature (˜T= T_{jet}-T_{room})	Room Size (LxWxH) (LxH) [m]	Supply Flow Rate	Room Air Supply	Room Air Exhaust	
Chen (1997) cf. Chen & Chao (1996)	Flow (O) Particle (O)	Flow (O) Particle (O) k-_ and RNG	Buoyancy effect (O) 530W heat source	5.6x3.0x3.2	5 ACH	Side wall rectangular slot	Side wall rectangular slot	Comparison **of** turbulence modeling
Shankar et al. (1995)		Flow (O) Particle (X) modified k-_ model & RSV	Buoyancy effect (O) k-_ model modified by buoyancy production					Comparison of turbulence modeling Thermal plume
Miller et al. (1997)		Theory Flow (X) Particle (O)						Two-zone
Drivas et al. (1996)		Diffusion equation Flow (X) Particle (O)						Short-term Exposure Reflection B.C.
Rasouli & Williams (1995)		Flow (X) Particle (O)						Dispersion analytic sol.
Nicas (1996)		Theory (imperfectly mixed room)						

Authors	Experiment	Calculation	Temperature (˜T= T_{jet}-T_{room})	Room Size (LxWxH) (LxH) [m]	Supply Flow Rate	Room Air Supply	Room Air Exhaust	
Chen (1997) cf. Chen & Chao (1996)	Flow (O) Particle (O)	Flow (O) Particle (O) k-_ and RNG	Buoyancy effect (O) 530W heat source	5.6x3.0x3.2	5 ACH	Side wall rectangular slot	Side wall rectangular slot	Comparison **of** turbulence modeling
Shankar et al. (1995)		Flow (O) Particle (X) modified k-_ model & RSV	Buoyancy effect (O) k-_ model modified by buoyancy production					Comparison of turbulence modeling Thermal plume
Miller et al. (1997)		Theory Flow (X) Particle (O)						Two-zone
Drivas et al. (1996)		Diffusion equation Flow (X) Particle (O)						Short-term Exposure Reflection B.C.
Rasouli & Williams (1995)		Flow (X) Particle (O)						Dispersion analytic sol.
Nicas (1996)		Theory (imperfectly mixed room)						

Authors	Experiment	Calculation	Temperature (˜T= T_{jet}-T_{room})	Room Size (LxWxH) (LxH) [m]	Supply Flow Rate	Room Air Supply	Room Air Exhaust	
Furtaw et al. (1996)	Flow (O) Particle (O)	Flow (X) - using known flow field Particle (O)		Volume of Source proximate zone=>decided by comparison with measurement	Flow rate Around source (uniform Gaussian distribution)			Exposure estimation (Two zone)
Rodes et al. (1995)	Flow (O) Particle (O) Wind tunnel experiment			Wind tunnel cross section (1.83x1.83)				Personal aerosol sampler
Todd & coworkers (1994, 96, 97)	CT							Two-zone
LBL (1994, 96, 98)	CT							
Murakami et al. (1991)		Flow(O) *k*-_ Particle (X)	Ar=0.0-0.032	2.5X2.3X215	Re=2500	Side wall 1 square slot	Side wall 4 square slots	anisotropic *k*-_ model
Yaghoubi et al. (1995)		Flow (O) *k*-_ Particle (O)	Ar=0.000151-0.00172	3.0x9.0x3.0	4.16, 6.25 ach	Side wall slot	Side wall slot	

Authors	Experiment	Calculation	Temperature (˜T= T_{jet}- T_{room})	Room Size (LxWxH) (LxH) [m]	Supply Flow Rate	Room Air Supply	Room Air Exhaust	
Murakami et al. (1994)	Flow (O) Particle(X)	Flow(O) Particle(X)	Ar=0.016	2.5X2.3X2.5	Re=2700	Side wall 1 square slot	Side wall 4 square slots	*k*-_ EVM ASM DSM

II. A LARGE INDOOR FACILITY FOR TRACER GAS EXPERIMENTS

Introduction

Measurements of gas dispersion are useful for quantitative analysis of air flows, fluxes of trace gases and pollutants, and for testing predictions from computational fluid dynamics (CFD). In particular, it is of interest to measure the spatial and temporal features of gas dispersion in indoor environments where contaminant concentration distributions, and hence human exposure, can change rapidly with time and in space (Rasouli and Williams 1995; Beychok 1997; Rasouli and Williams 1997).

Previous work on measuring the dispersion of indoor air has been conducted using both conventional pump-tube sampling (e.g. Baughman et al. 1994; Drescher et al. 1995), and the combination of open-path (OP) remote sensing (typically with Fourier transform infrared spectroscopy) and computed tomography (CT) (Yost et al. 1994; Drescher et al. 1997; Todd and Bhattacharyya 1997; Piper et al. 1999; Price 1999). In applications requiring rapid non-intrusive measurements with good spatial coverage and resolution, new technologies have allowed us to make substantial improvements in speed over past efforts.

In this section we describe a measurement system and experimental chamber that provide the capability to measure the temporal evolution of tracer gas concentration during a transient release. The measurement system combines rapid OP measurements using a tunable-diode-laser (TDL) spectrometer. These data are then used to reconstruct a map of gas concentration using computed tomography algorithms described in the next section.

Materials and Methods

- Tracer Gas Measurement System

Path integrated gas concentrations are determined by measuring the attenuation of infrared radiation in the region of a peak in the absorption spectrum of the tracer gas of interest (here, methane). To continuously correct for absorption by other gas species (e.g. water vapor), the system compares the attenuation spectrum measured in an open path with that observed in a reference cell containing only the tracer gas. The gas measurement system, called LasIR, was manufactured for us by Unisearch Inc., London Ontario, Canada. Here we provide a brief description of the system components.

- Tunable diode laser spectrometer (LasIR)

The spectrometer employs a single mode distributed feedback (DFB) tunable diode laser operating at 1.635 microns. The laser frequency is controlled by the diode temperature which is a function of bias current and thermal cooling, both of which are actively controlled. After a two-stage optical isolator and fiber-optic coupler, the output power of the laser is ~ 10 mW.
The optical layout internal to the LasIR, shown in Figure 1, divides the beam into three parts with a beam splitter. First, 10% of the light is used to supply an internal CH_4 reference channel

that contains a sealed cell of ~ 0.1 % CH_4. The remaining light is passed through a calibration cell and then divided into two measurement beams that are available at the back of the instrument at fiber optic output ports. Hence, the calibration cell is always included in any path being measured. The absorption spectrum is detected in the reference channel and both measurement channels using two-tone frequency modulation as follows.

The fundamentals of detection with two-tone frequency modulation (TTFM) are reviewed in (Brassington 1995). Briefly, in the present system, a modulation signal is produced by mixing a high frequency carrier (~ 500 MHz) and a second fixed oscillator at 5 MHz to produce tones at 495 and 505 MHz . The two-tone signal is added to the laser bias current to produce two sets of side-bands (495 and 505 MHz) above and below the frequency of the laser line. The laser radiation is then emitted from launching optics, traverses the open path, and is absorbed on a photodiode detector. The relative intensities of the sidebands reaching the detector depend upon how much each set of sidebands is absorbed by the CH_4 line. The presence of CH_4 in the open-path results in a 5 MHz signal that can be detected using the relatively inexpensive room temperature gallium phosphide (GAP) detectors. The 5 MHz signal is carried over co-axial cable from the detector to the LasIR and demodulated. The system also sweeps the two-tone signals across the CH_4 line (the total frequency sweep is ~ 0.4 cm^{-1}) at ~ 1 kHz in a saw-tooth pattern. The result is a signal that approximates a second derivative of CH_4 absorption as a function of laser center frequency. For each sweep of the laser, the amount of CH_4 in the measurement channels signal is determined by performing a linear fit of each measured signal spectrum to the reference channel spectrum. The slope of the fit, normalized by the total power in the measurement channel, is a measure of the amount of CH_4 present. For each measurement channel, a mean slope is computed every four sweeps, is normalized by the mean signal power, and is transmitted from the LasIR to the host computer every 11 ms using two 16 bit parallel digital interfaces. The resulting detection limit for CH_4 is approximately 2 ppm-m in a one second integration, yielding a maximum dynamic range of about 10,000.

- Fiber optic/RF multiplexers

A schematic diagram of the fiber and open path optics is also shown in Figure 1. Each of the 2 optical channels available from the LasIR is multiplexed onto one of 30 fiber optic lines that lead to the open-path source lenses. All of the fiber-optic cables have angled connections to reduce interference fringes which arise from multiple internal reflections within the optical paths from the laser to the detectors.

- Open-path optics

The open-path sensors used in this system come in two types. First, the thirty long optical paths (from 2-30 m in length) each comprise a pair of source and receiving optics and are henceforth termed remote sensors. The source optics is a single 0.6 cm diameter glass lens that has been anti-reflection coated for 1.6 micron radiation. The remote receiving optics is a 2.5 cm diameter collection lens that has no anti-reflection coating and a 0.3 cm diameter glass lens that is part of the GAP-1000L detector package (Germanium Devices Inc.). Both the source and receiving optics are mounted in stages that allow limited adjustment of the direction of the optic axis. Second, thirty short optical paths (each 0.1-1 m in length) each comprising a single folded path using a source optics, a return mirror, and a GAP-1000L detector. All of these components are

mounted in stages, and are affixed to a single steel tube. This arrangement is henceforth termed a point sensor. In the standard configuration the point sensors have a physical length of 0.5 m and an optical path length of 1m. Coarse positioning of the remote sensor optics is achieved with a pair of right angle tubes with clamps(source optic) or ball and socket (receiver optic) mounts.

- Host computer software

The host computer controls the two optical multiplexers to select which long and short path channel will be measured. The integration time on each channel is specified in a sequence file that is loaded at the beginning of each experiment. The minimum integration time on a given path is 200 ms. During an experiment, the raw (uncalibrated) data measured by each of the two channels of the LasIR are transmitted to the host computer as a 16 bit digital words every 11msec. This high-speed data can be recorded onto the hard disk. The host computer then integrates the raw data over the specified integration period, applies the calibration factors stored in the calibration file, and writes the measured average CH_4 concentration, the standard deviation of those data, and the number of data points in the average, to the hard disk.

- Calibration gas supply system

Calibration of the LasIR instrument is performed by measuring signal levels on all the optical channels after filling the 12 cm long calibration gas cell internal to the LasIR with a known standard. Currently, a system of solenoids and a pump allow one to fill the calibration cell with either ambient laboratory air, 1% CH_4 in N_2, straight N_2. Before a set of experiments an initial two point calibration (using ambient air and the 1% CH_4) is performed to calculate approximate values for the offset and gain of the system. In addition to the initial calibration, the two point calibration is repeated at the beginning of each experiment to check for offset drifts. Following each calibration the cell is flushed with ambient air from the laboratory or N_2.

- Experimental Test Chamber

The chamber is located in Building 71-106 on the LBNL site. It has approximate dimensions 7m x 9m x 11 m in height (~ 690 m^3 volume), is lined with galvanized steel sheets, with the sheet seams sealed with aluminum tape. A schematic drawing of the chamber, with five air supply registers and the air exhaust register, is shown in Figure 2. The supply registers are 1.3 m wide and 0.3 m high. The floor, the lower 2.3 m of the chamber walls, and the entire East wall of the chamber are constructed of concrete. The remaining upper sections of the chamber walls and ceiling are hollow. The exhaust register is a square approximately 50 cm on a side that is recessed into the ceiling in a 1.8 m x 1.2 m x 1.2 m tall air shaft (not shown in Figure 2). In addition to the HVAC system, a blower mounted in the South wall of the chamber at a height of approximately 4 m can be used to rapidly flush the chamber.

- Optics geometry in chamber

The optics are mounted so that all optical paths are horizontal and within 10 cm of a horizontal plane 2 m above the chamber floor to allow measurement of gas concentrations. The remote optical sensors are mounted (using magnetic clamps) to 0.5 cm thick steel bars fixed to the

chamber chamber walls, while the point sensors are suspended from cables just above the plane defined by the remote sensors. A plan view of the layout of the optical paths is shown in Figure 4. In addition to the sensors shown in Figure 4, an additional point sensor is used to monitor the concentration of CH_4 in the ventilation air supplied to the room (at the lowest supply register).

HVAC and Tracer Gas System

A schematic showing the layout of the flow and temperature control systems is shown in Figure 3. The system can supply air to the room at temperatures ranging from approximately 10 to 30 C, from approximately 1.5 to 6 air changes per hour (ACH). The flow rate of supplied air is measured with a flow measurement station comprising 15 and 30 cm diameter venturis in parallel, each instrumented with a digital manometer. A second set of venturis, located in the outside air supply stream, were installed but have not been instrumented with manometers.

- Temperature logging system

The temperatures of the chamber walls, roof and floor are measured at 2 positions on each surface using AD-590 temperature dependent current sources. The output of the sensors are logged on a Keitheley data acquisition system at an adjustable rate. The temperature sensors were cross calibrated against thermocouple sensors in a temperature controlled calibration chamber to achieve an absolute accuracy of ~ 0.5 C, and a relative accuracy of < 0.3 C, over the range from 15 to 30 C.

- Tracer Gas Release System

Tracer gas is released into the room from a 1m x 1m area source at a controlled rate. Approximately uniform release over the source area is achieved by forming a spiral release tube out of 0.8 mm ID Tygon tubing. The radial distance between consecutive turns of the spiral is approximately 20 cm. The release tube has 1.2 mm diameter holes drilled at 10 cm intervals. Both ends of the release tube are connected to the supply line to minimize pressure drops along its length (Figure 5).

We use 4% CH_4 in N_2as the tracer gas. This is the highest concentration of CH_4 that is explosion-safe. The release rate is controlled with a mass flow controller (Sierra Inst. Inc.). During experiments, the concentration of the tracer gas supplied to the room can be monitored continuously by routing the tracer gas through a 30 liter PVC cell containing a point sensor. For a typical tracer gas release rate of 20-40 lpm, the residence time of gas in the cell is ~ 1 min.

RESULTS

System Tests

- Tests of HVAC system flow rate

Two methods were used to estimate the flow rate of air supplied to the room. First, the flow speed of air supplied to the room from the supply registers was measured with a hot wire

anemometer positioned on a rectangular grid of 36 positions (1.3 m x 0.3 m in extent) at 10 cm in front of each supply register. The flow rate measured by the flow measurement station 0.87 +/- 0.02 m^3/s (1830 +/- 50 cfm). The volumetric flow rates inferred by multiplying the average of the 36 measurements for each supply register by the area of the register ranged from 0.13 +/- 0.013 to 0.16 +/- 0.016 m^3/s, with no obvious variation with the height of the register on the wall. The summed flow rate of 0.71 +/- 0.07 m^3/s (1500 +/- 150 cfm) is 0.82 times that reported by the flow measurement station. Further, this estimate is likely to be a slight underestimate of total flow because there is likely to have been additional flow from the vent at positions beyond those measured; flow from a 3 cm wide strip at the edge of the measured region would make up for the factor of 0.82 difference in total flow rate.

The second method used to check the air flow was to measure the first order decay rate in tracer gas concentration under well mixed conditions with no air re-circulation. The flow rate is then the product of the chamber volume and the decay rate. The test was conducted by filling the chamber to an easily measurable concentration, mixing the air vigorously with an internal mixing fan, and measuring the decrease in gas concentration with time. During the test, the ventilation system was run at a constant rate of 0.43 m^3/s (900 cfm) as measured by the flow station. Both the point and remote sensor channels showed similar first order decays in concentration with time. The mean decay rate for all channels was 2.6 +/- 0.1 air changes per hour which is equivalent to a flow rate of 0.50 +/- 0.02 m^3/s (1050 cfm) or 1.16 times that measured by the flow station.

- Combined test of System Response to Tracer Gas Release

As a combined test of the instrument calibration, tracer gas release system, and the volume and air-tightness of the experimental chamber, 0.8 m^3 of 4% CH_4 was released into the chamber and well mixed by a large fan internal to the chamber (during this test the HVAC system was not run). The calibration of the sensors was obtained using the calibration system. The path integrated concentration was measured for each remote and short path sensor as a function of time during the release. As shown in Figure , the resulting mean response measured by the remote (point) sensors was within 10% (25%) of that expected for based on the instrument calibration, the estimated volume of CH_4 released, and the estimated chamber volume (40,000 ppm x 0.8 m^3 /694 m^3 = 46 ppm). Further, and of importance for uncertainty in computed tomographic reconstructions, the range in concentrations for the remote (and point) channels was within 10% of the mean response.

- Testing the ATRIUM Operation

To test the overall experimental system, a tracer gas release experiment chamber was conducted in the chamber under conditions of high ventilation rate of 1.2 m^3/s (6.4 ACH), with no re-circulation of chamber air. The methane release rate was 0.6 lpm. The experiment consisted of a calibration w/ 1% CH_4 (added to the calibration cell), a settling period that was used to measure the offset on each channel and then a release of 4% CH_4 from the release source into the chamber lasting from 400-2600 s. The chamber was then flushed with outdoor air using the ventilation fan and then the experiment was repeated. A total of three runs were recorded. The CH_4 path integrated concentrations measured on the remote sensors from one of the three experiments are

shown in Figure 7. The differences in integrated concentration observed by the different channels are due to the combination of the different path lengths and the differing positions in the chamber.

The data collected from each complete set of measurements can be used to reconstruct a map of gas concentration in the measurement plane using the computed tomography algorithms described later in this document. Here, gas concentrations measured along each remote path are shown in Figure 8 for a set of four 21-second intervals taken from early to late in the experiment. Using the path integrated data from Figure 8, best fit reconstruction maps are shown in Figure 9. Also shown in Figure 9 are the measured concentrations for each of the point sensors, as well scatter diagrams showing the correlation between the measured point sensor data and a predicted concentration for that point sensor. The predicted concentration for each short path sensor is obtained by integrating the reconstructed concentration map over the path of each point sensor. Generally good agreement is found between measured point sensor data and the concentration of the reconstructed map with correlation (R) values in the range from 0.71-0.93. This demonstrates that very rapid acquisition of highly spatially resolved maps of tracer gas concentration is possible with this technique.

While this technique represents a great improvement over previous techniques for measuring tracer gas dispersion, the correlation between reconstructed maps and point sensor data is not perfect. The observed differences are due to a combination of two factors. First, the gas concentrations may have spatial structure small enough to be detected by a given remote (or point) sensor but not be detected in nearby sensors. The solution to this problem is to increase the volume of space covered by the infrared beams. This can be achieved increasing the number of beam paths. Second, temporal variations in the gas concentration can occur on time scales comparable to or shorter than the time (currently 6 seconds) required to complete a scan of all 30 remote (or point) channels. If the concentration varies during a scan then the reconstructed image will be contain errors due to those variations. The solution to this problem is to reduce the time to complete a scan of all channels. Ideally all channels would be observed simultaneously so that a complete set of measurements could be obtained in the time that it now takes to obtain a measurement of one channel. The limitations of both spatial and temporal resolution have been explored using spatially and temporally resolved images obtained from the water tank experiments. This analysis is described in the section on computed tomography.

REFERENCES

Baughman, A. V., A. J. Gadgil and W. W. Nazaroff (1994). Mixing of a Point Source Pollutant By Natural Convection Flow Within a Room. Indoor Air-International Journal of Indoor Air Quality and Climate **4**(2): 114-122.

Beychok, M. R. (1997). Application of dispersion modeling to indoor gas release scenarios. Journal of the Air & Waste Management Association **47**(7): 738-738.

Brassington, D. J. (1995). Tunable Diode Laser Absorption Spectroscopy for the Measurement of Atmospheric Species. Spectroscopy in Environmental Science. R. J. H. Clark, and R.E. Hester, John Wiley & Sons**:** 85-148.

Drescher, A. C., C. Lobascio, A. J. Gadgil and W. W. Nazaroff (1995). Mixing of a Point-Source Indoor Pollutant By Forced Convection. Indoor Air-International Journal of Indoor Air Quality and Climate **5**(4): 204-214.

Drescher, A. C., D. Y. Park, M. G. Yost, A. J. Gadgil, S. P. Levine and W. W. Nazaroff (1997). Stationary and time-dependent indoor tracer-gas concentration profiles measured by OP-FTIR remote sensing and SBFM-computed tomography. Atmospheric Environment **31**(5): 727-740.

Piper, A. R., L. A. Todd and K. Mottus (1999). A field study using open-path FTIR spectroscopy to measure and map air emissions from volume sources. Field Analytical Chemistry and Technology **3**(2): 69-79.

Price, P. N. (1999). Pollutant tomography using integrated concentration data from non-intersecting optical paths. Atmospheric Environment **33**(2): 275-280.

Rasouli, F. and T. A. Williams (1995). Application of Dispersion Modeling to Indoor Gas Release Scenarios. Journal of the Air & Waste Management Association **45**(3): 191-195.

Rasouli, F. and T. A. Williams (1997). Application of dispersion modeling to indoor gas release scenarios - Response. Journal of the Air & Waste Management Association **47**(7): 738-738.

Todd, L. A. and R. Bhattacharyya (1997). Tomographic reconstruction of air pollutants: evaluation of measurement geometries. Applied Optics **36**(30): 7678-7688.

Yost, M. G., A. J. Gadgil, A. C. Drescher, Y. Zhou, M. A. Simonds, S. P. Levine, W. W. Nazaroff and P. A. Saisan (1994). Imaging Indoor Tracer-Gas Concentrations With Computed Tomography - Experimental Results With a Remote Sensing Ftir System. American Industrial Hygiene Association Journal **55**(5): 395-402.

FIGURES

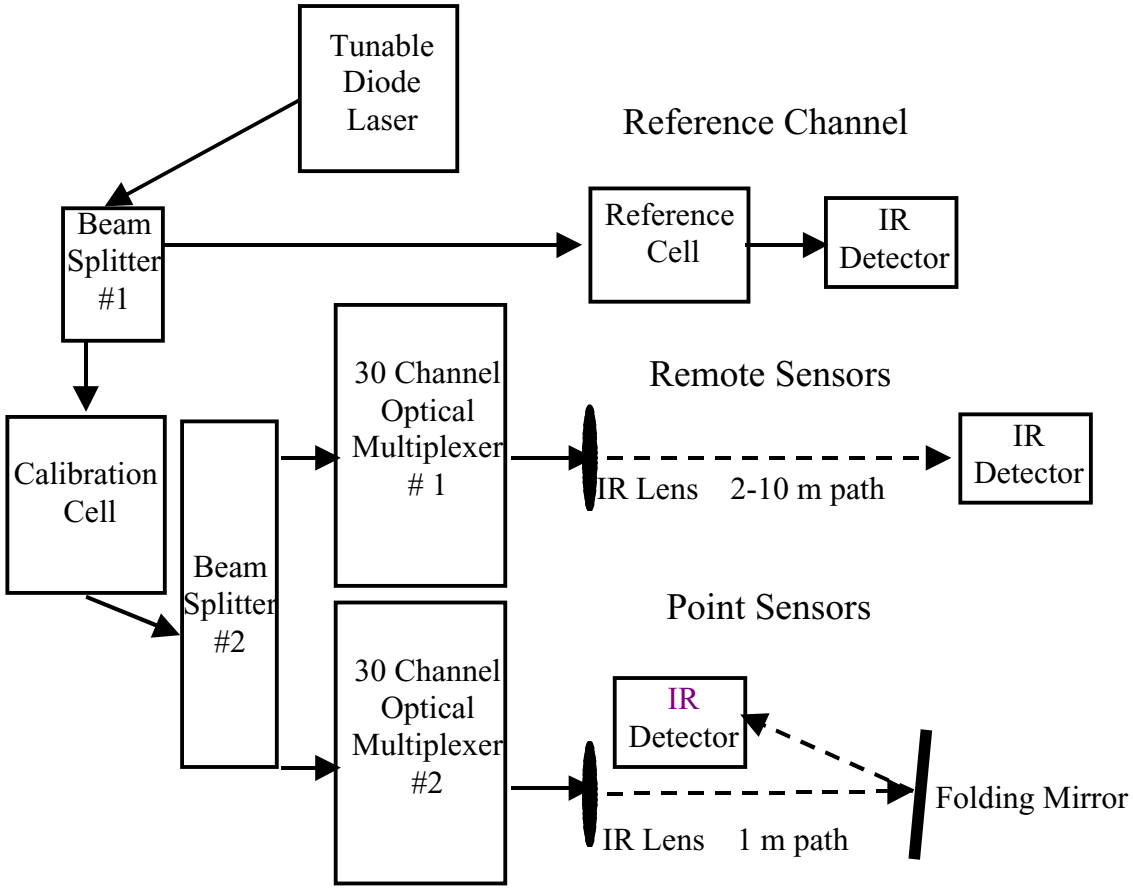

Figure 1. Optical layout of LasIR spectrometer and open-path optics. Solid lines indicate sections where beam is carried in optical fiber. Dashed lines indicate open-paths. Optics for one remote and point channel (of 30) each are shown connected to optical mulitiplexers 1 and 2 respectively. Because the calibration cell is always in the optical path of any measurement, after calibration, it is filled with ambient air.

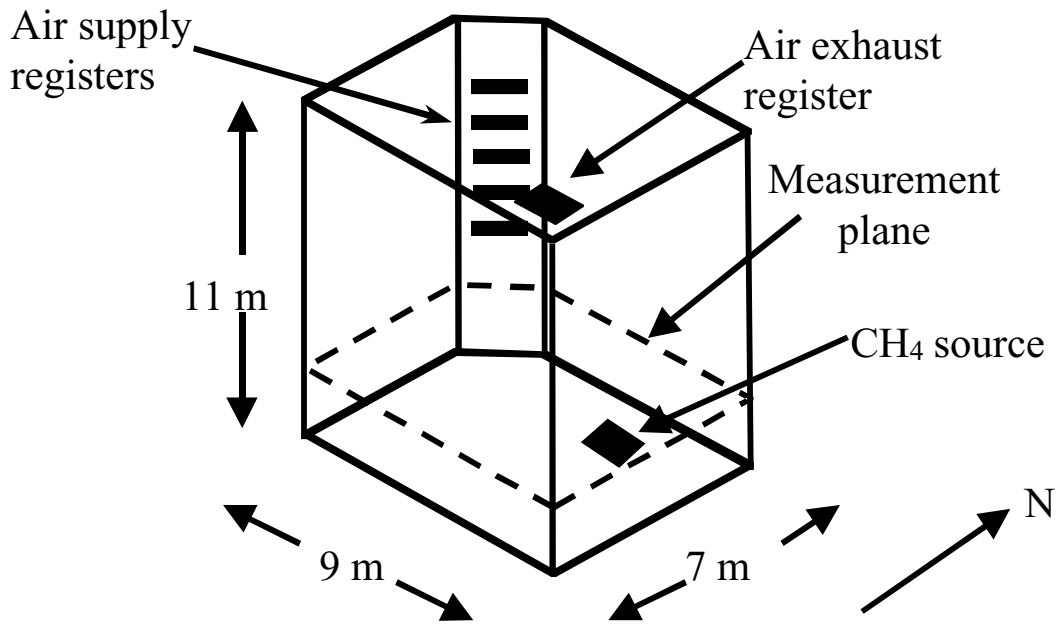

Figure 2. Side view of experimental chamber showing air supply and return registers, tracer gas release source, and open-path gas measurement plane.

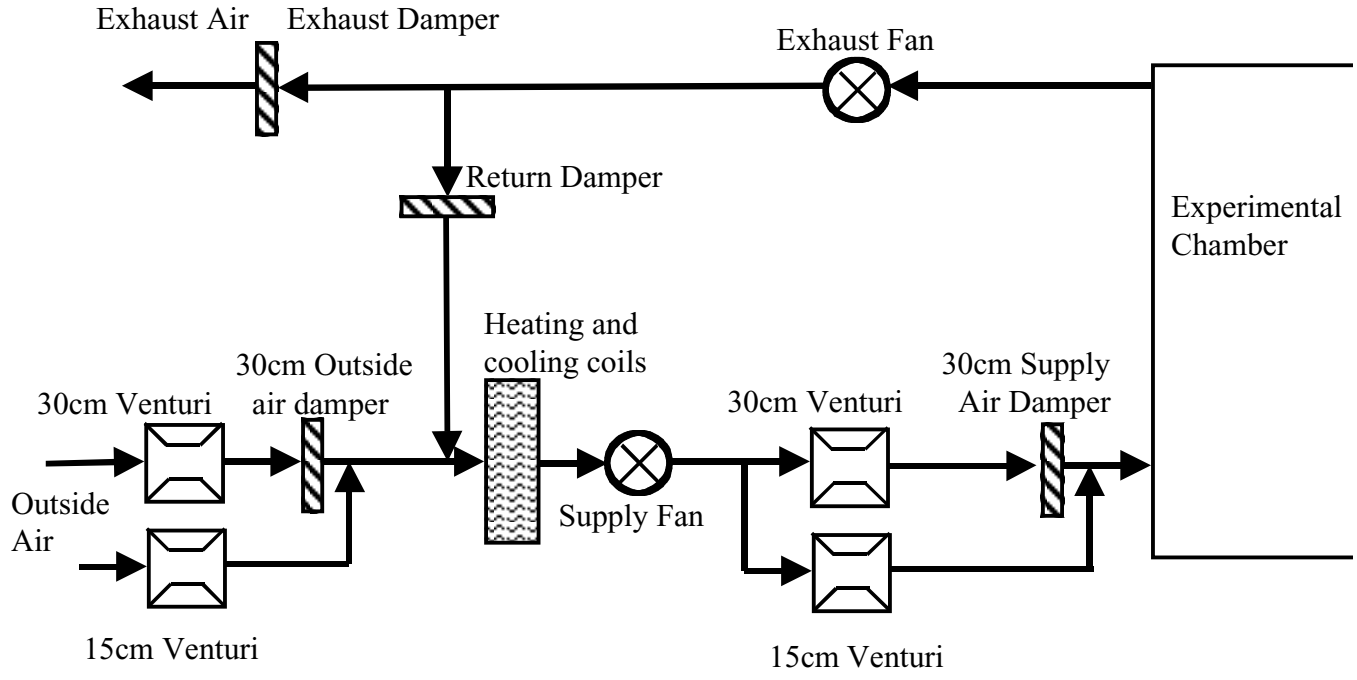

Figure 3. HVAC flow measurement and control system. Note that a minimum of 10 % the air supplied to the experimental chamber comes from outside.

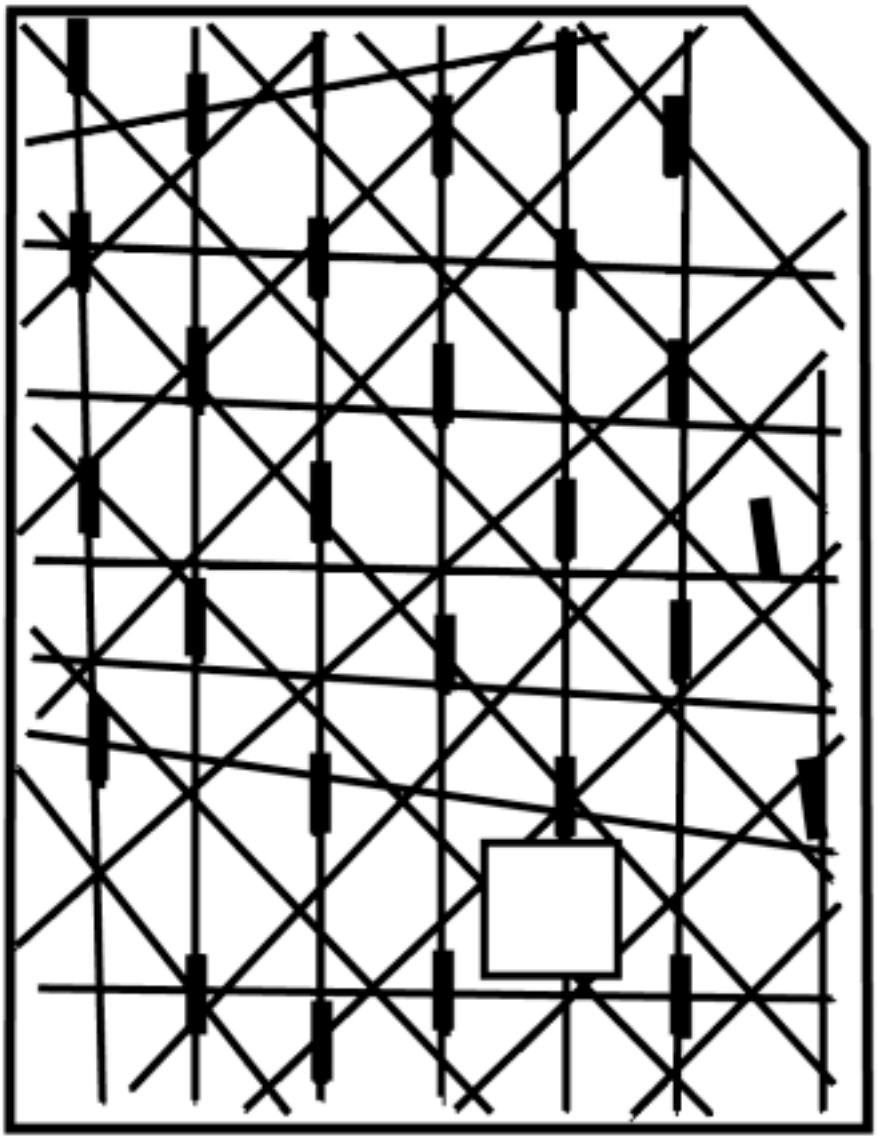

Figure 4 Top view of optical path geometry in experimental chamber. All beam paths are arranged in a horizontal plane at a height of 2m from the chamber floor. Thick lines indicate ray paths of point sensors, while thin lines indicate ray paths of remote sensors. The square box indicates the location of the tracer gas release source.

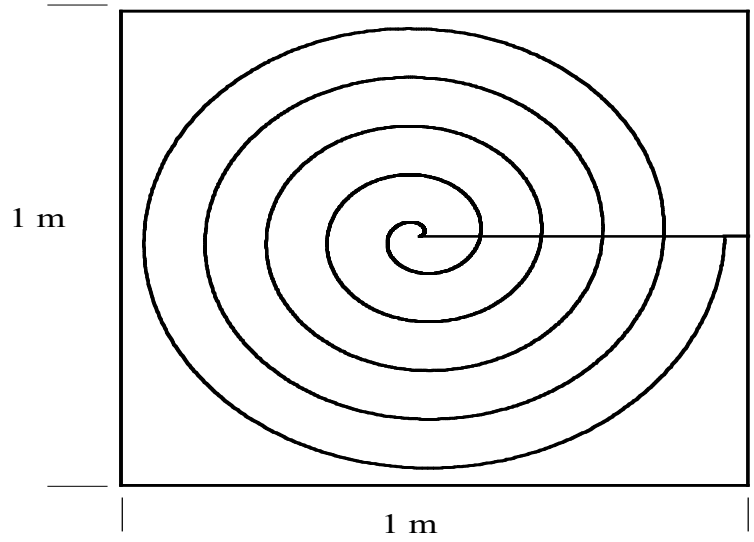

Figure 5. Geometry of gas release source. The 1 cm diameter spiral release tube has 1.2 mm diameter holes drilled at 10 cm intervals. The tube is mounted in a 5cm deep box with the holes facing away from a perforated top plate. Both ends of the tube are connected to the inlet to reduce pressure drops along the tube.

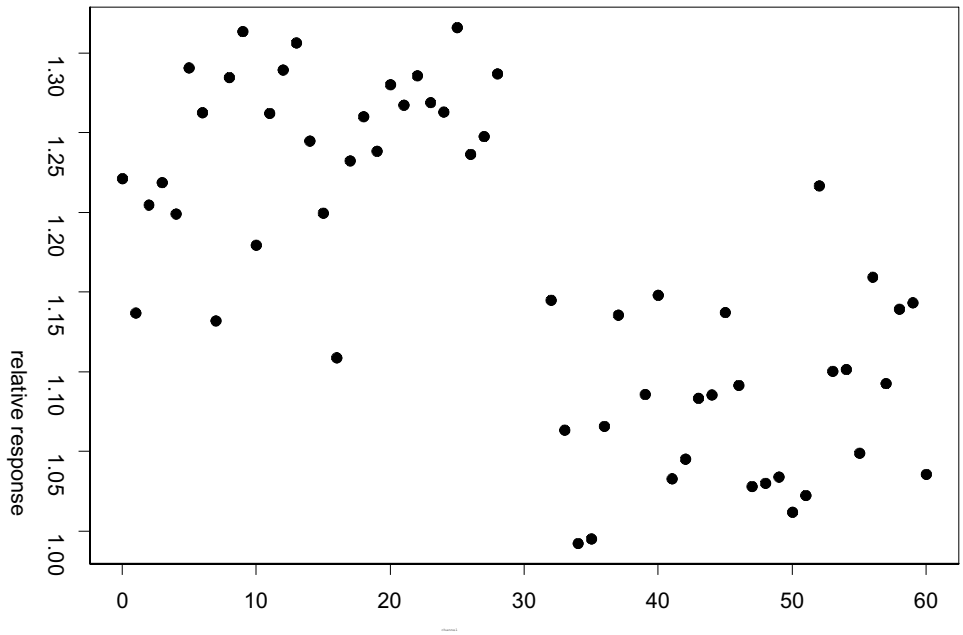

Figure 6. Response of open-path channels to a release of methane into the experimental chamber relative to that expected based on release rate measured by mass flow controller and chamber volume. The mean response of remote (channel 32-60) and point (channel 0-29) channels are 8% and 24% greater respectively than expected based on instrument calibration, the reported concentration of tracer gas, release volume, and estimated room volume. As a matter of importance for the spatial distribution obtained in reconstructions, the range of values about individual means are 10% for both the point and remote sensors.

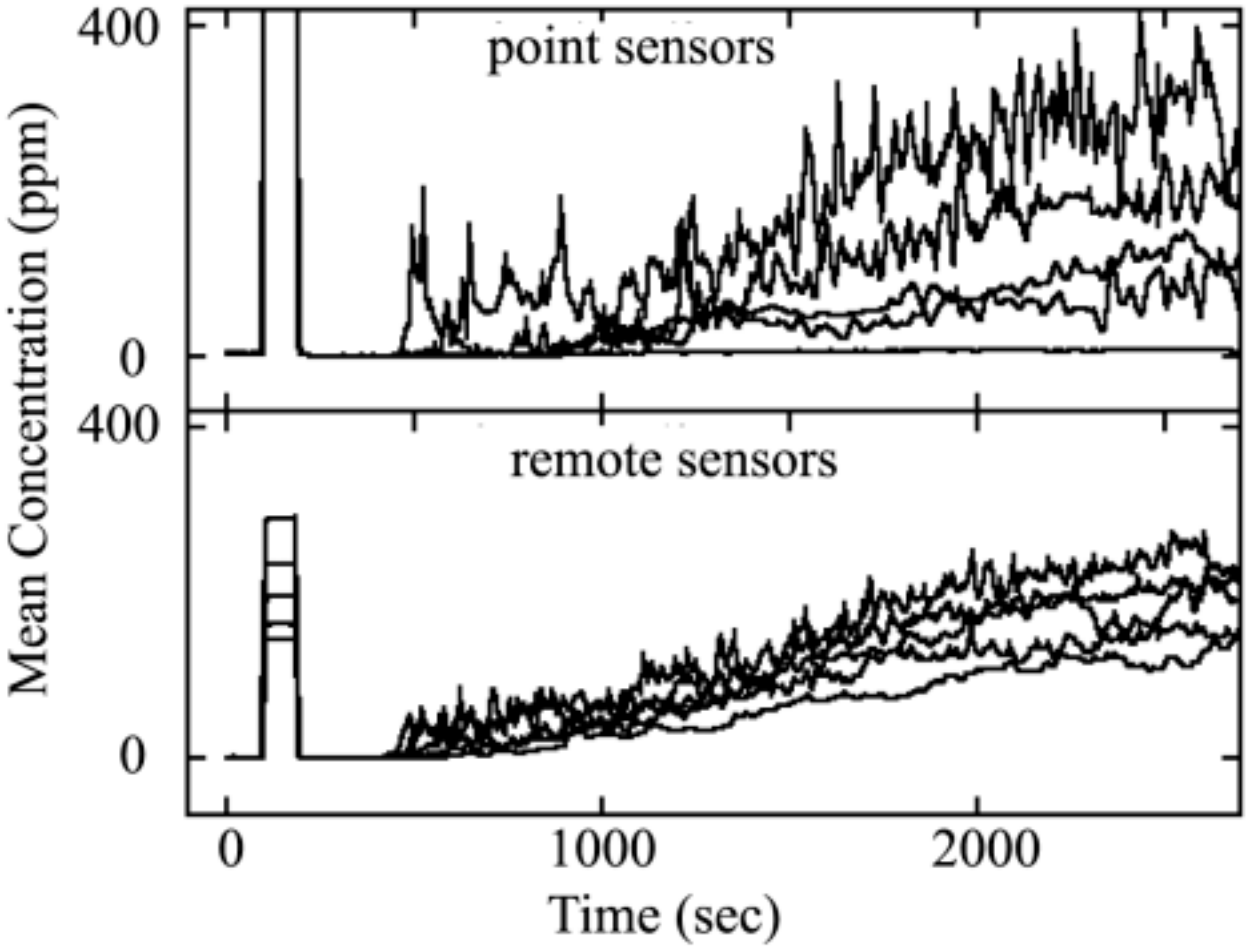

Figure 7. Path integrated methane concentrations measured on selected point and remote sensors during a CH_4 release experiment. The experiment was conducted at a ventilation rate of 1.2 m^3/s (6.4 ACH), with no re-circulation of chamber air. The methane release rate was 0.6 lpm from 400 to 2600 seconds. The differences in integrated concentration observed by the different channels are due their different positions in the chamber.

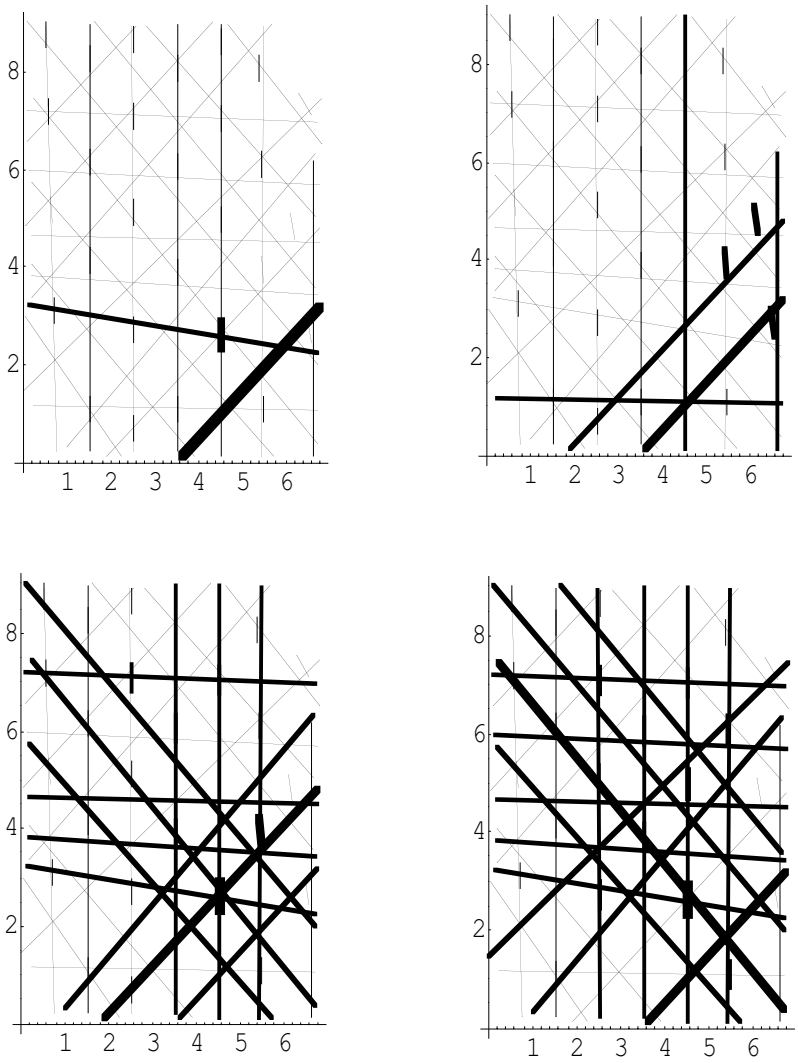

Figure 8. Average path-integrated concentrations for four 21-second long time intervals during experiment shown in Figure 7. The line thickness indicates the average concentration along each path. The dimensions of the room are indicated units of meters.

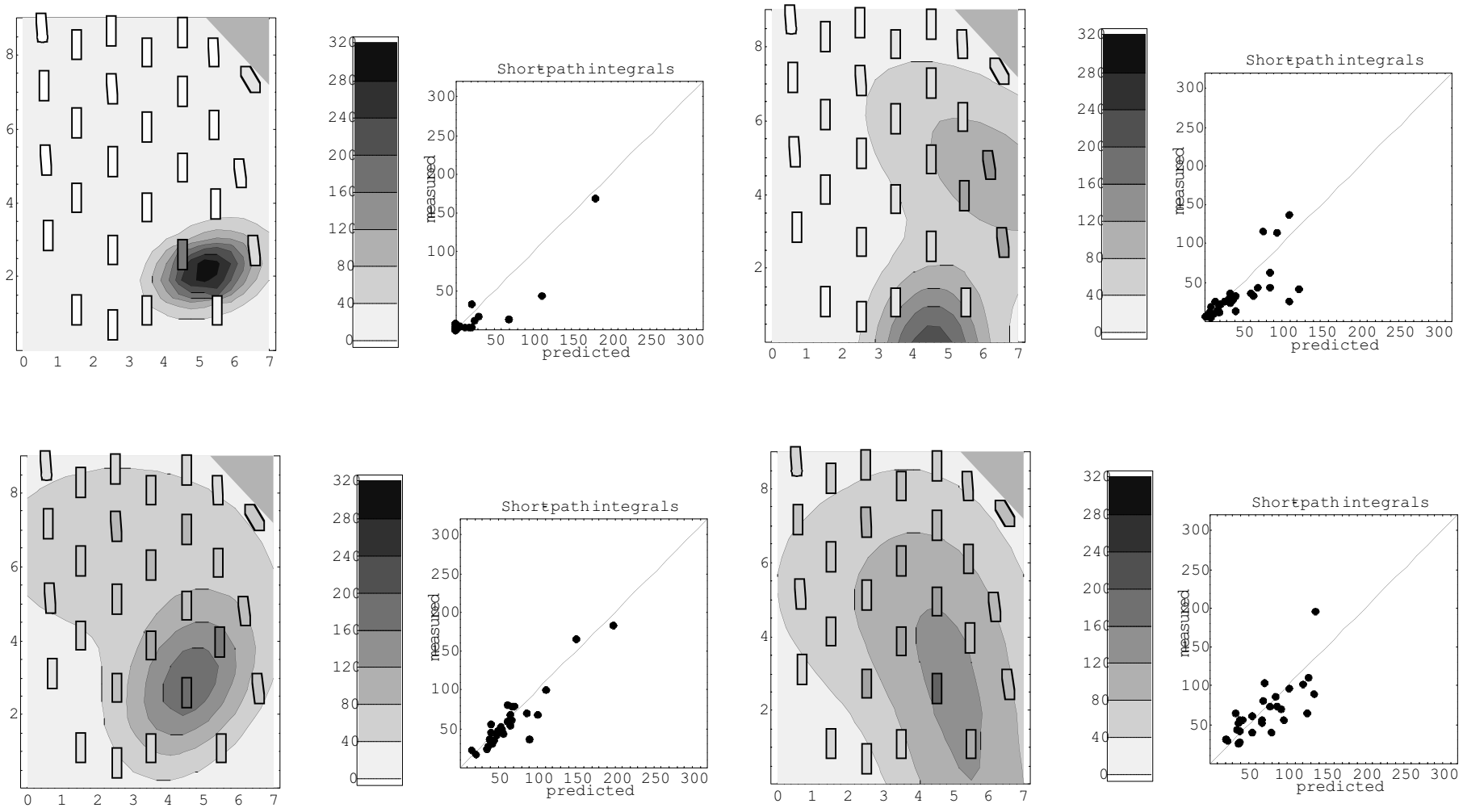

Figure 9. Gas concentration maps reconstructed from the remote sensor data shown in the four frames of Figure 8, and point sensor measurements of gas concentration. For each map, a scatter plot is included that shows the comparison between the measured and the predicted concentration for each point sensor. The predicted concentration for each short path sensor is obtained by integrating the reconstructed map over the path of each point sensor.

III. COMPUTED TOMOGRAPHY

Introduction

Computed tomography (CT) is the process of estimating the value of a parameter as a function of position, given only path-integrals of the parameter along a set of pre-determined paths. In our case, we produce a map---an estimate of the methane concentration at each point in a plane---given the integrated concentration along 30 optical paths. We refer to an estimated methane map as a reconstructed map.

Computed Tomography has mathematical roots in the Radon tranform (Radon, 1917), and has found common application in medical imaging, specifically in Computer Aided Tomography and Positron Emission Tomography (Natterer, 1986). These medical techniques make integrated measurements along thousands or even tens of thousands of paths, in contrast to the few dozen paths to which we are limited by experimental constraints. Unfortunately the computational methods that work very well for medical imaging do not work very well for our problem (see Drescher et al., 1995, and Todd and Ramachandran, 1994).

In this chapter, we briefly discuss the major issues associated with the CT reconstruction. These include deciding on an arrangement of optical paths (the ray geometry), choosing an algorithm for performing the reconstruction, and algorithm implementation details. It was necessary to work on many of these items in parallel. For instance, in order to choose a ray geometry, we needed to perform reconstructions with a particular algorithm using simulated data and evaluate both the resulting computational efficiency and the accuracy of the results. Thus the ray geometry question was intertwined with the CT algorithm and its numerical implementation, as well as the issue of quantifying the agreement between the reconstruction and the original synthetic data.

Choosing an arrangement of optical paths

Previous work by us (Drescher et al., 1996 and Drescher et al., 1997) and others (Yost et al., 1999, and Todd and Leith 1990) has addressed optical paths that radiate out from a unified source/detector combination and either bounce back directly at retro-reflectors or first bounce off a mirror to a retro-reflector and then bounce back to retrace their path. In contrast, the experimental equipment used for the present work allows more flexibility---rays can begin and end anywhere on the perimeter of the room (or, indeed, in the interior of the room if free-standing mounting devices are used).

An early decision was to consider only ray geometries that cover a plane with approximately uniform density. An alternative approach would have been to place more optical paths in regions of expected high methane concentration, or perhaps expected high concentration gradient. This latter approach was rejected because we wished to remain as flexible as possible about experimental conditions, and because it is impossible to know in advance what areas might have high concentrations or high gradients. In principle the CFD or water model data could help address the issue, but in practice the experimental conditions in the current water model and CFD runs may differ from those in the full-scale experimental chamber.

In standard terminology of medical imaging, a set of parallel rays is called a *view*. A natural way of creating a geometry is to divide the thirty available optical paths into a small number of views. For instance, we could use two orthogonal views to create a rectangular grid of optical paths. In our terminology, such a pattern would be a *two-way grid*.

Each optical path measures the path-integrated concentration only along a very narrow beam, so narrow that it can be thought of as a mathematical line. As a result, no matter what geometry is used there will be many unsampled areas. We investigated the effectiveness of 3-way, 4-way, and 5-way grids, first by using simple simulated gas distributions---a superposition of Gaussian plumes---and later by using data from the water model.

We know of no theoretical way of evaluating the effectiveness of different geometries, though there are methods of examining the spatial and angular densities as a function of location. It is obvious that long, wide unsampled areas are undesirable, since they effectively limit the resolution that can be reached even in principle---we cannot reasonably hope to reconstruct the spatial variation of gas concentration in an area through which no ray passes, since we will have no information at all about the concentrations in that area. Spatial density of the rays is not the only factor, however: just because a geometry has dense spatial coverage does not ensure that it will produce accurate reconstruction.

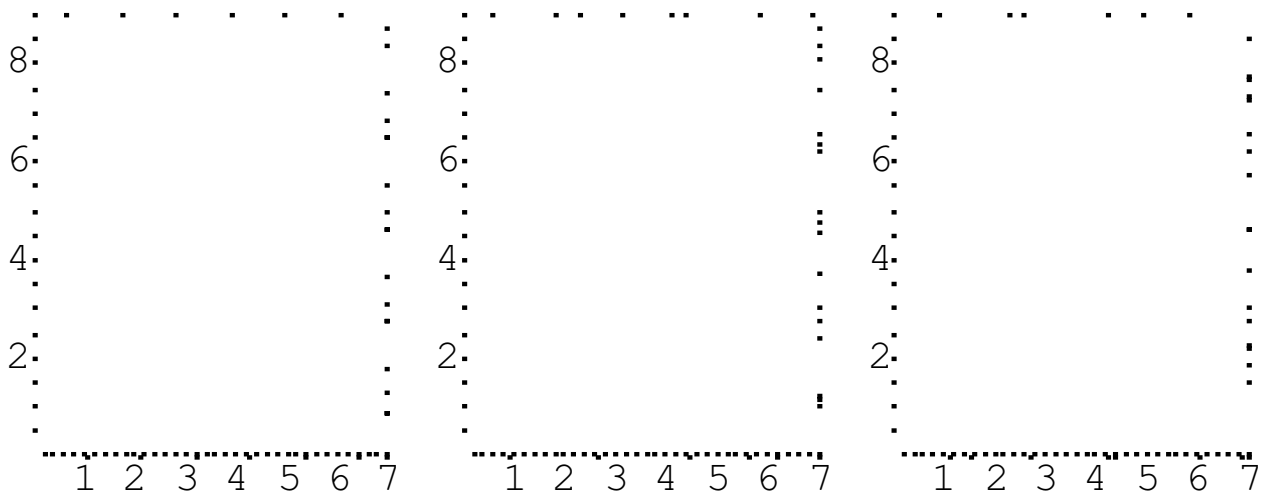

Figure 1. 3-way, 4-way, and 5-way grids, each with thirty rays. The three-way grid has the smallest unsampled spaces; the five-way performs best when concentrations do not have spatially sharp peaks. The 4-way is a compromise between these two.

The *water model* experiments use water in a scale model of the large experimental chamber in order to simulate airflow. Dye is used in place of the methane tracer gas used in the large chamber. The water model experiments yield dye concentrations in a plane (corresponding to the breathing plane in the experimental chamber) at a high spatial resolution, in a video whose time-scale is such that each frame represents about 3 seconds in the large chamber. To use the

water model data to investigate computed tomography methods, we calculate the path-integrated concentrations that would be measured if the concentrations of the dye in the water model represent methane concentrations in the large experimental chamber. We use these calculated path integrals as inputs into our tomography algorithm, and compare the resulting reconstruction with the original data.

Figure 2 illustrates that point. Figure 2a shows an image based on data from the water model. The figure shows the time-average dye concentration at each point in a plane. From these data, we calculated ray integrals for a four-way grid. Using the methods discussed later in this chapter, we then performed a reconstruction using these ray integrals; results are shown in Figure 2b. The reconstruction matches the ray integrals essentially perfectly (the coefficient of determination is r^2 = 0.96), but does not perfectly reproduce the actual map, though most of the major features are correctly captured. As far as the SBFM algorithm is concerned, figure 2b is a nearly perfect solution, in the sense that it correctly predicts all of the ray integrals.

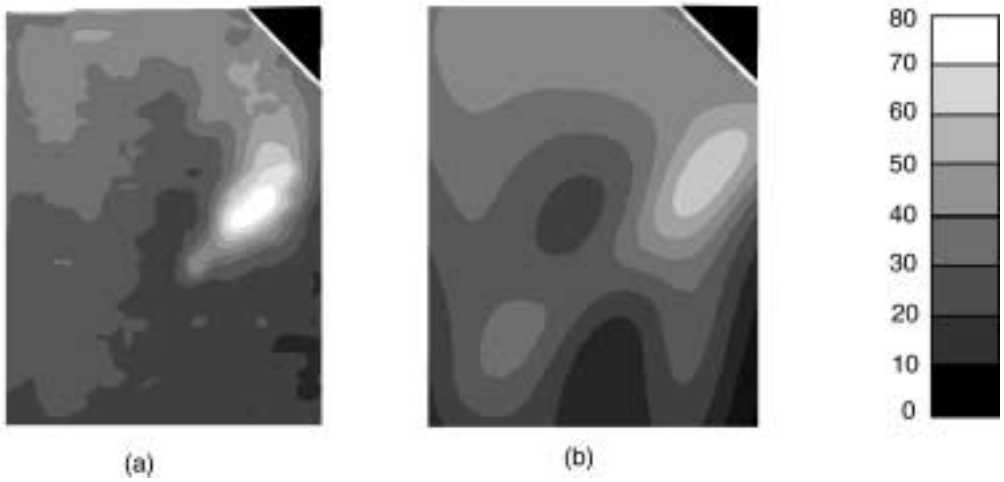

Figure 2. (a) Time-averaged dye concentrations in a plane, measured in the water model. [Note: need to make a B&W version of this figure with no short-paths superimposed]. (b) Reconstruction based on ray integrals in a four-way geometry, calculated from (a). Most of the gross features are accurately reproduced, but the reconstruction shown in (b) is not perfect, in spite of the fact that the ray integrals are nearly perfectly matched.

Comparing the reconstructions (not shown here) made using synthetic data from 3-, 4- and 5-way grids, all three geometries performed similarly. Although we are hampered by lack of an unambiguous way of measuring reconstruction fidelity, it seems that in general, the more different views in a geometry, the better the reconstructions, provided the smallest areas of high concentration were larger than the unsampled areas. Thus, for wide distributions of gas, the 5-way worked somewhat better than the 3-way, in the sense that the reconstructions tended to match the true concentration distributions more closely. However, the largest gaps in the 5-way configuration were much larger than the largest gaps in the 3-way, a severe handicap if experiments were to produce narrow distributions of gas. We settled on a 4-way as a reasonable compromise, but we consider the optimal geometry to still be an open question. Indeed, if we find that some reconstructions match the ray integrals very well but do not accurately reproduce

the true concentrations, there are only two ways to address that problem, barring algorithmic improvement: either choose a different geometry, or add more rays to the present geometry.

Considerations for future work on choosing a geometry

Although it is standard in CT to choose a geometry based on views (sets of parallel rays), given our equipment there is no need to restrict ourselves to such a geometry. We investigated several geometries not based on views; several of these alternative geometries involve optical paths that intersect at some point inside the measurement plane, giving the appearance of a hub from which rays radiate (though in fact the hub is virtual ---all rays begin and end at the edges of the plane). We performed reconstructions using simulated data for several hub geometries, with different numbers of hubs. Overall performance was inferior to the performance of regular grids.

There is in principle no reason that there must be any regularity or symmetry at all in the ray geometry. Even if a grid based on views is used, there is no requirement that the spacing between rays in a view must be uniform. Indeed, Mohammad Kolachi (personal communication, 1999), has pointed out that Amman lines, a construction used in Penrose tiles, can be used to create a 5-way grid with irregular spacing along each view such that the largest unsampled areas are smaller than the largest unsampled areas in a regular 5-way.

In real-world situations such as monitoring of auditoria or convention centers (or for outdoor monitoring of chemical plants or refineries) it would be highly desirable to use rays that terminate on existing structures. Almost always, this will lead to an irregular path geometry. Indeed, even in our experimental chamber, the position of doors and protrusions into the space preclude use of a completely regular geometry. A quantitative approach to evaluating or estimating the effectiveness of a geometry would be a valuable development for the field of gas CT.

Generating the reconstructions

Most standard methods of computed tomography (CT) are based on picture elements (pixels): a plane of interest is assumed to be divided into a large number of (usually equal) polygons, and it is assumed that the parameter of interest is constant across each polygon. If the number of measured path integrals is larger than the number of polygons, and the spatial distribution of paths is chosen correctly, then in principle each polygon s parameter value can be determined algebraically. In practice, measurement error, temporal variability on a timescale rapid compared to the measurement time, and other factors, can cause minor problems with this approach, and various methods of overcoming these problems have been found (citations here).

Although pixel methods are standard in medical imaging, results from previous research on tracer gas releases (Drescher et al., 1995; Todd et al., 1994) showed that standard pixel methods would not provide satisfactory results for our purposes, for two reasons. First, with only 30 optical paths, we would be limited to rather poor spatial resolution, such as a 6 x 5 array of pixels. Second, the temporal variability in our system is quite large, and many pixel reconstructions could be found that would match the measured ray integrals about equally well. Most such reconstructions would be unphysical, or at least very unlikely, e.g. including very large pixel-to-pixel variability in concentrations across the entire reconstruction plane. In principle, one might be able to find a way of restricting the search to a plausible realm of

parameter space; at this time, however, no such computational methods are available, and pixel reconstructions of gas releases based on sparse path-integral data have been unsatisfactory.

For these reasons, the Smooth Basis Function Method (SBFM) developed by Drescher et al. (1996) was chosen for performing the reconstructions. This method assumes that the methane concentration in the measurement plane, C(x,y), can be written as a superposition of smooth basis functions. The parameters of these basis functions are chosen so that the path integrals for the reconstruction match the measured path integrals as well as possible. In our work, we use two-dimensional Gaussian profiles:

Where γ is a vector of six parameters for each of the Gaussian distributions labeled by *i*:

$$C(x, y) = \sum_i G(x, y; \gamma_i)$$

Ai: amplitude of peak,
Xi, Yi: location of peak,
Sui, Svi: width of Gaussian in u- and v-directions
Thetai: angle between ui-vi axis and x-y axis.

A major advantage of this approach over any previous pixel-based approach is that the resulting reconstructions are smooth, and have a number of local maxima less than or equal to the number of Gaussian basis functions.

- Initial pixel reconstruction

Although pixel reconstructions created by standard methods are unsatisfactory for our purposes, they can be used to obtain initial guesses for the parameters for the Gaussian basis functions. This step is optional, as even poor initial guesses can lead to good final fits if a suitable annealing schedule is used (see below); however, better initial guesses allow use of a more computer-efficient (and thus faster) annealing schedule.

We investigated two types of algorithms for generating pixel reconstructions: the algebraic construction technique (ART), and the pseudoinverse method.

ART is an iterative method that adjusts concentration estimates for sets of pixels upwards or downwards to attempt to match observed ray integrals. There are many decisions that contribute to the final result: how should one pick which pixels to adjust in a given iteration; how should they be adjusted (e.g. by shifting them all by the same absolute amount, by multiplying them all by the same factor, etc.); how many iterations should be performed; how should constraints be imposed (e.g. all concentrations must be positive); and so on.

The Pseudoinverse method, by contrast, attempts an analogy to the fully determined matrix problem: given a vector of y of path-integral measurements, and a system matrix X, on which the jth row contains the path lengths of ray j through each pixel, we wish to find the vector p of pixel concentrations for which y = Xp. If the number of pixels were less than the number of rays, and if the y values were consistent with a reality in which each pixel has a constrant concentration, then this system could be solved with p= Inv(X) y. Even when those conditions

do not hold---when the y values are not consistent with a pixel-like reality, and when the number of pixels is greater than the number of optical paths---one can write p=PseudoInverse(X) y, where PseudoInverse(X) is defined so that the sum of all elements in (PseudoInverse(X)X — I) is minimized. This approach sometimes leads to reasonable reconstructions, or at least a reasonable starting point for reconstructions, in a medical imaging context.

In practice, when applied to our ray geometry neither ART nor the PseudoInverse method generate good reconstructions when used with 120 pixels or more, as checked against simulated data, data from experiments by Drescher (cite), and data from the water model scale water model. However, when the number of pixels was small (e.g. less than twice the number of optical paths) the reconstructions do have some important features of the actual concentration distributions. Specifically, regions with high actual concentrations tend to have high pixel values in the reconstructions.

ART seems to perform somewhat better, and more robustly, than the pseudoinverse method. Tinkering with ART s adjustable parameters (number of iterations, handling of positivity constraints, etc.) caused only minor changes in behavior. For these reasons, we currently use ART to generate initial guesses.

- **Technical notes on our ART implementation**

    1. We start with all pixel values equal to the average path integral divided by the number of pixels.
    2. At each iteration, the ray with the largest absolute difference between predicted and actual ray integral is selected, and all pixels on that ray are adjusted so that the predicted ray integral perfectly matches the measured ray integral; each pixel is adjusted by an amount proportional to the path length through that pixel.
    3. Every 5 iterations, all negative pixel concentrations are set to zero.
    4. The algorithm terminates when the sum of squared errors over all paths is less than a threshold that is inversely proportional to the number of pixels.

- Extracting initial parameter estimates

The point of first doing a pixel reconstruction is to generate initial guesses for the Gaussian parameters, thus speeding up the overall parameter search. The obvious approach to estimating Gaussian parameters from the pixel values is to do a search of parameter space in order to find the superposition of Gaussians that best matches the pixel reconstruction. (Recall that the eventual goal is to find the superposition that best matches the path integrals).

Unfortunately, a full search to match the pixel concentrations takes a large amount of computer resources, thus eliminating much or all of the speed benefit of using the pixel reconstruction rather than going directly fitting the ray integrals.

Instead, we use a very simple method: we place one Gaussian at the location of each local maximum in the pixel reconstruction, with a width of one meter in each direction. Some numerical experimentation leads us to conclude that in practice there is little benefit to extracting

more precise parameter estimates, since the pixel reconstruction is so poor anyway: even if we could find exactly the right parameters to match the pixel values, the final fit would usually change all of the parameters substantially to find the best fit to the ray integrals.

- Using a simulated annealing algorithm to improve parameter estimates

The simulated annealing method works as follows. Values are assigned to all of the Gaussian parameters, and the ray integrals that would result from those parameters are calculated. A measure of mis-fit, e1, between the predicted ray integrals and the measured ray integrals is calculated. Then a new set of parameter values is chosen, and the measure of mis-fit, e2, is calculated. If e2 < e1, then the new set of parameter values yields a better fit, and the new parameter values are accepted---we say that the program has accepted a step in parameter space. If e2>e1, then the second set of parameter values yields a worse fit, but this step may still be accepted subject to the following condition: a uniform random number from 0 to 1 is generated, and is compared to exp[-(e2-e1)/T], where T is an adjustable parameter. If the random number is less than the vale of the exponential, the step is accepted even though it yields a worse fit. This procedure is followed for many iterations. The parameter T, called temperature , is initially set at a large value (large enough that a substantial fraction of steps are accepted even if they lead to worse fits), and T is gradually decreased until only steps that lead to better fits are accepted. This method simulates the statistical mechanical progression through which crystals form, hence the name simulated annealing. It has the enormous advantage over many methods, that it tends not to get stuck at parameter values that yield local, but not global, best-fit solutions. It has the disadvantage, however, of being computationally very intensive: typically thousands or even tens of thousands of iterations are needed in order to find the global best fit.

Our initial hope was to either avoid simulated annealing altogether or to modify the algorithm to substantially increase the convergence speed. Unfortunately, the former goal has thus far proven unattainable: there are too many local best-fit solutions for standard methods to work, such as local gradient searches that begin at many different points in parameter space. On a 300 MHz Pentium II running Mathematica 4.0, a full reconstruction takes about 4 minutes if done from scratch, or about 2 to 3 minutes if a good set of initial parameters is provided.

Choosing initial parameter step sizes and starting temperature

If a very high temperature is used the simulated annealing algorithm, then almost all steps in parameter space will be accepted and any initial information (such as a good first guess from the pixel reconstruction) will be lost. On the other hand, if the initial temperature is too low, then the parameters will quickly settle into a local minimum in model mis-fit and the search for a global minimum will fail. Thus the initial temperature, as well as its rate of decrease, must be chosen with care. The description of how the temperature varies with iteration number is called the annealing schedule.

A related subject is that of the size of the attempted steps in parameter space. Very small changes in parameter values will generally lead to very small changes in the goodness of fit, whereas large changes in parameter values can lead to very large changes in goodness of fit. Recall that the probability of accepting a change in parameter values is proportional to the exponential of the change in model fit divided by the temperature. At high temperatures, it makes little sense to try

small changes in parameter values: a small change in parameter values will change the fit only slightly, so the steps will almost certainly be accepted, so this is just a random walk in parameter space, using very small steps. Conversely, for low temperatures it makes little sense to try large changes in parameter values, because by the time the temperature is low, the system should already be near a minimum in mis-fit, so almost any large change will make the fit much worse and will thus be rejected.

After experimenting with various methods of choosing step sizes and initial temperature, we selected the following procedure. We start by trying modest steps in parameter space: steps in the x or y direction of about 0.7 standard deviations, and changes in standard deviation in each direction of about 50%. In order to preserve some memory of the initial parameter estimates through at least the first part of the simulated annealing run, we need to set an initial temperature so that most steps of this size are rejected; otherwise, the system will quickly wander far from the initial conditions. On the other hand, we need to make sure that some of the steps of this size are accepted, or the system will remain locked in a local minimum and will not explore other, possibly more fruitful, areas of parameter space.

Implementing adaptive step sizes

As discussed above, for reasons of efficiency the size of attempted steps in parameter space should scale with temperature. We use an adaptive method: for each of the six parameters that characterize a Gaussian, we record what fraction of steps at a given temperature have been accepted. If that fraction is large, then the step size for subsequent iterations is increased; if the fraction is too low, then the step size is decreased.

After some experimentation, we settled on a goal of 20%-30% of steps for a given parameter being accepted. At the moment, step sizes for all Gaussian basis functions scale together---e.g., we keep track of the total number of accepted and rejected steps by all Gaussians in the x-direction, and if the fraction of acceptances is too low then we reduce or increase the step size in that direction for all of the Gaussians. A potential improvement would keep track of each Gaussian separately, and thus allow different step sizes for each Gaussian. However, such a procedure would increase the statistical variation in the fraction of accepted steps, because if there are N basis-function Gaussians any particular one is only selected for a possible parameter change 1/N of the time, and a given parameter of a given Gaussian is thus selected only 1/(6N) of the time. If the number of iterations M at a particular temperature is very large, so that I/6N exceeds 15 or so, then the increased statistical variation is probably unimportant, but with our current annealing schedules M is too low to meet this condition.

A hybrid approach is possible: rather than adjusting a given parameter stepsize for all of the basis-function Gaussians at once (as we currently do), or adjusting each of them entirely independently (as discussed above), an approach conceptually similar to a weighted average of these approaches might provide better performance. This is a possible avenue of future research.

Restricting the choice of new parameter estimates

For both computational and substantive reasons, it is desirable to restrict the range of values for some of the parameters. As an example, we do not wish move the peak of a Gaussian far beyond the boundaries of the room, so that only its extreme tail extends into the room and thus

contributes to the predicted path integrals. Although in principle one could construct a real distribution that could best be fit this way, in practice the likelihood of that happening is vanishingly small. Moreover, even if such a distribution did occur, it could be fit nearly as well by using a Gaussian of smaller magnitude, with a peak within or near the boundaries of the room: once the Gaussian has moved outside the room s boundaries, the main effect of moving it still farther away is to decrease its contribution to path integrals in the room. Restricting the search in parameter space to within or near the confines of the room substantially restricts the parameter space that must be explored by the simulated annealing , greatly improving computational efficiency.

There are at least two ways to impose restrictions to the search of parameter space. One way is to use a penalty (energy) function that strongly penalizes parameter choices outside the desirable realm of parameter space. Another is to simply never attempt a step outside the desirable realm of parameter space. The latter is more computationally efficient, so we use it for the entire simulated annealing portion of the fit procedure. (We use the penalty method in a final convergence discussed below).

The specific constraints that we currently use are:

1. If the initial portion of the step trial algorithm selects an x or y position for a Gaussian s center that is beyond the boundary of the room, the trial position is set on the room s boundary.
2. If the initial portion of the step trial algorithm selects a length (the major axis) or width (minor axis) that would make the Gaussian more than three times as long as it is wide, the trial length or width is set so that the length is three times the width. (This prevents the system from finding a solution in which a very long, narrow Gaussian is aligned along a single ray so as to fit that ray s concentration very well; such a concentration profile is very unlikely to occur in reality).
3. If the initial portion of the step selection algorithm selects a width narrower than the width of a typical unsampled area in the geometry, the trial width is set to the width of a typical unsampled area. (This prevents a very small Gaussian from settling on a single ray so as to fit that ray s concentration very well, or from settling into an unsampled area so that it contributes little to any of the path integrals).

Choosing an energy function

As mentioned in the section on performing simulated annealing, for each set of parameters we must calculate a measure of model mis-fit that summarizes, in a single number, how well or poorly the reconstruction fits the ray-integral data. This single number in simulated annealing plays the role of energy in the physical process of annealing. Many choices for such a function are reasonable; the simplest and most natural choices are either the sum of squared errors (SSE) in the predicted path integrated concentrations, or the sum of squared errors in the predicted average concentration along each path. The latter choice is equivalent to a weighted sum of squared errors, where the weights are inversely proportional to the path lengths.

The correct choice of energy function is intimately tied to the statistics of model mis-fit. In fact, in an ideal world in which the statistical behavior of the underlying gas distribution were known

and a statistical model could be selected to match that behavior, the energy function could be determined from first principles. In contrast, our situation is more complicated. We are attempting to write the concentration in the plane as a superposition of a small number of distorted Gaussian functions, but we know in advance that that is only an idealization of the actual situation, though the details of the variation away from this model are unknown and very difficult to estimate. For example, the spatial distribution of gas changes with time, which would introduce complications even if each ray were measured continuously. In the actual experiment the path integrals are measured very briefly and at different times, so a set of measurements that comprises one measurement from each path really represents a temporally and spatially sparse sample from a changing distribution. Finally, there is non-negligible experimental error due to detector noise; this noise is likely to have a larger relative effect on short optical path measurements than on long ones. Given these complications, it is impractical to construct a statistical model of the relationship between the pollutant distribution and the path integrals that could be used to determine the optimal measure of model fit. We instead consider the two natural measures mentioned above: SSE, and weighted SSE.

A possible drawback of using the SSE of path integrals is that this measure usually lends little influence to relatively short optical paths; to consider a greatly simplified example, if the concentration is nearly uniform across the room then the measured path integrals will be nearly proportional to path length.

If a measurement of a short optical path indicates that the integrated concentration along the path is low, then we might hope that the reconstruction based on all of the data would put a low concentration in the area covered by that optical path. But if the SSE of the path integrals is used, then reconstruction can put substantial concentration in that area if it helps to match the other path integrals well, even though we are quite sure that the concentration there is low. Based on this observation, it seems that using the SSE in the average concentrations (rather than the SSE in the path integrals) might be a better choice, since the shorter paths will then get relatively more emphasis. But in fact, this raises some problems of its own. The principal problem is the converse of the problem this approach is intended to solve: the reconstructed concentration in the middle of the room can be substantially affected by the measured average concentrations in the corners, where the optical paths are short---a case of the tail (of the distribution) wagging the dog. Tests using data from the water model suggested that using the SSE in the path integrals was a more robust method, in spite of its shortcomings, so that is what we currently use. An uninvestigated possibility would be to use a compromise. The SSE in path integrals assigns each integral equal weight, while the SSE in path-average concentrations assigns each a weight inversely proportional to the path length. Perhaps an approach in between these two (e.g. weight inversely proportional to a fractional power of the length) would work better than either of the extremes.

Terminating Simulated Annealing

As discussed above, as the temperature parameter in the simulated annealing method decreases our adaptive step size method will gradually decrease the size of attempted steps in parameter space so as to maintain a specified fraction of accepted steps. Once these attempted steps become small, the system has settled into a set of parameter choices that cannot change substantially. Rather than use a termination condition based on temperature (as is common, but

by no means universal, in simulated annealing applications) we terminate the simulated annealing algorithm when the step sizes for all of the parameters other than angle represent substantively small changes in value: when attempted changes in location are less than 20% of the width of the Gaussian, and when the attempted changes in length and width are less than 20% of those parameters values. We ignore angle in the evaluation of convergence because if the length is nearly equal to the width then changes in the angle will have virtually no effect on the path integrals, so even if the changes in angle are still rather large this does not necessarily indicate that these changes represent truly different solutions. If, instead, the length and width are substantially different, there is still no need to consider the angle, because if the length and width have settled into their final values then angle will have done so as well.

Final convergence

After exiting the simulated annealing algorithm, a local gradient search is performed (using Powell s algorithm (Press et al., 1986) to obtain final convergence. For this search, it is inconvenient to add restrictions on the parameters in the way that is used for simulated annealing as discussed. Instead, a multiplicative penalty is used to penalize very narrow Gaussians, Gaussians outside the boundaries of the room, and so on. This penalty function has the following characteristics:

1. An (x,y) location of the Gaussian center that is outside a specified area slightly larger than the dimensions of the room is heavily penalized;
2. Gaussian widths greater than _ the average room dimension, or less than 1/20 of the average room dimension, are heavily penalized;
3. Gaussians that are wider than 1/20 of the average room dimension, but are narrower than about 1/5 of the average room dimension, are weakly penalized;
4. Negative amplitudes of the Gaussians are weakly penalized;

Parameter values should (and usually do) change relatively little at this point of the procedure, but the Powell search adds only about 15% to the computation time, so there is no reason not to do it. On rare occasions, the Powell search leads to a substantially better solution than was found with simulated annealing alone.

Results and Discussion

Figures 3 and 4 show reconstructions from a methane release in the large experimental chamber. Each figure shows the output of a graphics program that is used to visualize the reconstructions and the extent to which the reconstructions match the short-path measurements. The first two lines of text show the time interval over which the long-path and short-path data used for the figure were collected. The next lines on the left show the highest measured short-path integral and the highest predicted concentration in the plane (whether or not the location of that concentration coincides with a short-path measurement); on the right, the correlation between short-path measurements and predicted short-path concentrations is displayed, as is the correlation for the long-path measurements. Finally, in each figure, the left-most plot shows the CT reconstruction as a contour plot, superimposed with average concentrations measured along 28 short (0.5m) optical measurement devices suspended in the chamber. These short-path concentrations provide a validation set for the reconstructions. In Figures 3 and 4, both the long-path data used for the reconstructions and the short-path data used for validation are constructed

from two complete scans of the room: each optical path is measured once every 7 seconds, and the data used for each reconstruction uses data collected within a 15-second interval (during which optical path is measured at least twice). The rightmost scatter plot in each figure compares the reconstructed and measured concentration for the short-path sensors.

Figures 3 and 4 show data and reconstructions for consecutive 15-second intervals. In both cases, the reconstruction agrees extremely well with the measured long-path integrals (correlation r=0.96 for figure 3, r=0.98 for figure 4), but in Figure 3 the agreement between the predicted and measured short-path concentrations is only fair (r= 0.71). In contrast, the predictions for the short-path concentrations in Figure 4 are very highly correlated (r=0.89) with the actual measurements. What causes this difference?

One possibility is that temporal variability in both short- and long-path measurements during the 15-second period leads to a mismatch between the reconstruction and the short-path measurements. This mismatch is itself variable over time, depending on specifics of the plume movement during the scan and the sequence in which the ray integrals are measured.

To see the effects of temporal variability during a scan, we return to water model data, since they give us concentrations at a high spatial resolution and all at the same time (in contrast to short-path measurements in the large air experiments, that give only rather low spatial resolution, over a measurement interval of 7 seconds). Figure 5 shows three photographs from the water model, showing a plume of high-concentration dye in the upper right, representing methane in the full-scale experimental chamber. The region of high concentration changes slightly from the first image (representing t=0s in air) to the last (t=6s).

Although the overall plume movement is small, concentrations vary enough in time that a short-path measurement will not necessarily reflect the average concentration at that location over a 7-second interval, as can be seen in a few places in figure 6: for several of the short-path sensor locations in the upper right of the plot, the short-path measurement from a particular instant (displayed as a colored rectangle on the plot) differs from the average over the entire 7-second time period (displayed on the underlying contour plot). This implies that even if the CT reconstruction provided a perfect map of the time-averaged gas concentrations over an interval, this map would still not perfectly match the short-path measurements. Of course the temporal variability does not just affect the short-path measurements; it affects the long-path measurements as well: a narrow, rapidly-moving plume of gas can be missed by all of the long-path measurements, in which case the reconstruction for that time interval will not reflect the presence of that plume. However, the issue of temporal variability is less important for reconstructions based on long-path data than for the short-path measurements, since each area of the plane is intersected by several long paths, all of which would have to miss the plume in order for it not to appear in the reconstruction.

As figure 6 illustrates, even when the gas concentration has quite large spatial gradients and is varying substantially with time, the reconstructions from SBFM are in quite good agreement with the actual concentration map. Of course the spatial structure cannot be reproduced on a finer spatial scale than is sampled by the long optical path measurements, but the larger spatial

features are well reproduced, as indicated by the high correlation between actual and reconstructed short-path integrals.

Experience with reconstructing many hours of actual data from the full-scale tin box experimental facility has demonstrated that the tomographic methods can be relied upon to map the actual gas concentrations fairly accurately, with the coefficients of determination between short-path measurements and the reconstructions usually in the range r^2= 0.6 to 0.8.

REFERENCES

Drescher, A.C., Park, D.Y., Yost, M.G., Gadgil, A.J., Levine, S.P., Nazaroff, W.W. (1995) Stationary and time-dependent indoor tracer-gas concentration profiles measured by OP-FTIR remote sensing and SBFM computed tomography. Atmospheric Environment 31:727-740.

Drescher, A.C., Gadgil, A.J., Price, P.N., Nazaroff, W.W. (1996). Novel approaches for tomographic reconstruction of gas concentration distributions in air: use of smooth basis functions and simulated annealing. Atmospheric Environment 30:929-940.

Natterer, F. The mathematics of Computed Tomography. John Wiley and Sons, New York, 1986.

Press, W.H.; Flannery, B.P.; Teukolsky, S.A.; Vetterling, W.T., Numerical Recipes. Cambridge University Press, Cambridge, 1986.

Price, P.N. (1999) . Pollutant tomography using integrated concentration data from non-intersecting optical paths. Atmospheric Environment 33:275-280.

Radon, Johan. ‘‘ ber die Bestimmung von Funktionen durch ihre Integralwerte l ngs gewisser Mannigfaltigkeiten.’’ Ber. Verh. S chs. Akad. Wiss. Leipzig, Math-Nat. 69 (1917) 262-277.

Todd, L.A. and Ramachandran, N. Evaluation of algorithms for tomographic reconstruction of chemical concentrations in indoor air. American Industrial Hygiene Association Journal 55:403-417 (1994).

Yost,M.G., Gadgil, A.J., Drescher, A.C., Zhou, Y. (1994). Imaging indoor tracer-gas concentrations with computed tomography: experimental results with a remote sensing FTIR system. American Industrial Hygiene Association Journal 55:395-402.

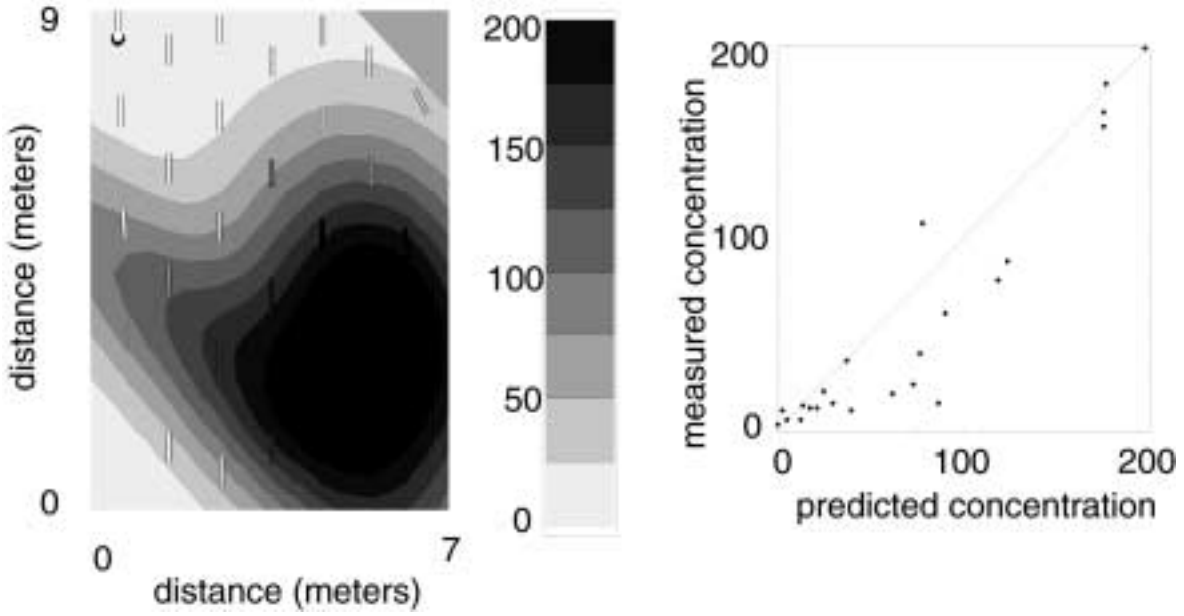

Figure 3. Left: contour plot showing reconstructed distribution, with short-path measurements superimposed (narrow bars). Where the short-path measurement agrees closely with the prediction, the short-path bar blends with the background and is not visible. Right: Scatter plot showing measured vs predicted short-path measurements.

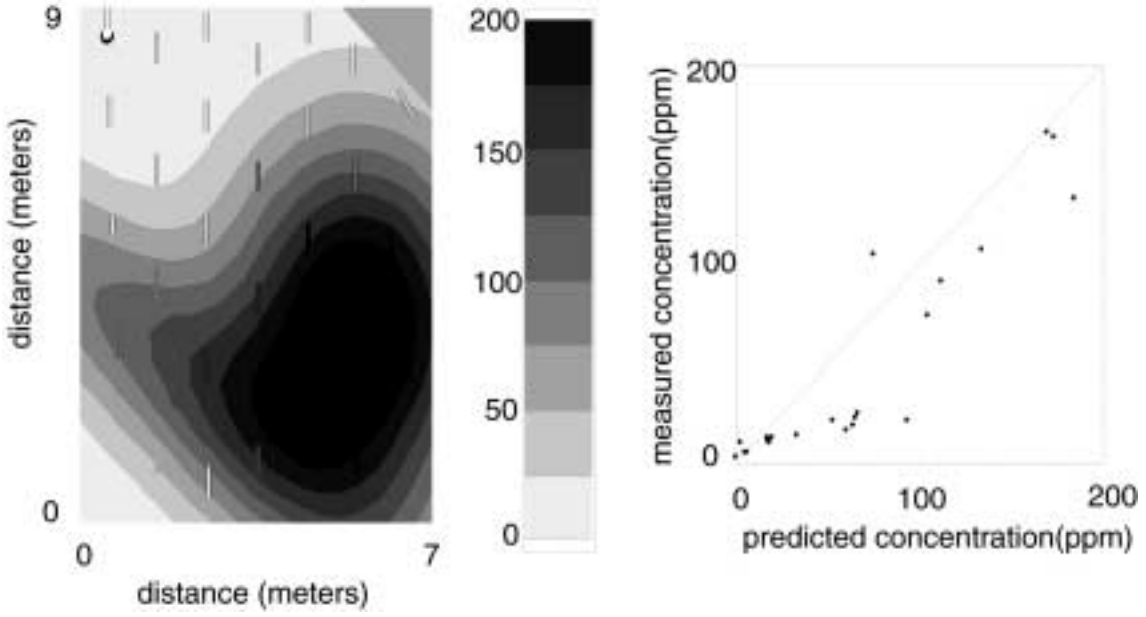

Figure 4. (a) Contour map of CT-reconstructed methane concentrations, with short-path measurements superimposed. (b) Scatterplot comparing measured and predicted short-path concentrations.

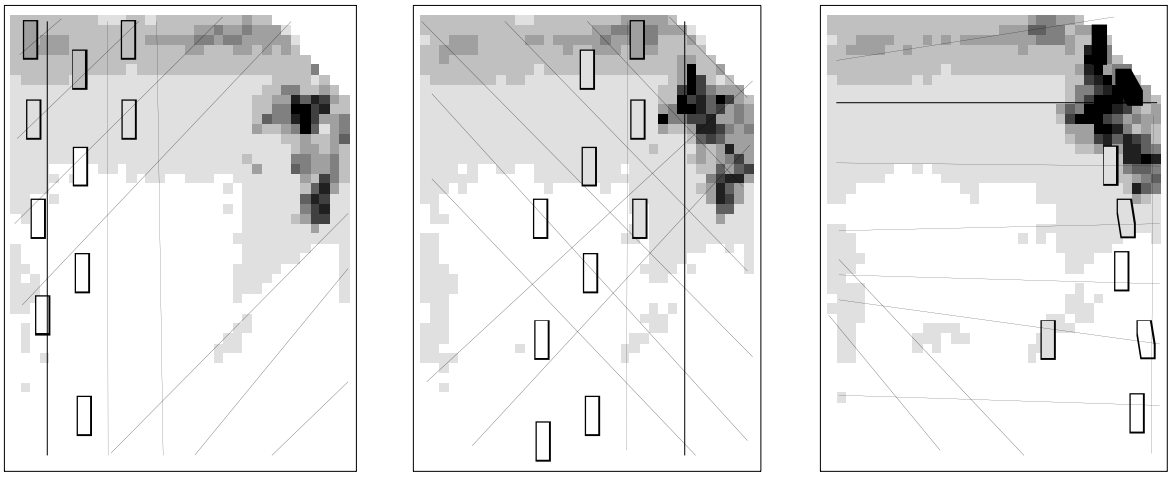

Figure 5. Three photographs of dye in the water tank scale model. These photos represent methane concentrations in air at t=0s, t=3s, and t=6s. Superimposed on each photo, we show the average concentration along a set of short-path sensors (small outlined boxes). These represent the short-path measurements that would be obtained if these short-path sensors were measured at the instant shown in the photo. Also superimposed are the long paths corresponding to the long-path integral measurements made in each time interval.

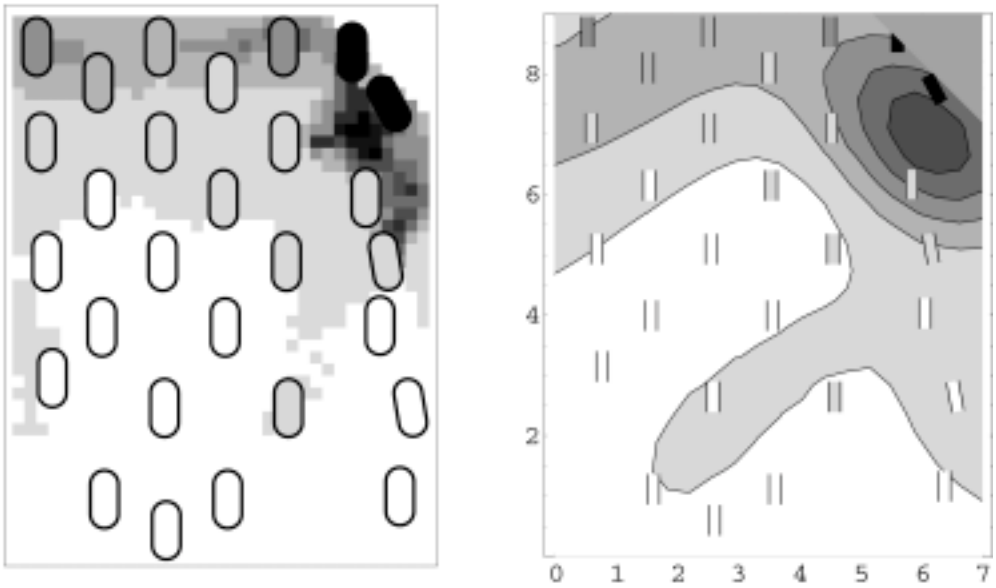

Figure 6: Left figure: average of the three photographs shown in Fig. 5, displayed as a contour plot, with short-path measurements superimposed. The underlying contour image is a time-average, but each short-path measurement was taken from a particular instant (that is, from one of the three photographs in Fig. 5). Motion of the dye causes a mis-match between the short-path measurements and the average concentrations; in particular, see the fourth short-path sensor from the bottom in the rightmost row. Right: reconstructed concentration distribution, based on long-path ray integrals shown in Fig. 5.

IV. SMALL-SCALE EXPERIMENTS

An approximately 30:1 scale water model of the large-scale indoor facility described in Section II is used to investigate pollutant dispersion in these experiments. A schematic of the model is shown in Figure 1. The water model is built inside a 20 gallon tank divided with a partition. One side of the partition houses the scale model, while the other side provides a container from which the overflow water can be removed. The upper surface of the tank is a free surface with no lid or ceiling.

Figure 1: Overhead View of Model Layout

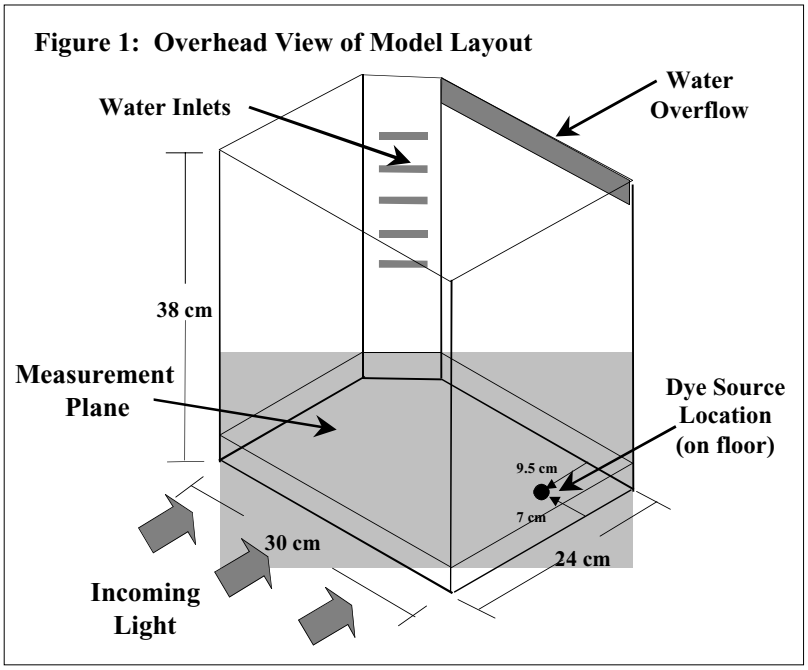

During an experiment, dye-free water flows into the model through the water inlets. All of the experiments described in this section were conducted in a single pass configuration (no recirculation of water from the overflow) with a water flowrate of 28 lpm, which is approximately one tank volume per minute. A pollutant spill or release is simulated using a uranine (sodium fluorescein) dye solution introduced into the tank just above the floor in the position shown in Figure 1. Uranine dye, at a concentration of 10 mg/l, flows through a 5 mm diameter foam ball at a flowrate of 1 cc/s. A constant dye flowrate was obtained using a peristaltic pump. The water and dye exit the model through the overflow weir.

An intense sheet of blue-green light 1 cm thick and centered 6 cm from the floor of the water model is formed by spreading the beam from a 5 watt, argon ion laser (Spectra Physics, model 168). This plane is just above the heads of people in model scale. The incoming laser light causes the uranine dye to fluoresce, i.e. emit light of a different wavelength. The amount of fluorescence emitted at any location is directly proportional to the product of the local dye concentration and the local intensity of the laser light. A black and white video camera (Hitachi, KP-M1) mounted directly above the tank records the light emitted from (and therefore the dye concentration in) the plane. This camera responds linearly to changes in light intensity, allowing the use of a linear calibration scale. Since the excitation wavelength for uranine (which causes the dye to emit light) is different than the wavelength of the emitted light, the dye in the region above the measurement plane does not attenuate the light that reaches the camera. A selective light filter (Kodak Wratten 15) prevents scattered or reflected laser light from reaching the camera, so that only light emitted by the dye is measured.

The images from the camera are digitized using a personal computer (Micron Electronics, Client Pro) connected to a capture board (Grabit Pro, Aims Laboratory) capable of recording higher resolution still images at 1 frame per second or lower resolution video at 5 frames per second. In addition to the images from experimental runs, images are also recorded which represent background conditions (with no dye present) and selected well mixed concentrations of uranine dye.

The digitized images are imported into an image processing program (Scion Image, Scion Corporation) where they are cropped and the background is subtracted. Since the light intensity in the plane is not uniform, a flat field correction is applied. This is performed by dividing the measured intensity at each pixel in the image by the measured intensity at the same pixel obtained from an image of uniform dye concentration. The images are then digitally smoothed to reduce the effect of camera noise. The smoothing process replaces the values in a 5 pixel by 5 pixel square with the average of those 25 pixels. The average light intensities for several different well mixed concentrations of uranine dye are used to produce a calibration curve. This calibration showed a linear light intensity response over the concentration range used in these experiments.

Theory of Scale Modeling

Turbulence theory provides insight into the appropriate flow conditions and time scale for matching water model results to the results from the ATRIUM. Performing the scaling transformation requires an understanding of the factors affecting turbulence both within the full scale room and the model. For the experiments performed here, only mechanical ventilation effects are investigated; the experimental plan was restricted to a neutrally buoyant plume with isothermal flows and surfaces. Therefore, we can describe turbulence in terms of the Reynolds number. We will look at both flow from the inlets and general flow within the room. Ideally, a scale model would exactly match the Reynolds numbers for the larger space being emulated. However, in practice this is not always easily achievable. When Reynolds numbers do not match exactly, it is possible to use turbulence theory to estimate the differences between model and full scale results.

In order to analyze the scale model, we must first define length, velocity, and time scales for both the inlets and room. For this analysis, we define these scales in terms of the physical dimensions and flowrates as follows:

Length Scales		Velocity Scales		Time Scales	
$S_{inlet} \equiv A_{inlet}^{1/2}$	(1)	$U_{inlet} \equiv Q_{inlet}/A_{inlet}$	(2)	$t_{inlet} \equiv A_{inlet}^{3/2}/Q_{inlet}$	(3)
$S_{room} \equiv V_{room}^{1/3}$	(4)	$U_{room} \equiv Q_{inlet}/V_{room}^{2/3}$	(5)	$t_{room} \equiv V_{room}/Q_{inlet}$	(6)

Where:

$S_{inlet\ or\ room}$	=	representative length scale, m
A_{inlet}	=	area of the inlet, m^2
V_{room}	=	room volume, m^3
$U_{inlet\ or\ room}$	=	representative velocity scale, m s^{-1}
Q_{inlet}	=	volumetric flowrate through the inlet, m^3 s^{-1}
$t_{inlet\ or\ room}$	=	representative time scale, s

Based on these definitions, we can express the Reynolds numbers, $Re_{inlet\ or\ room}$, as:

$$\mathrm{Re}_{inlet} = \frac{U_{inlet} S_{inlet}}{\nu} = \frac{Q_{inlet}}{A_{inlet}^{1/2} \nu} \tag{7}$$

$$\mathrm{Re}_{room} = \frac{U_{room} S_{room}}{\nu} = \frac{Q_{inlet}}{V_{room}^{1/3} \nu} \tag{8}$$

where ν is the kinematic viscosity, $m^2\ s^{-1}$, for the fluid.

For a perfect match, both the inlet and room Reynolds numbers in the model should be the same as those for the full scale chamber. For the inlet, this condition is met if:

$$\frac{Q_{inlet,full}}{A_{inlet,full}^{1/2} \nu_{air}} = \frac{Q_{inlet,model}}{A_{inlet,model}^{1/2} \nu_{water}} \tag{9}$$

For the room this condition is met if:

$$\frac{Q_{inlet,full}}{V_{room,full}^{1/3} \nu_{air}} = \frac{Q_{inlet,model}}{V_{room,model}^{1/3} \nu_{water}} \tag{10}$$

If the defined length and velocity scales are substituted into these equations then both equations become:

$$\frac{Q_{inlet,full}}{Q_{inlet,model}} = \left(\frac{S_{full}}{S_{model}} \right) \left(\frac{\nu_{air}}{\nu_{water}} \right) \tag{11}$$

This means that, for a model where the room and inlets are scaled by the same factor, a solution for Reynolds number matching of the inlet will also match the Reynolds number for room flow under all mechanically driven flow conditions. This equation can be solved knowing that the ratio of the kinematic viscosities of air and water is approximately 12 and the ratio of the length scales in these experiments is 30. Therefore, perfect matching of the room and inlet Reynolds numbers occurs when the volumetric flowrate in the full scale room is 360 times the volumetric flowrate in the model.

The time scale for Reynolds number matching can be determined from the time scale definitions as:

$$\frac{t_{room,full}}{t_{room,model}} = \frac{\left(\frac{V_{room,full}}{Q_{inlet,full}}\right)}{\left(\frac{V_{room,model}}{Q_{inlet,model}}\right)} = \left(\frac{S_{room,full}}{S_{room,model}}\right)^3 \left(\frac{Q_{inlet,model}}{Q_{inlet,full}}\right) \qquad (12)$$

For the 30:1 scale model used in these experiments, this gives a time scale of 75:1. Therefore, one second of flow in the model would simulate 75 seconds of flow in the full scale room. Since in the full-scale experiments the desired air exchange rate is 4 air changes per hour, this means that Reynolds number matching is achieved with the water model operated at 300 volume changes per hour or one volume change every 12 seconds.

Although it would be possible to operate the water model at these high flowrates, several factors complicate the process. First, a high speed image acquisition system would be required for capturing the data with a reasonable time resolution. Second, the flowrates and pressures within the model would require large pumps and significant structural reinforcement. Finally, operation in a single pass mode would require either a large water storage system or a high capacity water source. Fortunately, turbulence theory shows us that, under fully turbulent flow conditions, reducing the model Reynolds number has very little effect on the correlation between the model and full scale results. Given the difficulties in operating the model with an exact Reynolds number match, we choose to run the model at a lower flowrate and a lower Reynolds number, but still with fully developed turbulent flow.

In turbulent flow, eddies within the fluid transport and disperse contaminants. The size range for the eddies in any given system is a function of the physical and flow characteristics within that system. The larger eddies in the system contribute most to the kinetic energy and comparatively little to the viscous dissipation. Conversely, the smallest eddies are primarily responsible for viscous dissipation. Experiments show that the size and structure of the eddies in a fully developed turbulent flow are not strongly influenced by the Reynolds number. Townsend (1976, p53) states that:

> Perhaps the most significant fact about turbulent flows is that, while geometrically similar flows are expected to be dynamically and structurally similar if their Reynolds numbers are the same, their structures are also very nearly similar for all Reynolds numbers which are large enough to allow turbulent flow.

The major effect of lowering the Reynolds number is to increase the size of the smallest eddies in the system. The magnitude of this increase can be estimated by looking at the ratio of the sizes of large and small eddies, given as (D. Wilson, private communication):

$$\frac{\ell}{\eta} = \left(\frac{u_s \ell}{\nu}\right)^{3/4} \qquad (13)$$

where l is the size of the largest eddies, η is the size of the smallest eddies, u_s is the rotational velocity of the turbulent eddies, and ν is the kinematic viscosity.

The size of the largest eddies, l, depends on the physical dimensions of the enclosure. Based on physical reasoning, we estimate the largest eddies to be 0.1 times the length scale, S, for our calculations. Similarly, physical intuition suggest that the turbulent velocity should be some fraction of the flow velocity at the inlet vents: we will use 0.1 times the inlet velocity. Using these values, the smallest eddies in the full scale room are 0.38 cm. When we run the model at 28 lpm (20% of the flow needed to match Reynolds numbers), the smallest eddies in the model are 0.028 cm. Multiplying by 30 to scale these eddies to their equivalent full scale size yields a value of 0.84 cm. This means that concentration features which are smaller than 0.84cm in the full scale room will not be well described by the scale model results. Since our image resolution is approximately 0.1 cm, we will not be able to capture the differences caused by the loss of eddies in the model (those smaller than 0.028 cm). Therefore, the lowering of the Reynolds number will have an imperceptible effect on the observational data.

Based on our volumetric flowrate of one model volume per minute, the time scale for the model is 15:1. This means that 1 second in the water model is equivalent to 15 seconds in the full scale room.

Experimental Design

Three different configurations of the model interior are used for these experiments. In the first set of experiments, the interior of the model is unobstructed, containing only the dye source and a small tube running along the floor connected to the peristaltic pump. In the second set of experiments, five obstructions representing rows of tables are placed on the floor of the model in parallel rows. For the third set of experiments, twelve obstructions with the approximate dimensions of human adults are placed on the model floor in addition to the table-like obstructions. The human-like obstructions are not heated and therefore do not capture the effect of the thermal plumes caused by real people. A schematic of the obstructions is shown in Figure 2. An overhead view of the layout of these obstructions within the model is shown in Figure 3.

Figure 2: Schematic of Obstructions

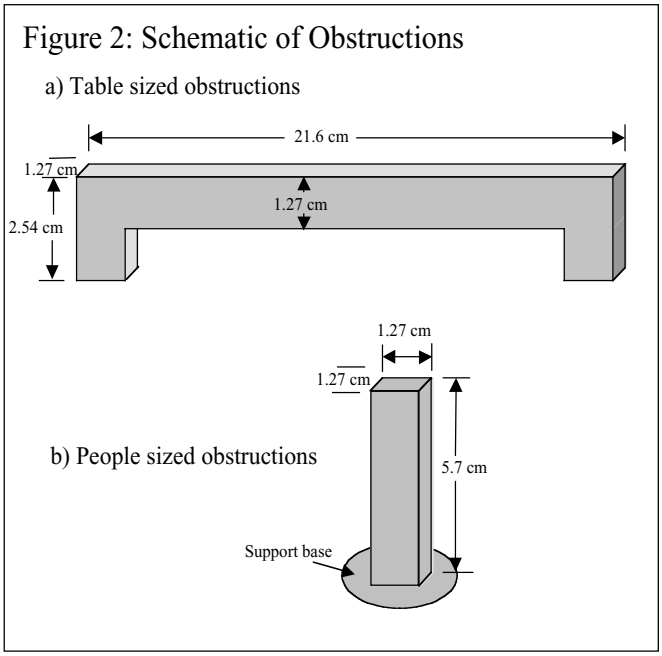

Experiments are performed to investigate dye concentrations in the measurement plane under both transient and fully developed conditions. For all measurements, the flow field was established prior to beginning dye injection, starting at least 3 minutes, 3 volumes of flow before the dye was injected (3 volumes of flow). Since each run represents only one realization of a

highly variable and stochastic process, capturing a statistical representation of the developing flow requires multiple runs for a given set of flow conditions. In these experiments, we typically captured 20 replicate runs for both 5 frame per second lower resolution video and 1 frame per second higher resolution images. Each of these realizations contains approximately 1000 frames.

Figure 3: Overhead View of Model Layout

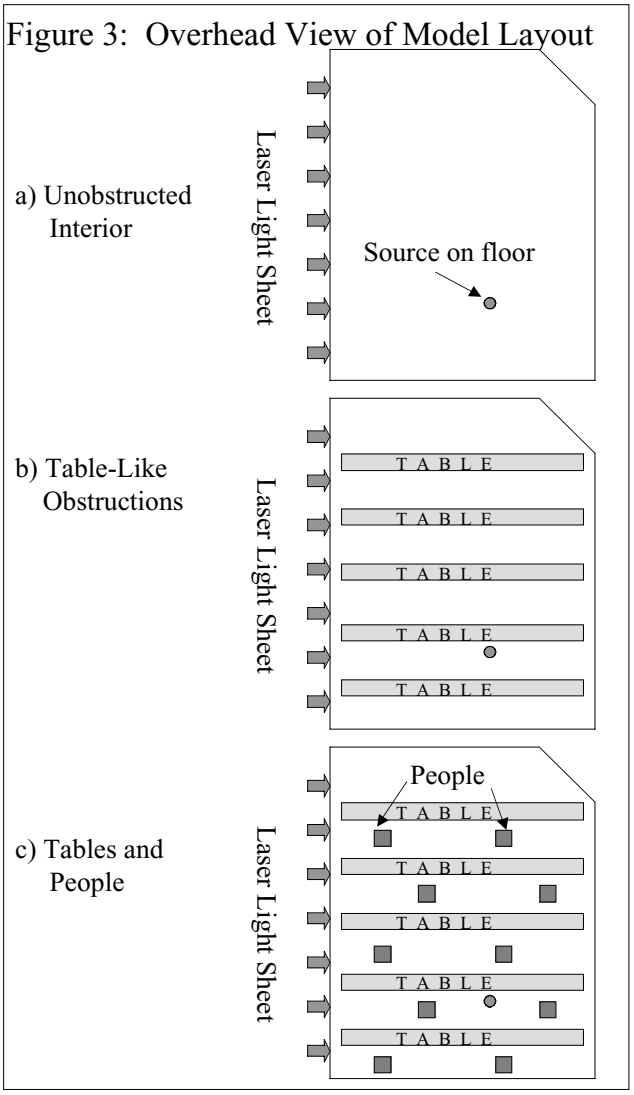

For experiments with fully developed concentration profiles, dye injection was initiated 5 minutes prior to beginning image collection. Then, one image was collected every 3 seconds for 50 minutes (1000 images). The average concentration images shows the average value at each pixel for a given set of data. The fluctuation intensity image represents the standard deviation of the values at each pixel divided by the average concentration at that pixel. Comparisons between the results from replicate sets of images showed that 1000 images provided a sufficient number of independent profiles to characterize the concentration and fluctuations accurately.

4. Results and Discussion

Results from the transient experiments in the unobstructed model are shown in Figure 4. The images were taken at 1 second intervals starting 6 seconds after the initiation of dye discharge. Each image in Figure 4 represents the average of 19 concentration images, each from a different run, taken at the same elapsed time after the start of dye injection . This sequence demonstrates the evolution of the average concentration in the image plane with time. Dye first appears in the image plane approximately 5 seconds after dye flow starts. In addition to the growth of the plume in the plane with time, consecutive frames (e.g. 9 seconds, 10 seconds) show fluctuations, demonstrating that there are not a sufficient number of replicates to obtain well defined profiles for the developing flow. However, the replicates are sufficient in number to provide a reasonable sense of the time evolving average concentration profile.

Even after the concentration distribution becomes fully established, the stochastic nature of the flow results in large changes in the instantaneous concentration profile in the measurement plane over time. However, the time-averaged concentration profile is stable. To obtain meaningful time-average concentration profiles, a large number of independent images need to be averaged.

Figure 4: Average concentration profiles in the measurement plane (from 19 runs). Time reflects elapsed time after initiating dye injection. Darker grays indicate higher concentrations.

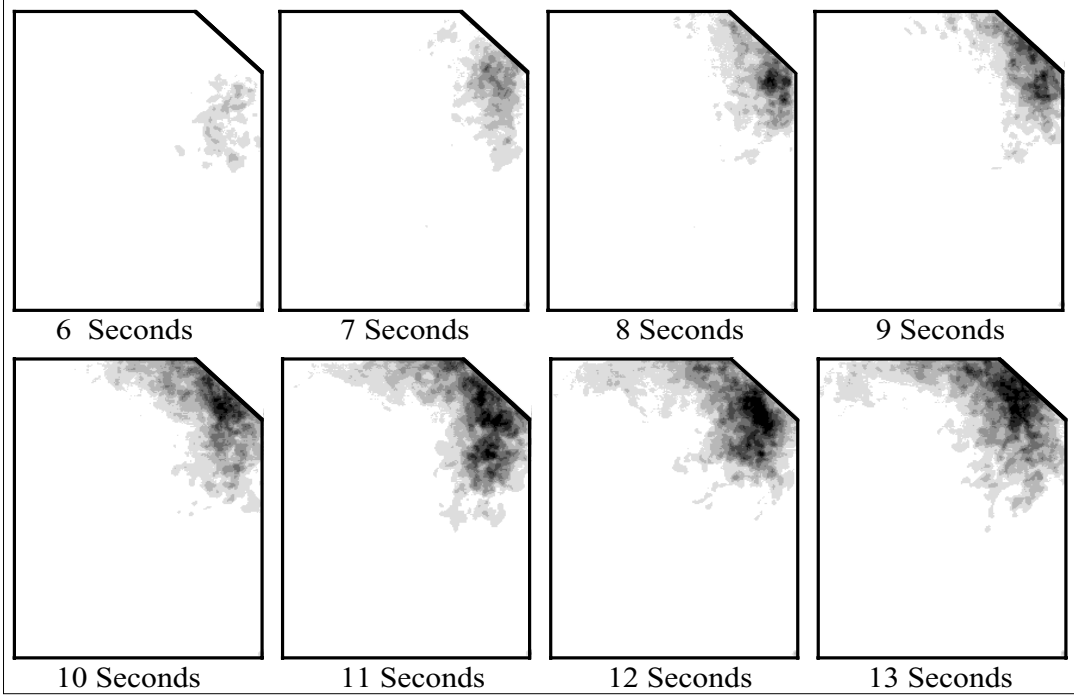

Figure 5: Increasing numbers of images used in averaging the instantaneous concentration profiles for fully developed flows.

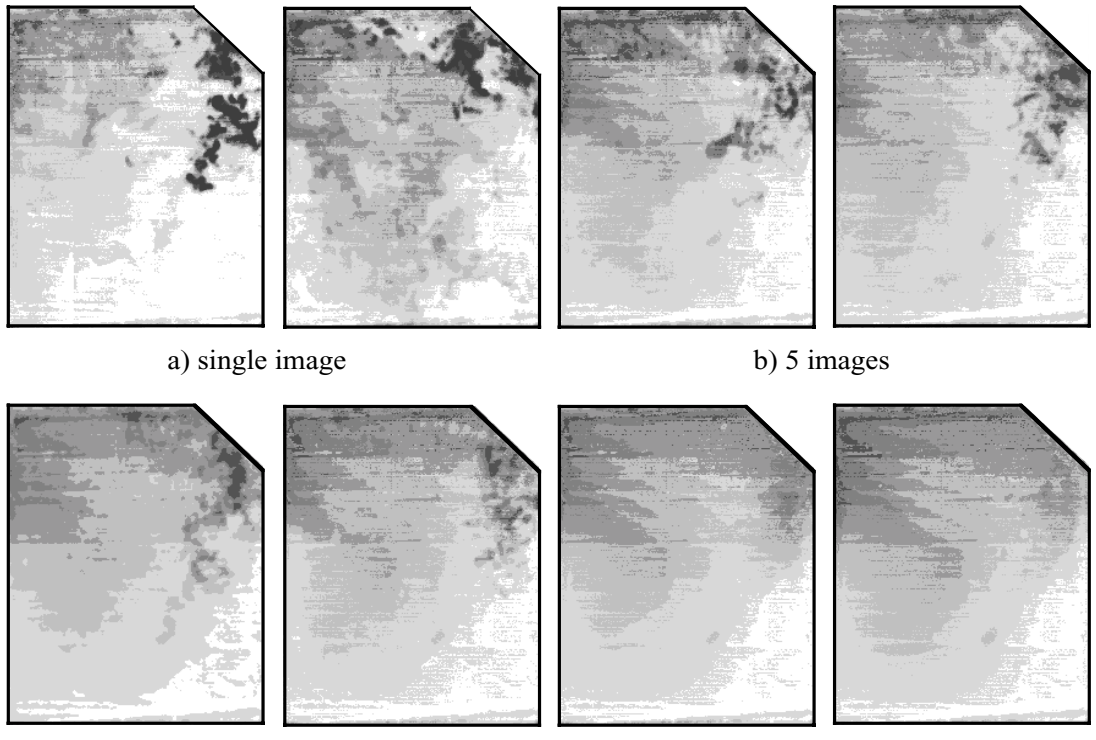

Figure 5 illustrates this point by showing the concentration profile obtained by averaging between 1 and 200 images for a fully developed concentration profile for the unobstructed model. There are two images shown for each of the four different number of frames being averaged (1, 5, 10, and 200 frames). Each of the two average images was obtained using different independent sets of frames from a single experiment. When a small number of frames is averaged, the concentration profile is dependent on which frames are used for the average. As a larger number of frames is used, the images converge to a consistent average concentration profile. For a large enough sample, the average values should be identical.

Figure 6: Comparison of the averages from two separate experiments of 1000 frames each. In both experiments, table and human obstructions were present and experimental conditions were duplicated.

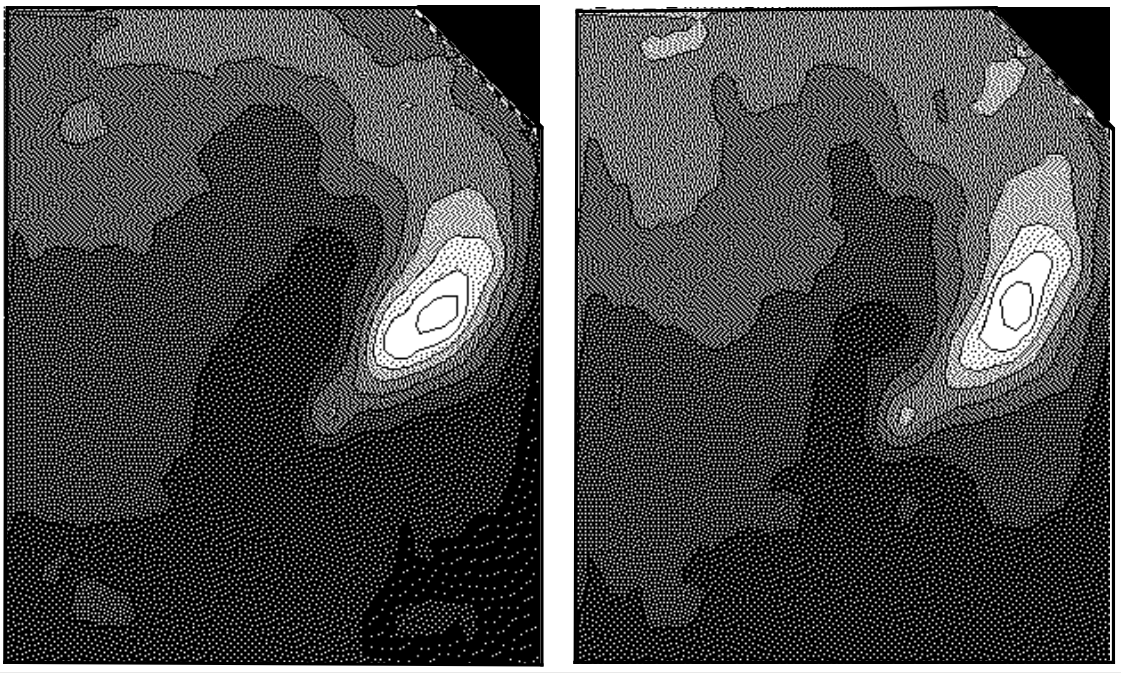

When the results from two separate runs with the same experimental conditions are compared, the averages are similar in the location, shape, and magnitude of the concentration features. Figure 6 shows the average concentration maps obtained for 1000 frames from two separate runs for the configuration with bench-like and human-like obstructions.

The effect of obstructions can be seen in Figure 7. The three images show the time-average, fully developed concentration profiles for the three configurations studied: (1) unobstructed, (2) with 5 long tables, and (3) with 5 long tables and 12 humans. Each image is the average of 1000 frames taken from the same run. These images show that obstructions of the sort that are typically found in rooms can have a significant impact on the average concentration in the measurement plane, even in the absence of thermal plumes. The presence of obstructions increases the overall concentration in the measurement plane, increases the peak concentration in the plane, and shifts the areas of highest concentration. Other configurations of obstructions would almost certainly cause different changes in the concentration profiles and could

conceivably even reduce the average concentration in the plane. The important point is not so much the actual concentration profiles, which would vary with the type and location of the obstructions, but more the magnitude of the effects seen. When human figures are present, videos of the time sequence of dye release show dye rising up along the figures near the source and entering the measurement plane from the top of the figure. We also see that, when table obstructions are present, the dye spreads more below the measurement plane and enters the plane as a plume with a larger cross-section.

Figure 7: Time-average of 1000 images from fully developed concentration profiles with three different levels of obstructions on the floor of the model. Concentrations are normalized to the average, fully developed outlet concentration.

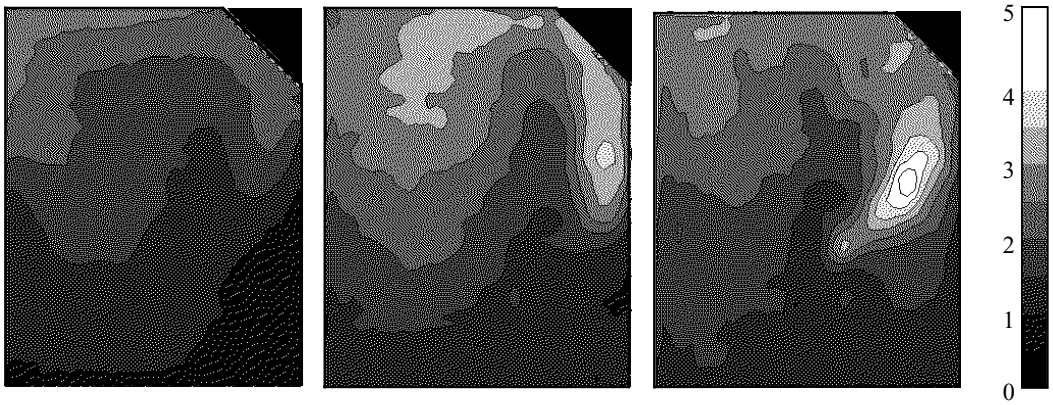

a) unobstructed b) 5 tables c) 5 tables and 12 humans

Figure 8 shows the fluctuation intensity in the measurement plane for the three configurations studied. These images show a shift in both the location and strength of the fluctuation intensity when obstructions are added. The fluctuation intensity increases when tables are present, but decreases when humans are added along to the tables.

Figure 8: Time-average fluctuation intensity of 1000 images from fully developed concentration profiles with three different levels of obstructions on the floor of the model.

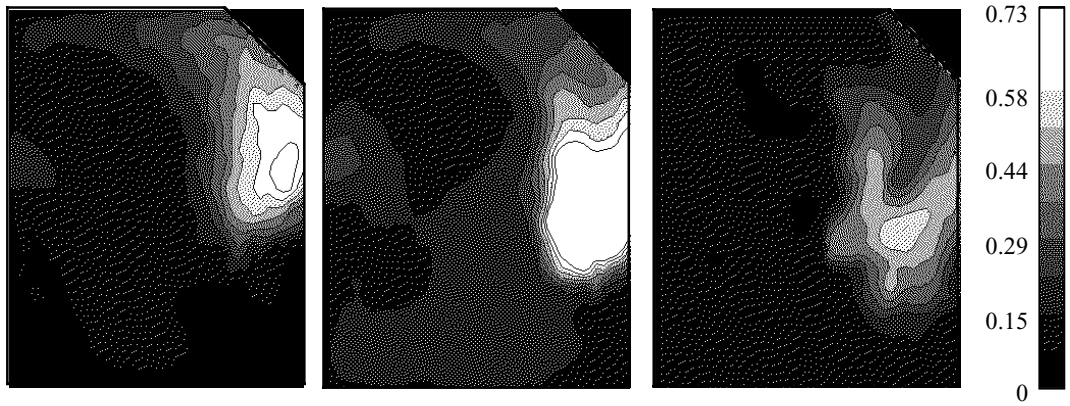

a) unobstructed b) 5 tables c) 5 tables and 12 humans

Based on visual observation of the flow patterns, the fluctuation intensity decrease with humans is due to plume rise along the human figures, which localizes the positions where the plume enters the measurement plane and decreases the variability.

Future Directions

The use of a water-filled scale model for visualizing flow within a full scale facility has proven to be very helpful for providing high resolution experimental data for comparison to the Computational Fluid Dynamics models and computed tomography reconstructions. In addition, visualization of the flow has provided insight into experimental design of and interpretation of data from the full scale facility. Water-filled scale models are particularly well suited for investigating mechanically driven flow. They have also been used with some success in other applications for buoyancy driven flow. However, due difficulties in achieving full similarity for both mechanical and buoyant flow simultaneously, the method is significantly limited in its applicability to mixed flow conditions, where buoyant and mechanical forces are both important.

In the future, this method could be used to provide benchmark solutions for a two dimensional flow field for an indoor room geometry. This information is of particular interest for providing data to facilitate model comparisons between Large Eddy Simulation, RANS CFD, and Zonal methods. Another interesting application of the scale model is as a diagnostics tool for specific locations of high interest and as a screening method for building ventilation retrofit designs.

V. COMPUTATIONAL FLUID DYNAMICS MODELING

The computational fluid dynamics (CFD) group within the Interiors Project focused its efforts first on code and hardware selection and later on defining and obtaining preliminary results for three different enclosure configurations. This summary contains two parts. The first part is an updated version of a conference paper (Gadgil at al. 1999) and summarizes the first six months of work within the CDF group. This paper covers the code and hardware selection process. The second part describes the progress with the CFD simulation of flow and dispersion in three different enclosures during the calendar year of 1999.

Part I — Selecting Commercial CFD Software for Modeling a Pulse Release of Pollutant in a Large Indoor Space

Computational fluid dynamics (CFD) has been used for many years to model temperature distributions and airflow in buildings with mixed success (Chen, 1997 and Baker, 1997). We are interested in the early phase of the pollutant release when the room is imperfectly mixed. Much of the research on pollutant dispersion has relied on the assumption of a well-mixed room (Nazaroff et al. 1993). However, it is known that this assumption can underpredict exposure of occupants in the vicinity of the release (Nicas, 1996 and Behar, 1996). CFD offers a solution approach free of the well-mixed assumption. A recent literature review (Emmerich, 1997) discusses the use of CFD to model pollutant dispersion in large indoor spaces. The CFD predictions can be used (in conjunction with experimental results) to determine optimal sensor location, develop rapid response strategies, and quantify pollutant dispersion under various release scenarios. We envisage three phases in our multiyear effort applying CFD to indoor pollutant dispersion. (1) selection and application of a suitable commercial CFD code and its experimental verification in the laboratory, (2) enhancement of CFD model capabilities as necessary and experimental verification of CFD predictions in the field, and (3) application of the enhanced CFD model to provide guidance for response strategies.

Early on we decided that we would use a commercial software package rather then develop one in house. We made this decision based on a belief that the technical quality of CFD software has reached an acceptably high level. In addition commercial software packages have user friendly front ends that make them easier to learn to use than research codes. Also the majority of commercial codes are adaptable through user coded subroutines. Finally, commercial software companies can devote more effort toward code development leaving us people power resources to obtain results for the different configurations.

Here we discuss the prominent features of the problem and identify the capabilities needed in a CFD package. We also discuss how several commercial CFD packages fared in terms of these criteria.

Problem Definition

A release in a public space will expose large numbers of people to the pollutant. We assume that the pollutant (heavy vapor, gas, or aerosol cloud) release occurs over a short period (on the order of seconds). It is important to predict the detailed early behavior of the transport and dispersion of the release because of the implied risk to the health and safety of the occupants. We defined an example space and obtained preliminary predictions of airflow to evaluate several commercial CFD packages.

Our example space, an auditorium, is roughly 20 m long, 40 m wide and 10 m high. A computational mesh for an empty room with a resolution of 0.25 m (resolving a few breathing volumes) in the core region and further refinement of the boundary layers in near-wall regions requires about a million cells. More cells are needed to model flow around occupants, furniture, and equipment. The auditorium is mechanically ventilated with low velocity (between 0.2 and 2 m/s) conditioned air supplied from ceiling and near ceiling registers. Heat plumes caused by people and equipment also affect the room airflow. The square root of the Grashof number is an order of magnitude greater than the Reynolds number in this problem, indicating a mixed convection regime. The possibility of unsteady laminar, transitional, and fully turbulent flow in various parts of the room further complicates the simulation.

We are primarily interested in the transient pollutant transport and dispersion. We suspect that large turbulent eddies will significantly affect pollutant transport. The room has regions of anisotropic turbulence due to jets and thermal plumes. This leads us to explore the applicability of a large eddy simulation (LES) model. LES simulation will require an order of magnitude higher resolution than the present 0.25 m. The present resolution is adequate for a k-epsilon eddy viscosity turbulence model. Such models may offer an approximate guide to the pollutant plume development and dispersion, although k-epsilon models have been shown to be inadequate to accurately model all aspects of the flow field in a room [7-9].

Based on the air velocities in the auditorium, the pollutant will remain in a computational cell from 0.1 to 1.0 seconds, which is the order of the temporal resolution needed. We are interested in making predictions during the first 2 air changes after release. Assuming the room has 2 to 4 air changes per hour (ACH), the simulation will cover between 0.5 and 1 hour. Thus a typical simulation will require about 30,000 time steps.

CFD Requirements

We identified seven desirable criteria for a CFD code to model pollutant dispersion and deposition in a large single room. Other aspects of the codes were evaluated but received lower weighting in our decision process. We need a code that:

- Handles large problems efficiently. Due to the large problem size availability of super computer resources, and need for fast turn around, we gave preference to codes that can run in a massively parallel mode.
- Allows for local grid refinement. Error estimators and other tools to evaluate the quality of the mesh are also considered advantageous.

- Utilizes second order discretization schemes. This is required for LES analysis which we plan to do in subsequent years. Control of numerical diffusion is also desirable.
- Implements different turbulence models. Codes with an LES model or with a capability to incorporate one are favored.
- Simulates mixed convection typical of large indoor spaces. Ideally the code has a library of predefined HVAC components. A track record of applications in the buildings field is desirable.
- Simulates transport and dispersion of aerosol clouds, heavy vapors and gases using appropriate mass transport models. Ability to model settling, coagulation and deposition of aerosol particles is desirable, as is the ability to accommodate a variety of wall boundary conditions.
- Allows for user modification. As a research organization, we need some means of modifying key aspects of the analysis such as turbulence and deposition modeling. This can be accomplished either by access to the source code or through application of user subroutines.

Commercial Codes

There are many commercial CFD codes available, and most are listed in the popular engineering literature [e.g., 10]. Based on an internal review and discussions with colleagues, we identified seven potentially suitable commercial CFD codes. Subsequent discussions with vendors led to a short list of four finite volume commercial CFD codes. In principle, finite element codes are just as capable of addressing our problem. Comparison of finite element and finite volume codes can be found in the literature [e.g., 11]. Preference for finite volume codes probably reflects our research bias.

This paper is not an endorsement of any commercial code. Therefore, we refer to the four codes and their vendors as A, B, C, and D. We saw demonstrations of the codes and determined how their features matched our criteria. All four codes can model multispecies vapor transport. All four codes have the standard k-epsilon model; all but A also offer other turbulence models. All four codes have ease of use that is rarely found in the research codes to which we are accustomed. They all have automated or computer assisted grid generation, user-friendly graphical interfaces, beautiful post-processing capabilities and graphics outputs. All codes, except A, can import tetrahedral and hybrid meshes created by third party software. All codes, except A, allow user defined subroutines. All codes, except A, can run in a parallel mode. We then supplied each vendor with specifications of our example space to simulate its airflow. We summarize of capabilities of the codes and discuss their performance in modeling the example auditorium.

Code A is an industry specific code. It was developed to model airflow in rooms and is presently used primarily for simulating industrial clean rooms. The code is geared towards HVAC professionals who are more interested in clean room design than in CFD research. It uses a fully structured Cartesian grid (the only one among the four to do so). In a fully structured grid, closely spaced grid lines needed for local refinement must extend throughout the entire domain. This makes for inefficient distribution of elements. Code A has been used to model flow in large rooms and the vendor has good in-house buildings expertise. Code A provides built-in boundary conditions for common HVAC components. Accurate modeling of these boundary conditions is

obviously desirable and was identified in a previous review as a key element for accurate modeling of room airflow [6]. Aerosol transport can not be modeled at this time.

Code B is a general-purpose CFD code initially developed to model turbomachinery. The code uses a hexahedral multiblock mesh. A wide variety of turbulence models are offered including several two-equation models, the algebraic stress model and the Reynolds stress model. There are no near term plans to develop LES capabilities. A consulting group has been modeling large indoor spaces for many years using Code B. The grid structure of Code B, suitable for turbomachinery, was considered cumbersome by this consulting group for buildings applications. Code B can model aerosol particles including gravitational settling.

Code C was developed as a general-purpose code. It is currently the most used CFD code worldwide. Its mesh generator automatically creates a tetrahedral mesh and allows for semi-automated hexahedral meshing. Hybrid grids are also possible. Code C has the same full range of turbulence models available in Code B and also has LES capabilities. We were shown an example of a large auditorium modeled with Code C. The vendor has four technicians on staff to help users with HVAC applications. The code can model aerosol particles including inertial slip and gravitational settling. There is a range of options for wall boundary conditions such as reflection and escape. Deposition can also be modeled including the effects of surface reaction, and wall concentration. This is a significant strength of the code.

Code D is a general-purpose code used extensively in the automotive industry. The code has been optimized and widely used to simulate large and complex problems, and is the only code among the four that runs in a vectorized massively parallel mode. Code D has a semi-automated hexahedral mesh generator. There are quality checks for the mesh and an error estimator to help determine where local grid refinement is necessary. Code D does not contain an Algebraic or Reynolds stress turbulence model but does have a variety of two equation models as well as LES. There is a second order spatial discretization scheme offered in Code D that controls numerical diffusion. A major architectural firm has been using Code D for many years to satisfactorily model airflow in large spaces. The aerosol model includes gravitational settling. Code D has an easy-to-use framework for implementing the user defined subroutines.

Example Auditorium

Each of the venders was given the specifications of the auditorium to model. The room was modeled assuming symmetrical airflow about the vertical center plane of the room. There are two seating areas in the model, one on the ground and one in a small rear balcony. Heat sources representing people are arranged in rows. Exhaust vents are located on the floor near the heat sources. Mechanical ventilation provides 13…C supply air at the rate of 8 ACH. We specified the mesh resolution at approximately 500,000 elements. The vendors modeled only the airflow using a standard k-epsilon model. Although we tried to fully specify the problem, each vendor did something a little different making direct comparison of the results impossible. Two vendors directly solved the steady-state equations, one vendor used false transients to obtain a steady-state solution, while one vendor solved the time dependent equations with time-marching to try to reach the steady state solution. We examined the simulation predictions for reasonableness, based on our engineering judgment.

Results Of The Selection Process

Vendor A produced the first results. They modeled the entire room, rather than impose a symmetry boundary condition as suggested. They provided us with an animation of the results and an informative report including suggestions on how to better represent the inlet conditions. Their results seemed reasonable. Code A certainly meets the criterion of having a track record modeling airflows in buildings. However, it did not meet any of the other decision criteria and so we eliminated Code A.

The remaining three codes appeared to be comparably strong candidates. Each met most of the criteria. Ultimately our experience working with each of the vendors was as important to the decision process as the technical capabilities of the codes.

Vendor B provided a quick turn around and sent us converged steady state results. An examination of the results suggested a problem in the boundary conditions. Nothing was exiting through the ground floor exhaust grills, modeled as pressure boundary conditions. Simulations by all other vendors showed exhaust through these grills, as expected. There were also counter-intuitive distortions in the streamlines in the core region. At our request the vendor reviewed the results. They reported back that they had every confidence in their results. Our faith in Code B was inversely proportional to the vendor s confidence.

Vendor C made a faulty first attempt based on a misunderstanding of the boundary conditions. They subsequently presented us with a converged steady state solution. The vendor also ran the problem on a coarser mesh to demonstrate the grid independence of the solution. Vendor C solved the problem in two stages. In the first stage (300 iterations), they obtained a converged solution to the isothermal problem assuming only mechanical ventilation. The sum of the residuals was then 10^{-3}. In the second stage (150 iterations), they turned on the heat sources until the sum of the residuals leveled off at
10^{-2}. The flow solution seemed to make physical sense although the solution approach struck us as unorthodox.

Vendor D reported trouble getting the problem to converge to a steady state solution. The vendor finally asserted that the flow in the room was steadily oscillating and that no time invariant solution existed. They sent us an animation showing an oscillation between two vortex structures, one in the balcony and one on the ground floor. The animation showed the heat building up on the floor and periodically injecting hot air into the room. These results also seemed reasonable. Vendor D performed a numerical experiment, halving the time step, to show that the period of the oscillation was independent of the time step. This led us to believe that the oscillation reflected the nature of the flow rather than a numerical artifact.

Discussion

It was a close choice, but we finally chose Code D. The decision was based on apparent reasonableness of predicted air flow for the example auditorium, optimization of the code for massively parallel vectorized computing, willingness and ability of the vendor to work closely with our research staff, and features of the code allowing ease of user defined subroutines. We

plan to use this last feature of Code D to implement our own detailed pollutant transport models, and overcome any deficits in the prepackaged pollutant models.

In addition to exploring appropriate turbulence models and selecting the appropriate software we also had to make some decisions about computer hardware. Early on we decided that much of our production runs would be done on one of two supercomputer clusters: National Energy Research Supercomputing Center (NERSC) at LBNL and Facility for Advanced Scalable Computing Technology (FAST) at LLNL. We also needed a workstation class machine that would primarily be used for pre- and post- processing and for initial convergence tests. The existing older workstations in the department did not have adequate memory and could not be upgraded. We purchased a SGI Origin 2000 computer with 2 250 MHz processors and 2 GB of RAM. The plan was to start with a sparsely populated computer and over the years purchase additional processors. The system is capable of handling up to 64 processors with the individual chassis stacked in a rack.

Unfortunately although SGI uses IEEE binary, neither the Crays at NERSC nor the DECs at FAST; do so conversions between these multiple platforms presented an added complication to the project. As it turned out about 80% of the work completed this year was done on Lorax. For this next year we have been awarded 20,000 hours on the NERSC PVP machines and 15,000 hours on the NERSC MPP machine. We plan to focus our effort on these machines and hold the FAST machines as an emergency backup.

Part 2: Application of the Commercial Code to Selected Three Problems

Initial Three Geometries

1). THE FRANCO-AMERICAN AUDITORIUM

Once the preliminary decisions were made we began performing calculations on three configurations. The first configuration was a modification of the auditorium used as the test case in the software selection process. This revised model was adapted to more closely represent a possible auditorium by conforming occupancy rates, chair spacing and aisles to the Uniform Building Code. This generic auditorium has no experimental counterpart. The simulation work done with configuration is being done in cooperation with two research groups in France (Ecole Nationale des Travaux Publics de l Etat, ENTPE, Lyons and Laboratoir d Etude des Ph nom nes de Transfert Appliqu s au B timent, LEPTAB, La Rochelle). Each of these research groups has there own method of using multi-zonal methods on a single large indoor space. The group from ENTPE uses a conventional multi-zonal model (Voeltzel et al. 2000, Litvak et al. 2000 and Voeltzel, A. 1999). The group from LEPTAB uses a multi-zonal model that includes physical flow features such and jets and plumes (Wurtz et al. 1999 and Inard et al. 1996). The volume flow rates, angle of inlet flow, amount of heat released into the room and the definition of the pressure at the outlets were modified in an attempt to harmonize how the auditorium was modeled by each of the groups. One of the reasons for choosing this as the first computational model is because the experimental facilities at LBNL were not finished. Indeed the water tank experiment had not even been suggested. As the experimental facilities came on line our efforts shifted to modeling them and work on the auditorium was postponed. At this writing we are in

the process of obtaining the velocity field in the empty room. This is the solution with no heat transfer or pure forced convection. In the course of the next year we plane to continue to work closely with our French colleagues to analyze this room in the hopes of determining the usefulness of using a multi-zonal model approach for large indoor spaces. We will add the effect of heating to the occupants of the space and we will explore four release scenarios. Three that are burst releases on the floor of the auditorium and one that is a burst release in the HVAC system. The detail drawings of the auditorium, called the Franco-American auditorium are provided in Figures 1 — 6.

- Boundary Conditions

1) Velocity:
   a) Walls: no slip condition (u = v = w = 0)
   b) Inlets (assuming 80% recirculation = 20% fresh air):
      i) Central Diffuser (assuming a flow rate of 5 m^3/sec, an overall area of 11.5 m x 22 m, and open area for this perforated plate of 25%.) w = -0.08 m/sec.
      ii) Balcony Diffuser (assuming a flow rate of 3.4 m^3/sec, and an overall are of 0.15 m x 34 m) v = 0.67 m/sec.
   c) Outlets: (Pressure Specified)
      i) One the floor, P = 100,000 Pa.
      ii) At the first riser in the balcony, P = 99,949 Pa.
      iii) At the second riser in the balcony, P = 99,942 Pa.
      iv) At the third riser in the balcony, P = 99,935 Pa.
2) Temperature
   a) Walls: adiabatic
   b) Volumetric heat sources representing people 0.36 kW/row
   c) Inlet Air Temperature 12.8 ¡C
3) Turbulence (k,_):
   a) Inlet:
      i) Turbulent intensity = 0.1
      ii) Length scales: for balcony = 0.015 m for floor = 1.15 m.
   b) Outlet:
      i) Turbulent intensity = 0.1
      ii) Length Scales: for balcony = 0.02 m for floor = 0.03 m
4) Sources (equivalent to 1.0 m^3 of neutrally buoyant pulse release with initial concentration normalized to 1.0). Release coordinates, below, in meters. See Fig. 1 for coordinate axes and origin definition.
   a) Release 1 — Center of release at (25.75, 18.50, 0.50)
   b) Release 2 — Center of release at (25.75, 10.00, 0.50)
   c) Release 3 — Center of release at (25.75, 0.50, 6.30)
   d) Release 4 — This release will simulate a simultaneous release from both the ducts. We assume that the pollutant has entered the air handling system and the cubic meter of pollutant enters the room through both the central diffuser and the balcony inlet. The source is defined to be initially in the shape of a thing slab of gaseous material with one face the same dimensions as the inlet (x and z for the balcony, x and y for the central diffuser). For the balcony diffuser the shape of

the release (directly adjacent to the balcony inlet is 0.15 x 0.075 x 34. For the central diffuser the shape of the release (directly adjacent to the central diffuser) is 0.0025 x 11.5 x 22.

For our computational efforts we are using a high Reynolds number k-epsilon model. We are assuming constant properties and are using the Boussinesq approximation to account for the coupling between the energy equation and the momentum, k and epsilon equations. The Navier-Stokes equations take the following dimensional form (Adapco 1999, Townsend 1976):

$$\frac{\partial U_j}{\partial x_j} = 0$$

$$U_j \frac{\partial U_i}{\partial x_j} = -\frac{1}{\rho}\frac{\partial p}{\partial x_i} + \frac{\partial}{\partial x_j}\left(\nu \frac{\partial U_i}{\partial x_j}\right) + \frac{2}{3}\frac{\partial k}{\partial x_i} + \beta g_i (T - T_{bulk})$$

$$U_j \frac{\partial k}{\partial x_j} = \frac{\partial}{\partial x_j}\left(\frac{\nu_{turb}}{\sigma_k}\frac{\partial k}{\partial x_j}\right) + \nu_{turb}\left(\frac{\partial U_i}{\partial x_j} + \frac{\partial U_j}{\partial x_i}\right)\frac{\partial U_i}{\partial x_j} - \beta g_i \frac{\nu_{turb}}{\sigma_T}\frac{\partial T}{\partial x_i} - \varepsilon$$

$$U_j \frac{\partial \varepsilon}{\partial x_j} = \frac{\partial}{\partial x_j}\left(\frac{\nu_{turb}}{\sigma_\varepsilon}\frac{\partial \varepsilon}{\partial x_j}\right) + \frac{\varepsilon}{k}\left[C_{\varepsilon 1}\left(\frac{\partial U_i}{\partial x_j} + \frac{\partial U_j}{\partial x_i}\right)\frac{\partial U_i}{\partial x_j} - C_{\varepsilon 3}\frac{\beta g_i}{\sigma_T}\frac{\partial T}{\partial x_i}\right] - C_{\varepsilon 2}\frac{\varepsilon^2}{k}$$

$$\frac{\partial M}{\partial t} + U_j \frac{\partial M}{\partial x_j} = \frac{\partial}{\partial x_j}\left(D_{molec} + \frac{\nu_{turb}}{\sigma_m}\right)\frac{\partial M}{\partial x_j}$$

$$U_j \frac{\partial T}{\partial x_j} = \frac{\partial}{\partial x_j}\left(\alpha + \frac{\nu_{turb}}{\sigma_T}\right)\frac{\partial T}{\partial x_j} + \nu\left(\frac{\partial U_i}{\partial x_j} + \frac{\partial U_j}{\partial x_i}\right)\frac{\partial U_i}{\partial x_j}$$

Where

σ_k	σ_ε	$C_{\varepsilon 1}$	$C_{\varepsilon 2}$	$C_{\varepsilon 3}$
1.0	1.22	1.44	1.92	1.44 or 0.0*

*$C_{\varepsilon 3}$=1.44 if $\partial T/\partial z < 0$ and is 0.0 otherwise.

$$\nu = \nu_{turb} + \nu_{molec}$$

and

$$\beta = 1/T_{bulk}\ .$$

The turbulent Prandtl number, σ_T, and the turbulent Schmidt number, σ_M , are assumed equal to one another (Kays and Crawford, 1993). A value of 0.9 is used near the wall and 0.5 is used in the core (Wilcox 2000).

2). The Water Tank Experiment — Water Model

The second geometry that we modeled was the water model. A top and edge view of the mesh used to model the water model is shown in Fig. 7. The mesh has a resolution of 0.3 cm in the core and of 0.06 cm within the region 0.3 cm near to the wall. This is roughly equivalent to a 10 cm mesh size in the core and a 2 cm resolution near the wall in the full scale (30 times larger) room. We assume that the volume flow rate (60 water changes per hour) enters through 5 rectangular openings. The velocity profiles are modeled as uniform across the openings and the flow rate is evenly distributed among the 5 openings. Although the velocity profile across the openings in the experimental setup is not exactly uniform, computational sensitivity studies were used to determine that the details of the profile, resulting in the shearing caused by the opening, can be ignored. The assumption that the flow was the same for each of the openings in the experimental setup was supported by the observation of the flow pattern of the minute air bubbles entering the tank with the inlet flow. This effect of this assumption was also explored with sensitivity studies. The mesh near the cut corner of the room, where the flow enters, is intentionally made to line up with the known flow direction of the jets to minimize numerical diffusion.

The pollutant source is modeled as a cube with surface area approximately equal to the spherical source used in the experiment. Steady state results for the mean velocity field were obtained using the high Reynolds number k-epsilon model. Spatially, a second order differencing scheme based on a Godunov method modified for incompressible flow (Asproulis 1994). The advantage of this scheme is that is suppresses numerical diffusion without causing instability. A second order implicit time differencing scheme is used for the solution of the mass transfer equation.

The velocity results show that the flow divides into two large vortices separated by the inlet flow. In the breathing plane there is a counter clockwise flow that spirals upwards in the SW corner. The flow from the jets enters the breathing plane near the SE corner. These flow characteristics are consistent with observation in the experiment. In the computational approach the pollutant is released into the tank once the steady state condition for the mean velocity field is reached. A comparison between the experimental data and the computation predictions for the fully developed pollutant concentration is shown in Figure 8. Figure 9 shows a scatter plot of the computational prediction and experimental data. The computational results show a greater spread of data. The computational results are lower on the low concentration end and higher on the high concentration end. There is a 4% difference in the average breathing plane concentrations between the two methods. Although there are several parameters that still need to be explored, such as turbulent mass diffusion coefficient and a method for predicting concentration fluctuations, we are pleased with the good agreement between experiment data and numerical results.

3). The Indoor Large Space ("Atrium")

The third geometry we modeled was the Atrium described in Section II. We carefully measured all of the geometric features in the experimental Atrium in order to create a computational mesh that captured details down to 5 cm. Figure 10 shows a sketch of the outline of the computational model used. Figure 11 shows the mesh used for the Atrium calculations. The inlet conditions, velocity profile shape and flow distribution are assumed to be the same as the reduced-scale water model. However the outlets are considerably different. The water model has an outlet that is a weir along the N side and a full slip boundary on the top of the tank. The Atrium has an outlet in the ceiling near the SE corner and a no slip boundary condition at the ceiling.

During this first year we obtained isothermal results for the Atrium. The first mesh resolution we used was equivalent to that of the water model. The predicted velocity field was similar to that seen in the water model in that we had a counterclockwise flow in the breathing zone and a downward flow along the SE wall. Steady state concentration results were also obtained. These are shown in Figure 12. It should be noted that the maximum concentration is in a different location than the maximum observed in the water model, Figure 8. It was assumed that the difference in the outlet boundary conditions was responsible for this effect. In order to test this hypothesis, the water model simulation was rerun with the outlet boundary conditions equivalent to the Atrium. This test showed that indeed the boundary conditions did effect the location of the maximum concentration somewhat but did not entirely account for the discrepancy. The differences in the isothermal results is an area of on going investigation.

Early experimental results showed two locations of high concentration; one in the expected location and the other along the east corner. It was determined that the east wall is on average 2K hotter than the other walls. In order to capture the effect of the thermal plume along this wall we created meshes with increased refinement at the wall in order to capture the thermal boundary layer. The initial mesh had a mesh that was refined to 5 cm at the wall. Two additional meshes were created with resolution down to 1 cm and 3 mm. Isothermal results were obtained for those meshes. Typical velocity contours plots are shown for each of these meshes in Figure 13. These results give us confidence that the 5 cm mesh resolution is acceptable for the isothermal case. The non-isothermal results are an area of future work.

CONCLUSION

Like the experimental work and the computational tomography work this has been a year of gearing up and preliminary results. We look forward to bringing the three projects mentioned in this report to completion in the next year

REFERENCES

Gadgil, A J, Finlayson, E U, Hong K H, Sextro R G. 1999. Commercial CFD Software Capabilities for Modeling a Pulse Release of Pollutant in a Large Indoor Space. *Proceeding of the 8th International Conference on Indoor Air Quality and Climate.* Edinburgh August 1999.

Chen, Q. 1997. Computational Fluid Dynamics for HVAC: Successes and Failures. *ASHRAE Transactions.* Vol. 103 (1), pp 178-187.

Baker, A J, Kelso, R M, Gordon, E B, et al. 1997. Computational Fluid Dynamics: A Two-Edged Sword. *ASHRAE Journal*. Vol. 39 (8), pp 51-58.

Nazaroff, W W, Gadgil, A J, and Weschler, C J. 1993. Critique of the Use of Deposition Velocity in Modeling Indoor Air Quality. In *Modeling Indoor Air Quality and Exposure* (ed. Nagda, N L). STP 1205, ASTM. pp 81-104.

Nicas, M. 1996. Estimating Exposure Intensity in an Imperfectly Mixed Room. *American Industrial Hygiene Association Journal*. Vol. 57, pp 542-550.

Behar, J V. 1996. Modeling Indoor Air Concentrations Near Emission Sources in Imperfectly Mixed Rooms. *Journal of the Air and Waste Management Association*. Vol. 46, pp 861-868.

Emmerich, S J. 1997. Use of Computational Fluid Dynamics to Analyze Indoor Air Quality Issues, NISTIR 5997. National Inst. of Standards and Technology. Gaithersburg, MD, USA. flame.cfr.nist.gov/bfrlpubs/build97/art016.html.

Murakami, S, Kato, S, Ooka, R. 1994. Comparison of Numerical Predictions of Horizontal Nonisothermal Jet in a Room with Three Turbulence Models — k-ε EVM, ASM and DSM. *ASHRAE Transactions*. Vol. 100 (2), pp 697-704.

Chen, Q, Chao, N-T. 1996. Prediction of Buoyant Plume and Displacement Ventilation with Different Turbulence Models. *Proceedings of the 7th International Conference on Indoor Air Quality and Climate — Indoor Air 96*, Vol. 1, pp 787-792.

Nielsen, P V. 1998. The Selection of Turbulence Models for Prediction of Room Airflow. *ASHRAE Transactions*. Vol. 104 (1B), pp 1119-1127.

Grummon, A D. 1997. Resource Guide FEA/CFD Software. *Desktop Engineering*. Vol. 4 (1), pp 46-50.

Freitas, C J. 1995. Perspective: Selected Benchmarks from Commercial CFD Codes. *J. of Fluid Engineering, Transactions of the ASME.* Vol. 117, pp 208-218.

Inard C., Bouia H., and Daliciux P., 1996. Prediction of Air Temperature Distribution in Buildings with a Zonal Model. *Energy and Buildings*. No. 24. pp 125-132.

Wurtz E., Nataf J-M., Winkelmann F., 1999. Two- and three- dimensional natural and mized convection simulation using modular zonal models in buildings. *International Journal of Heat and Mass Transfer*. No 42. PP 923-940.

Voeltzel, A., Carri , F. R., and Guarracino, G. 2000. Thermal and Ventilation Modelling of Large Highly-Glazed Spaces. Submitted to *Energy and Buildings*.

Litvak, A., Voeltzel, A., and Carri , F. R. 2000. A Zonal Approach for Predicting Spatial and Temporal Variations of Indoor Aerosol Concentrations. Submitted to *Indoor Air*.

Voeltzel, A. 1999. Mod lisation du comportement thermo a raulique des grands volumes vitr s en r gime dynamique. Ph.D. Dissertation en B timent et Techniques
Urbaines, Institut National des Sciences Appliqu es de Lyon.

Asproulis, P.N. 1994. High Resolution Numerical Predictions of Hypersonic Flows on Unstructured Meshes , Ph.D. Dissertation, Imperial College, Dept. of Aeronautics.

Kays, W.M. and Crawford, M.E. 1993. Convective Heat and Mass Transfer. 3rd Edition. Mc Graw Hill, Inc.

Wilcox, D. C. 2000. Turbulence Modeling for CFD. 2nd Edition. DCW Industries.

FIGURES

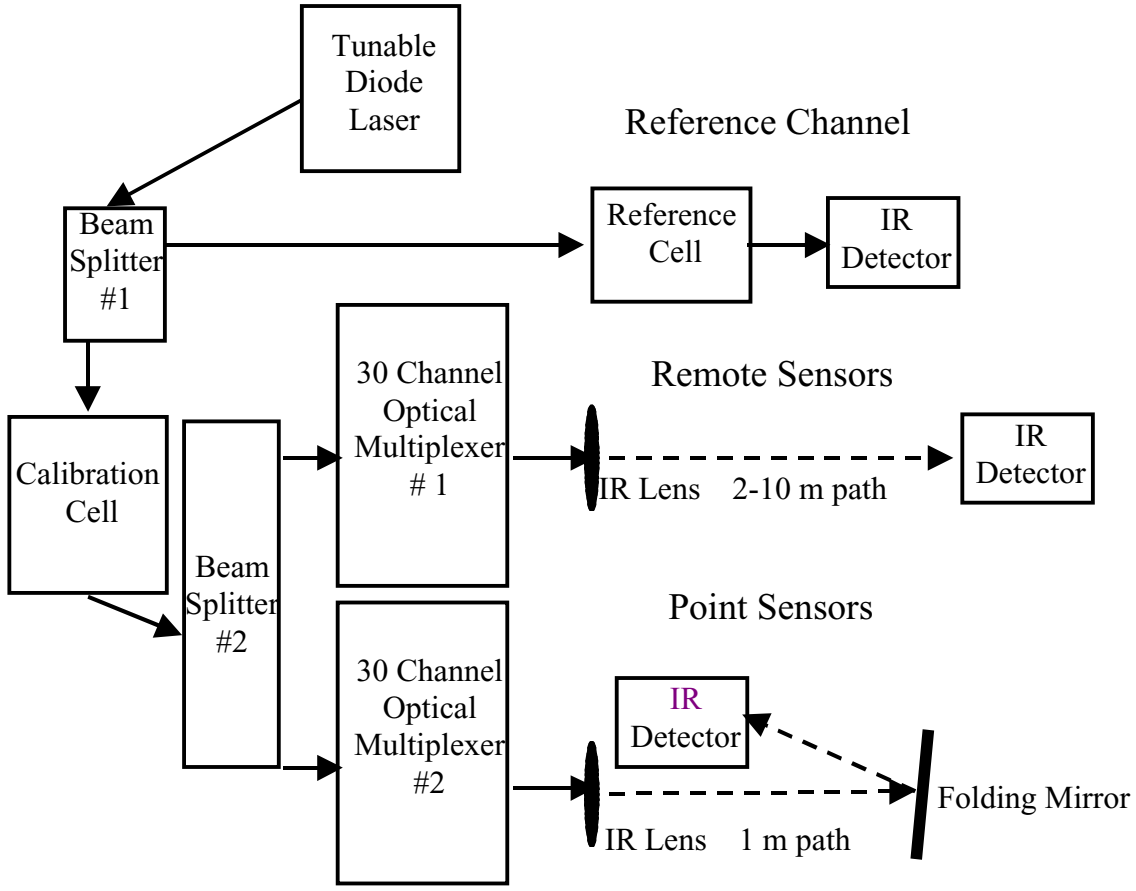

Figure 1. Optical layout of LasIR spectrometer and open-path optics. Solid lines indicate sections where beam is carried in optical fiber. Dashed lines indicate open-paths. Optics for one remote and point channel (of 30) each are shown connected to optical mulitiplexers 1 and 2 respectively. Because the calibration cell is always in the optical path of any measurement, after calibration, it is filled with ambient air.

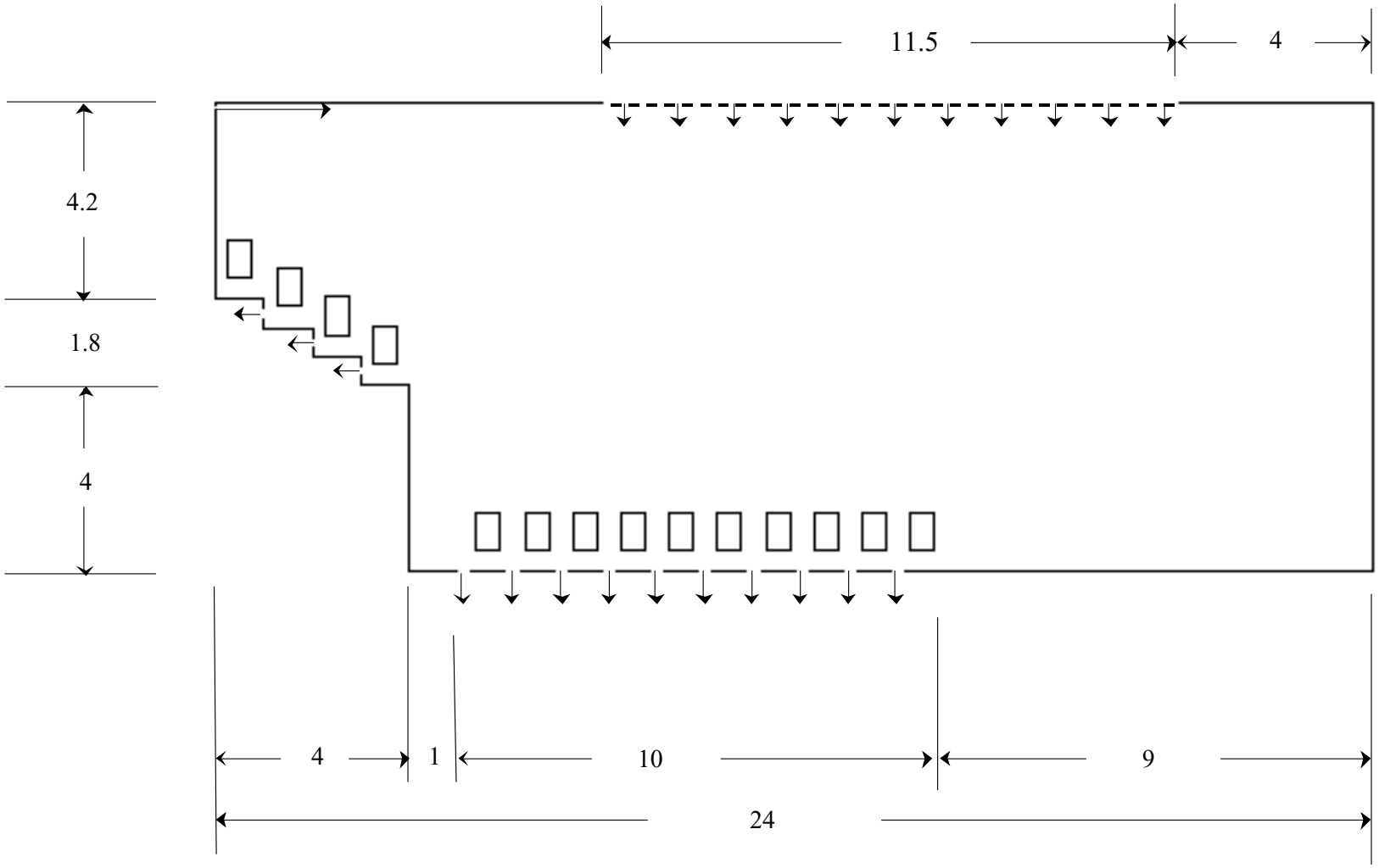

Figure 2 — Side view of Auditorium. Arrows indicate air supply and exhaust. The central diffuser is a perforated plate. Seated people show as rectangles.

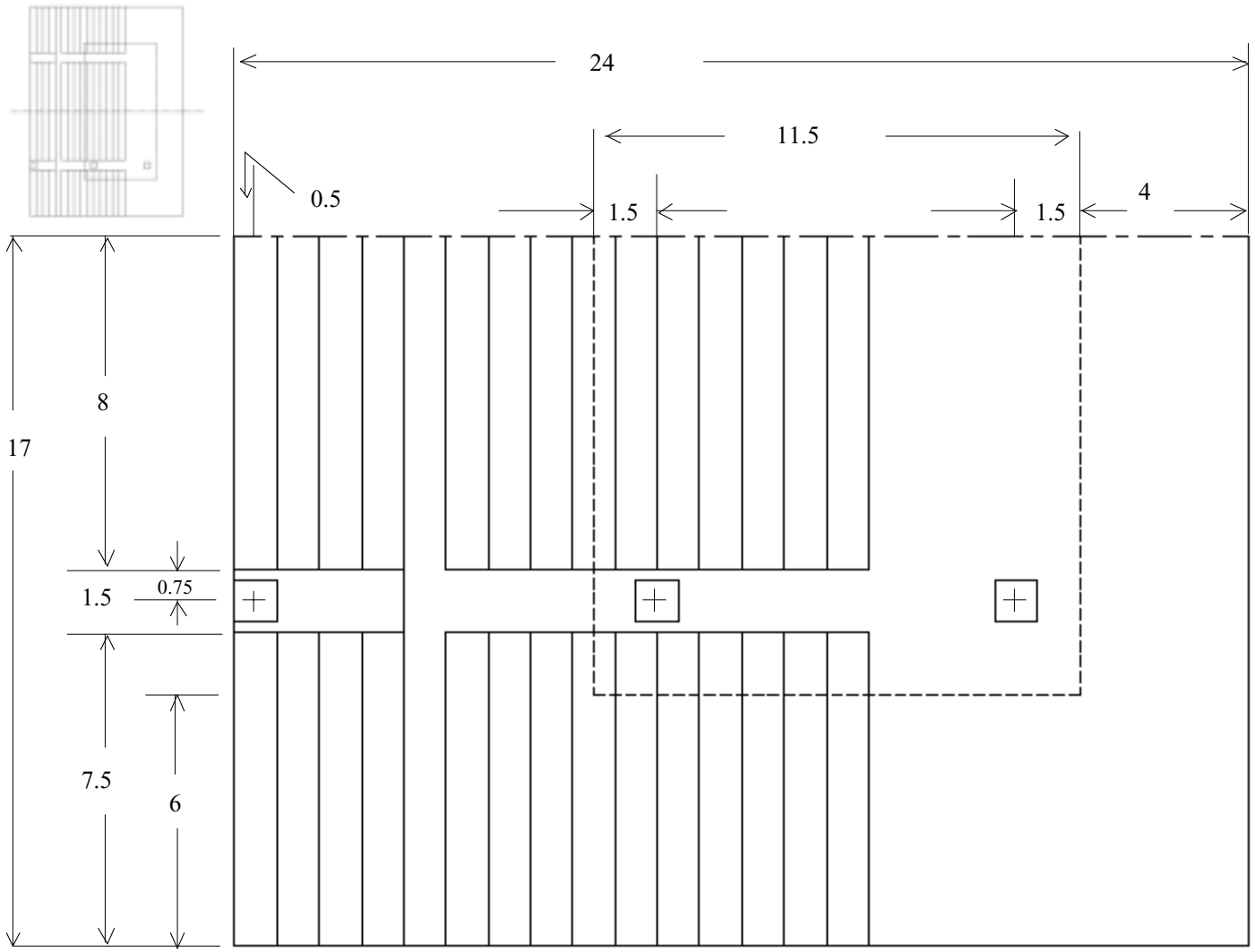

Figure 3 — Top view of generic auditorium. Releases are 1.0 m^3 and are placed in the aisle on the floor with centers located as marked with a +. An additional release scenario assumes that a 1.0 m^3 release comes from the air supply system. All dimensions are in meters.

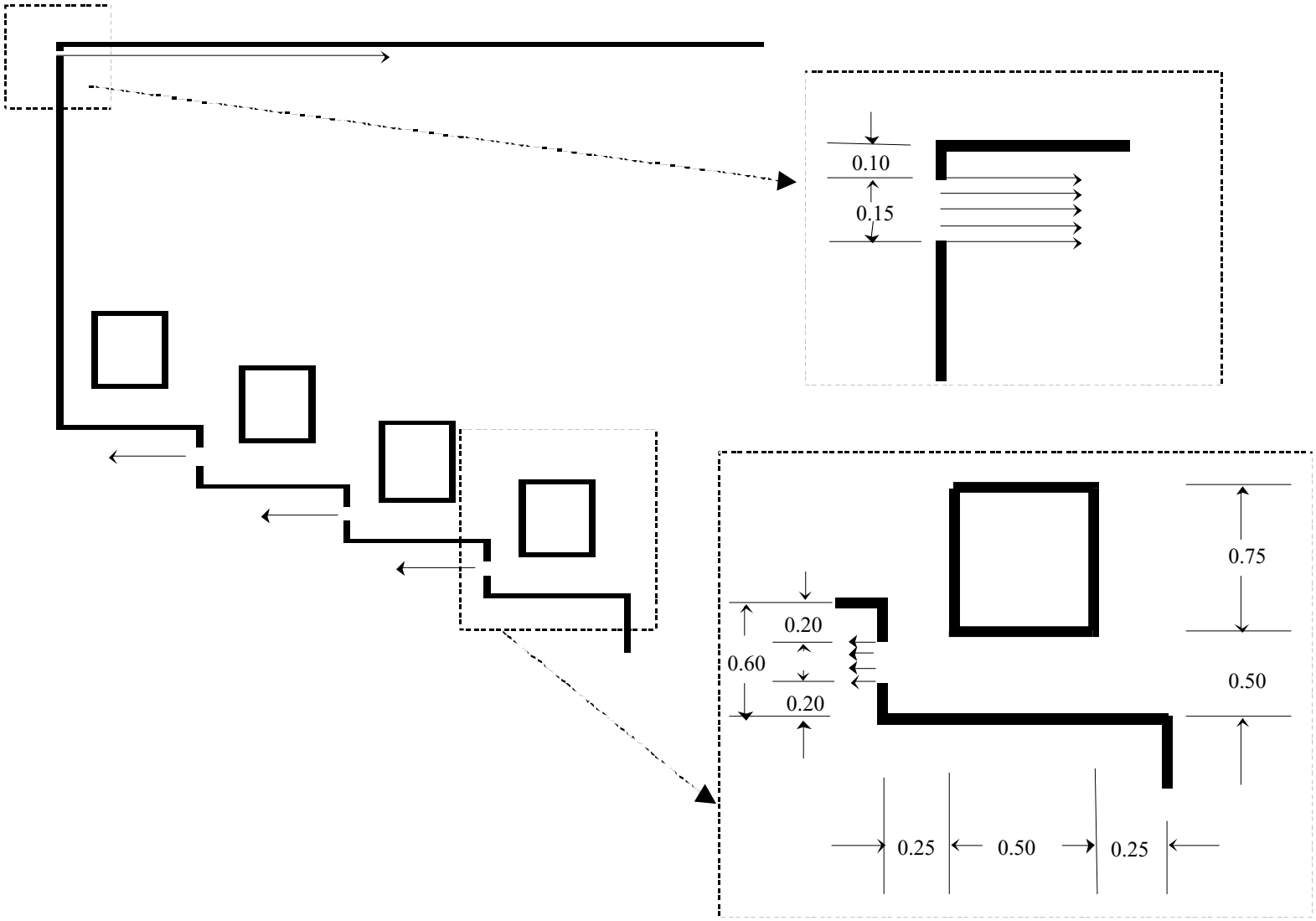

Figure 4 — Detail of geometry and boundary conditions in the balcony.

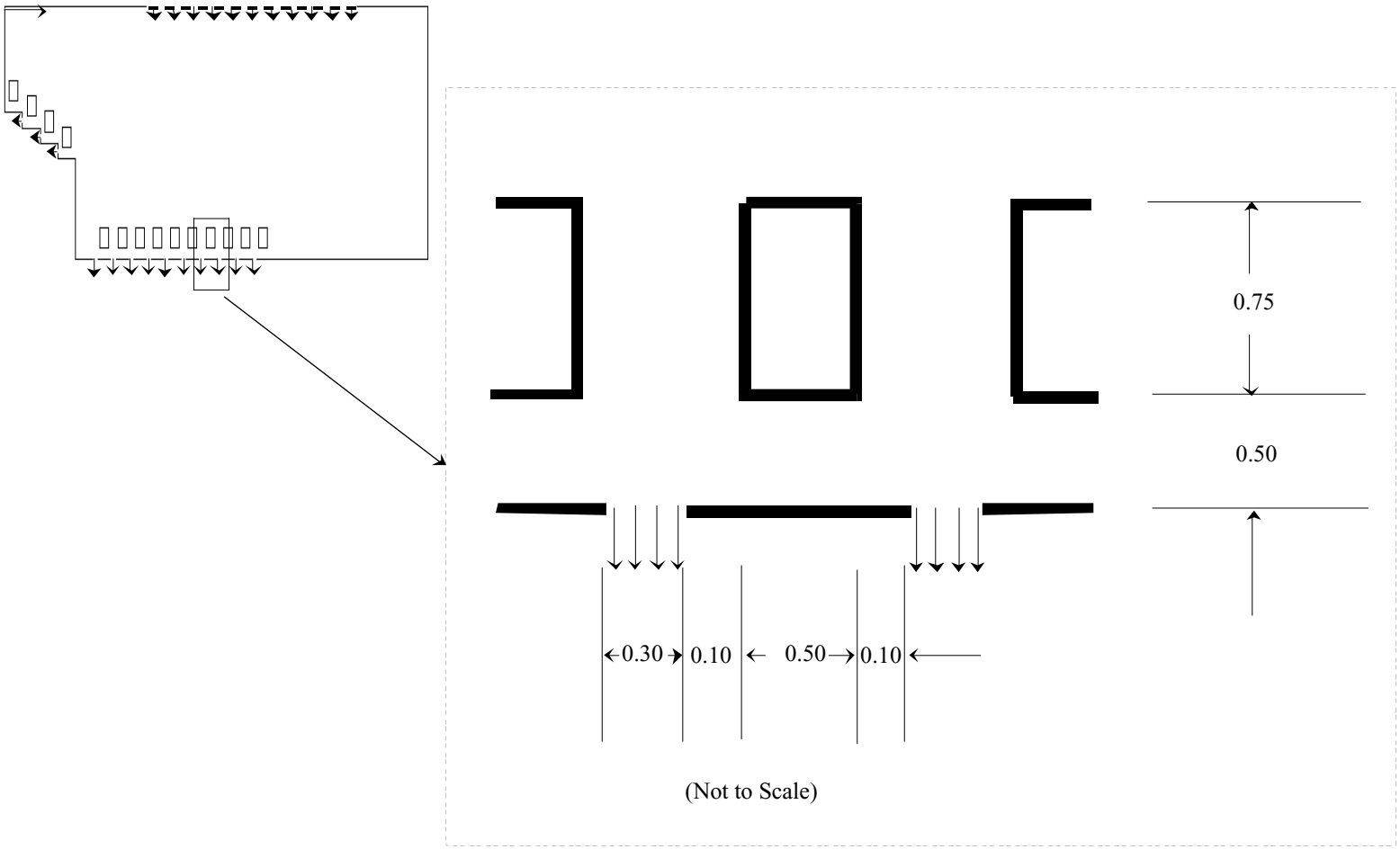

Figure 5 — Detail of geometry and boundary condition for the ground floor setting area.

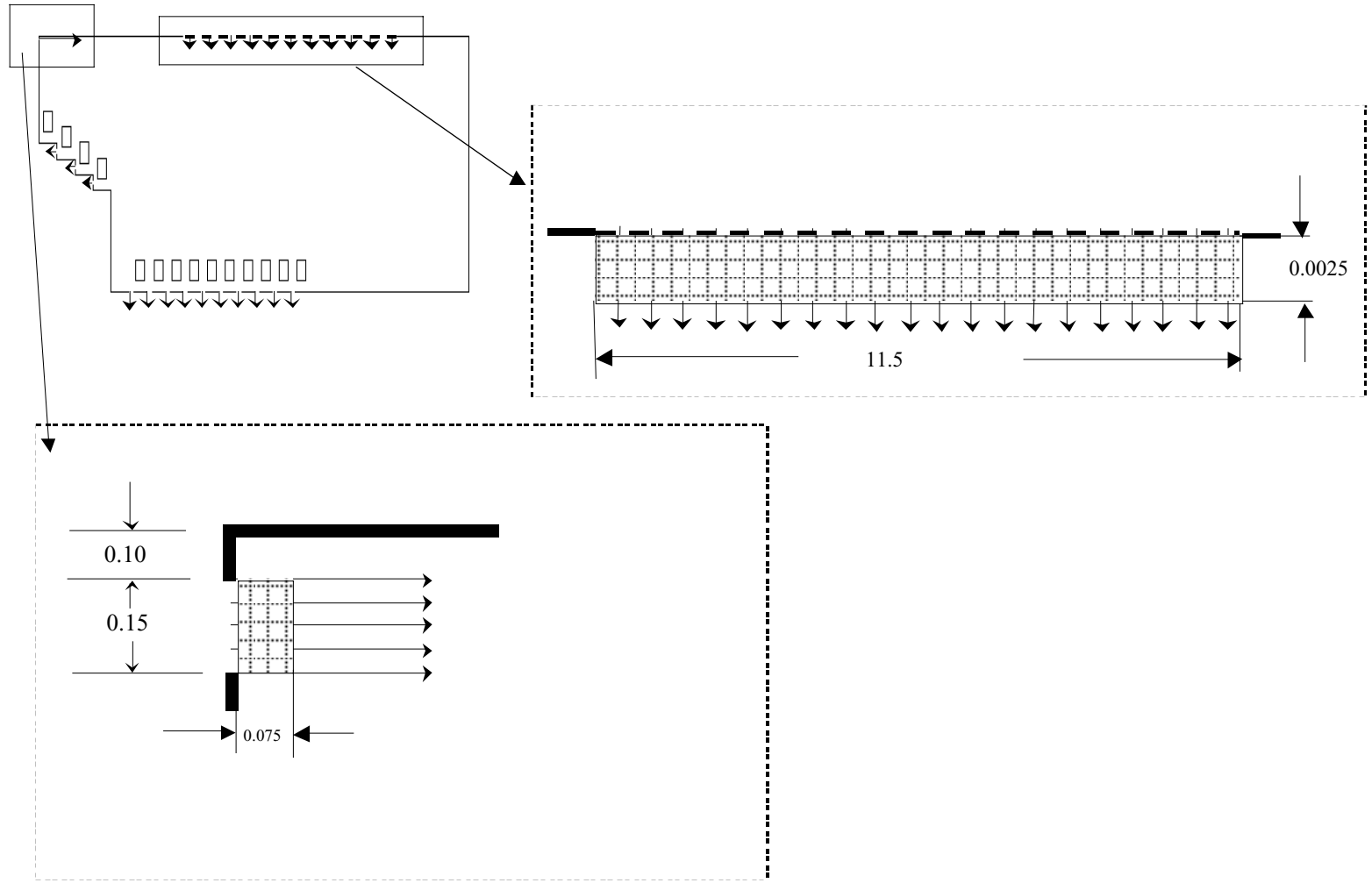

Figure 6 — Detail of boundary conditions and release 4 from the air supply system modeled as a slab of pollutant shown in the y-z- plane. Central diffuser air velocity : w = - 0.08 m / sec. Release slab applied to 22 meters in the x- direction. Balcony diffuser air velocity: v = 0.67 m/sec. Release slab applied to 34 meters in the x direction.

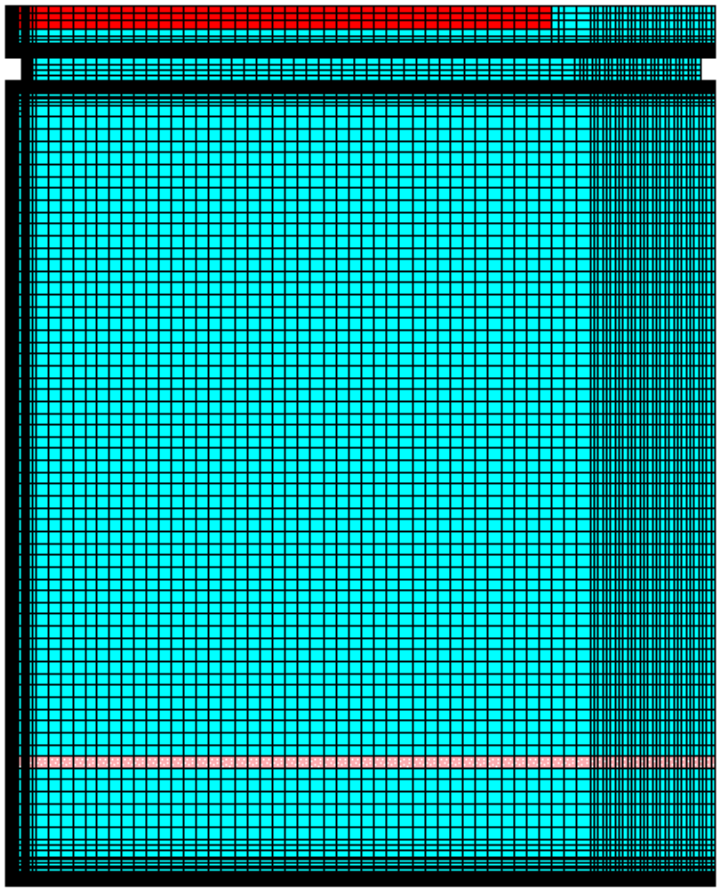

Side View

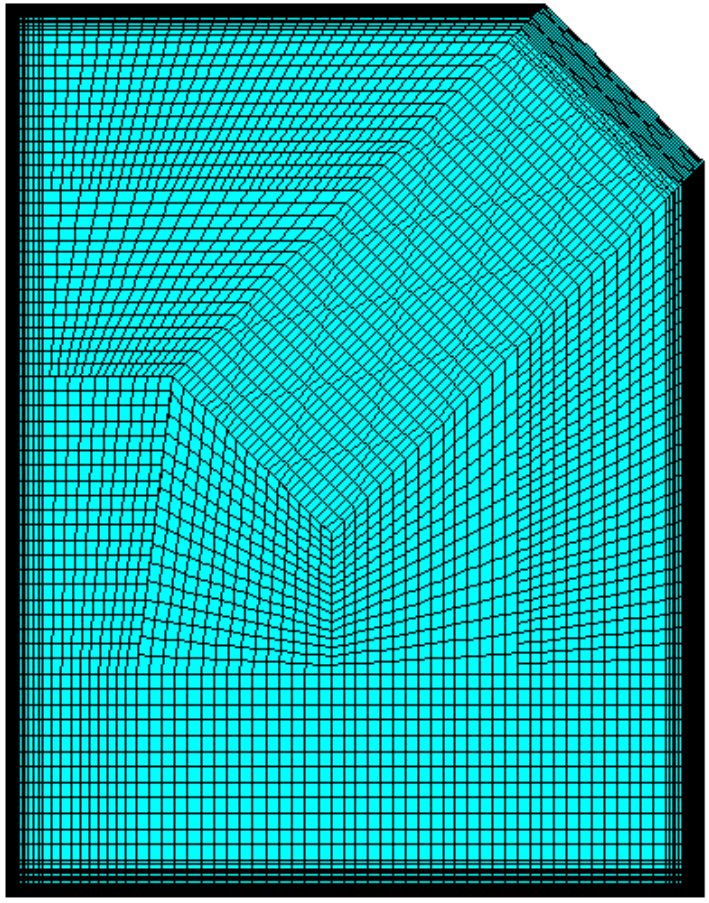

Top View

Figure 7 — Computational mesh for the Fishtank. The overall mesh has 900,000 cells. Cell size in the core is approximately 0.025 x 0.025 m. Near the wall the size perpendicular to the wall is 0.002 m. The

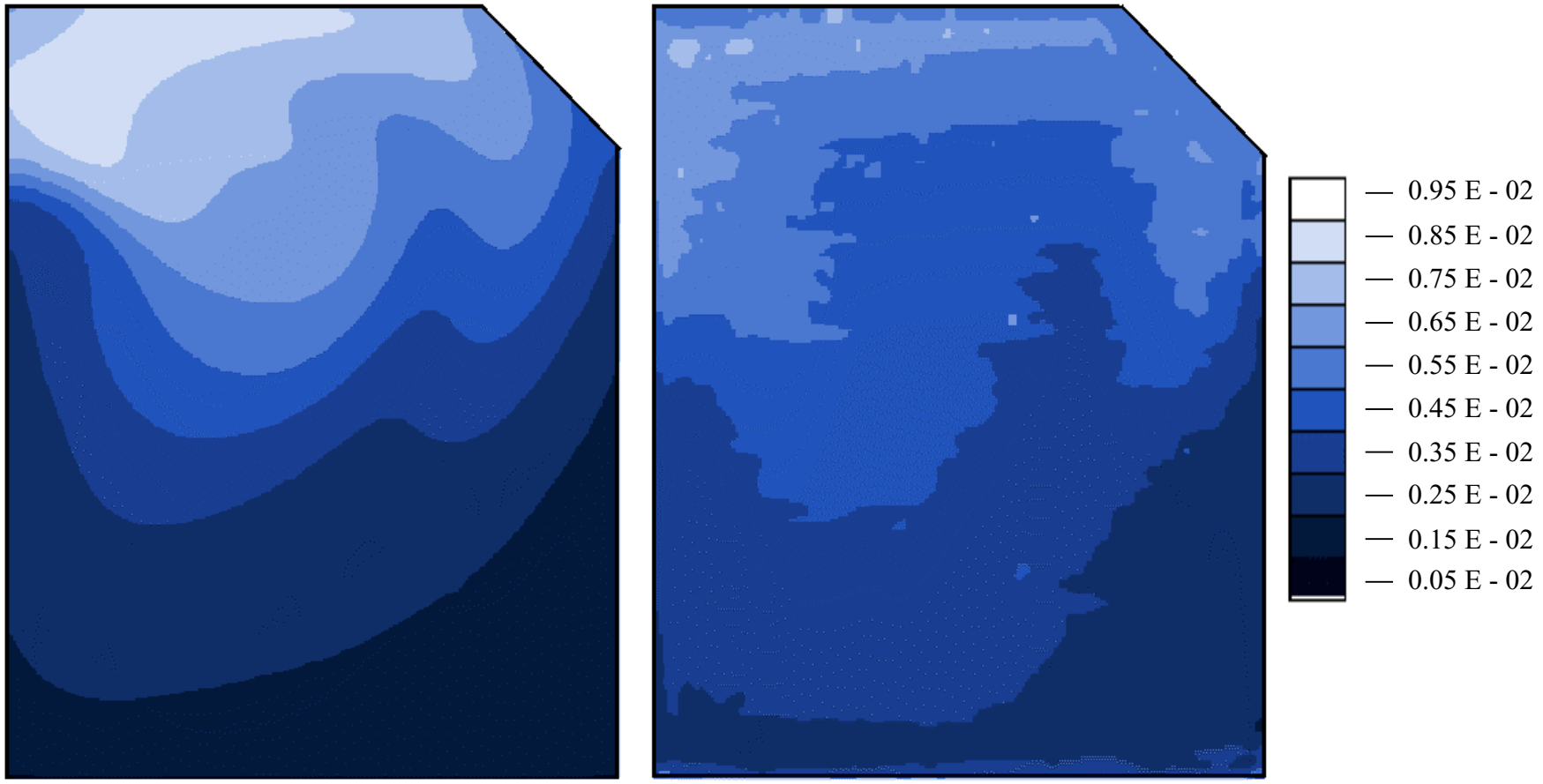

A) CFD Fully Developed Predictions
Max - 0.0090 Min - 0.0014

B) Experimental Data Averaged over 3000 Seconds
Max - 0.0080 Min - 0.0017

Figure 8 – Comparison between the experimental data and the CFD Predictions. These figures show fully developed concentration in the breathing plane. The concentration is reported as the volumetric fraction of a neutrally buoyant pollutant. Although the CFD over-predicts the high

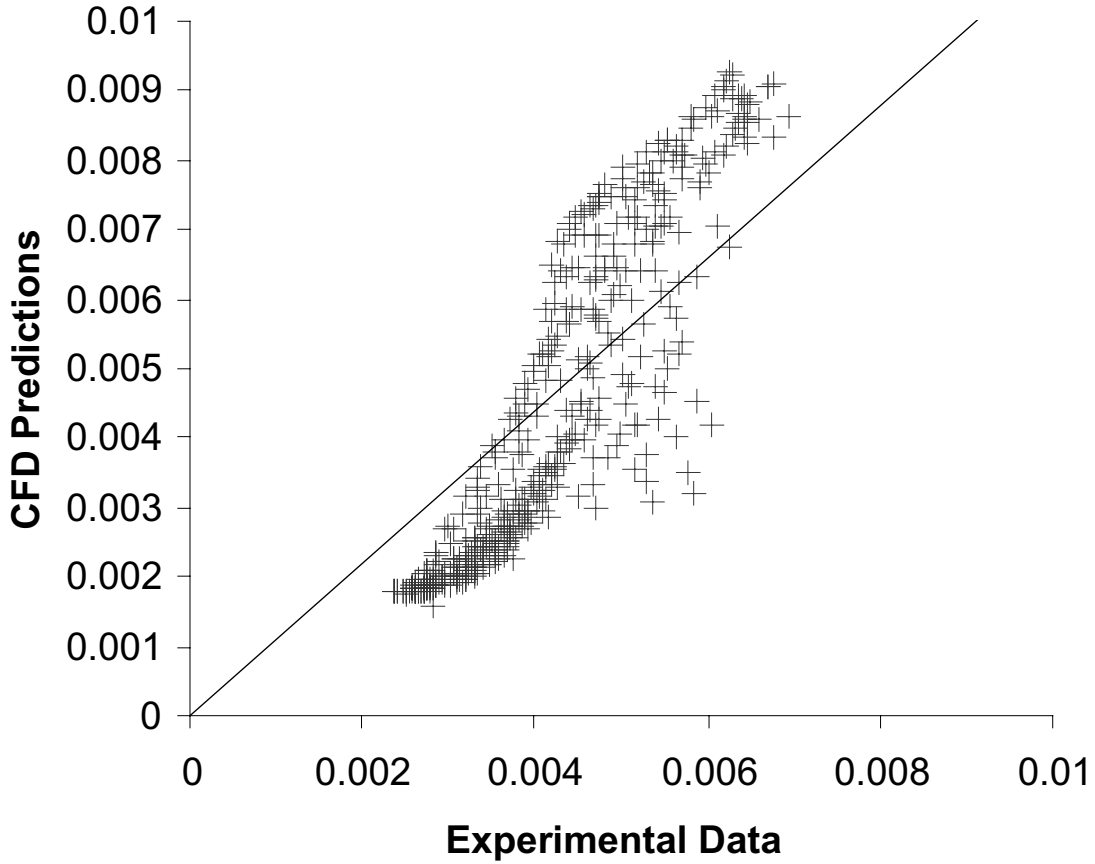

Figure 9 - Comparison of pollutant concentrations between experimental data and CFD Predictions. This scatter plot was made by overlaying a 21 X 21 uniform rectangular grid is overlaid on figure A and B in Fig. CFD 8. The spatial average of the concentration in corresponding grid pairs is plotted. The straight line fit to these data was forced to pass through the origin. The R^2 value is 0.66. The slope is 1.1.

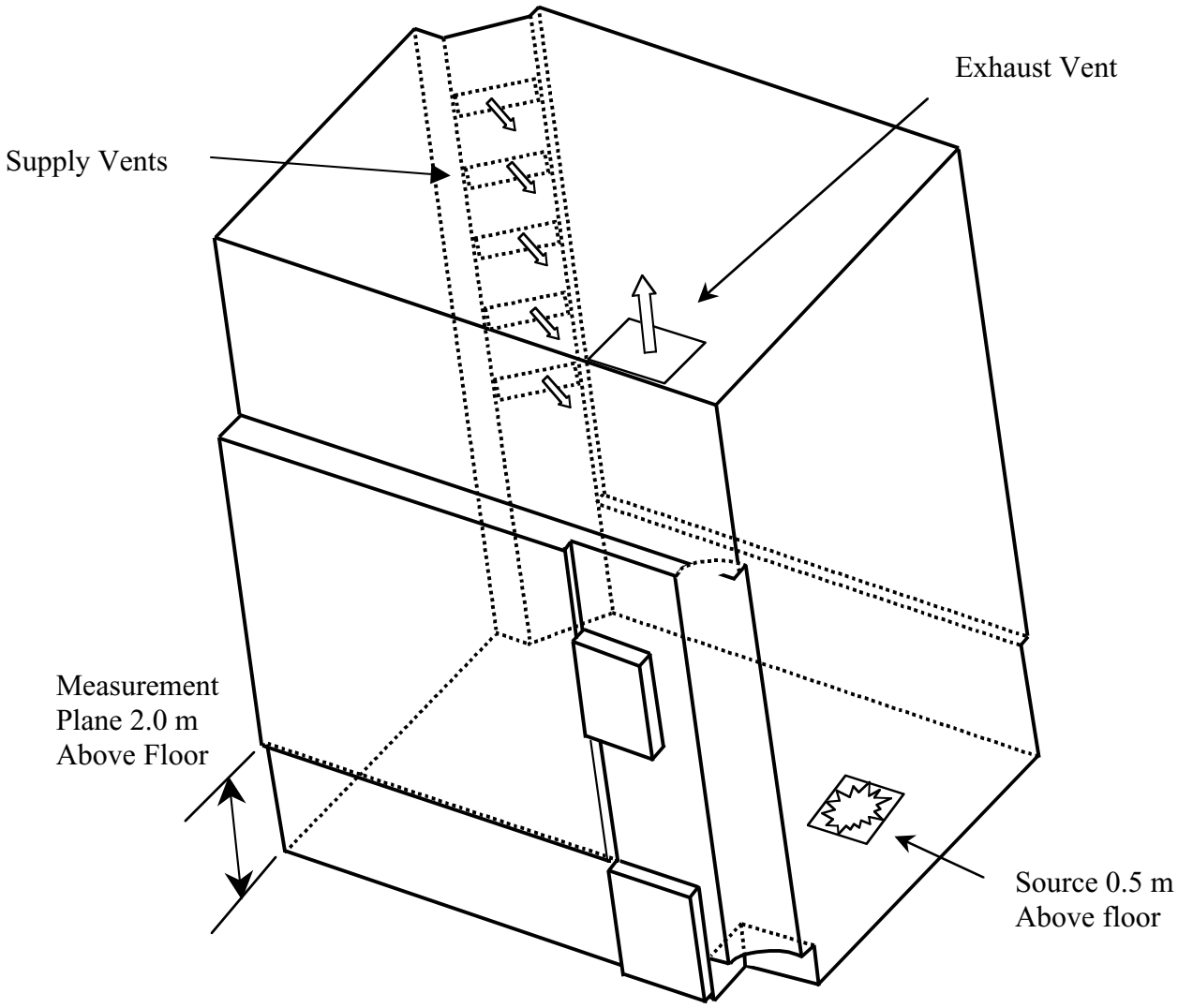

Figure 10 – Schematic of the Tinbox. The overall room size is 7.0 m x 9.0 m x 11.0 m high. The neutrally bouyant release occurs near the floor.

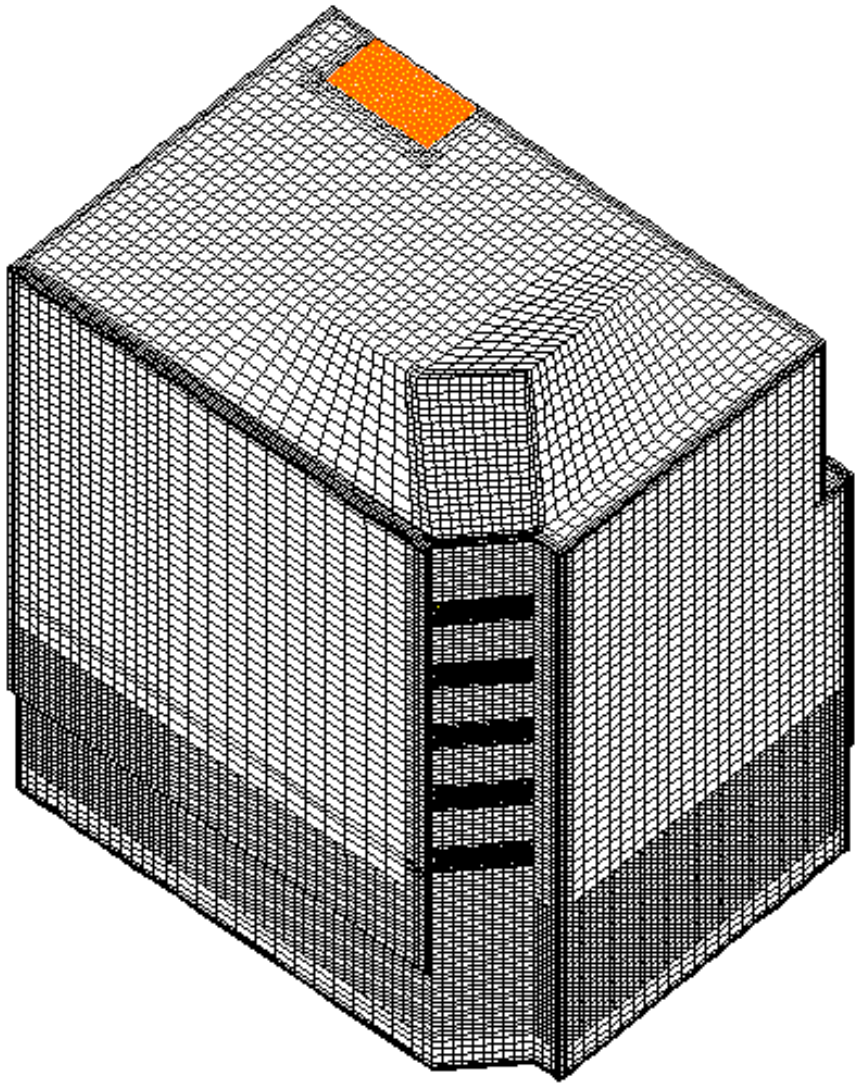

Figure 11 – This is the computational mesh used for calculations in the Tinbox. The core is meshed to a resolution of 0.20 x 0.20 m away from the breathing zone and 0.10 x 0.10 m near the breathing zone. Three wall resolutions were explored. In the direction prependicular to the wall the resolutions are 0.05, 0.01 and 0.003m.

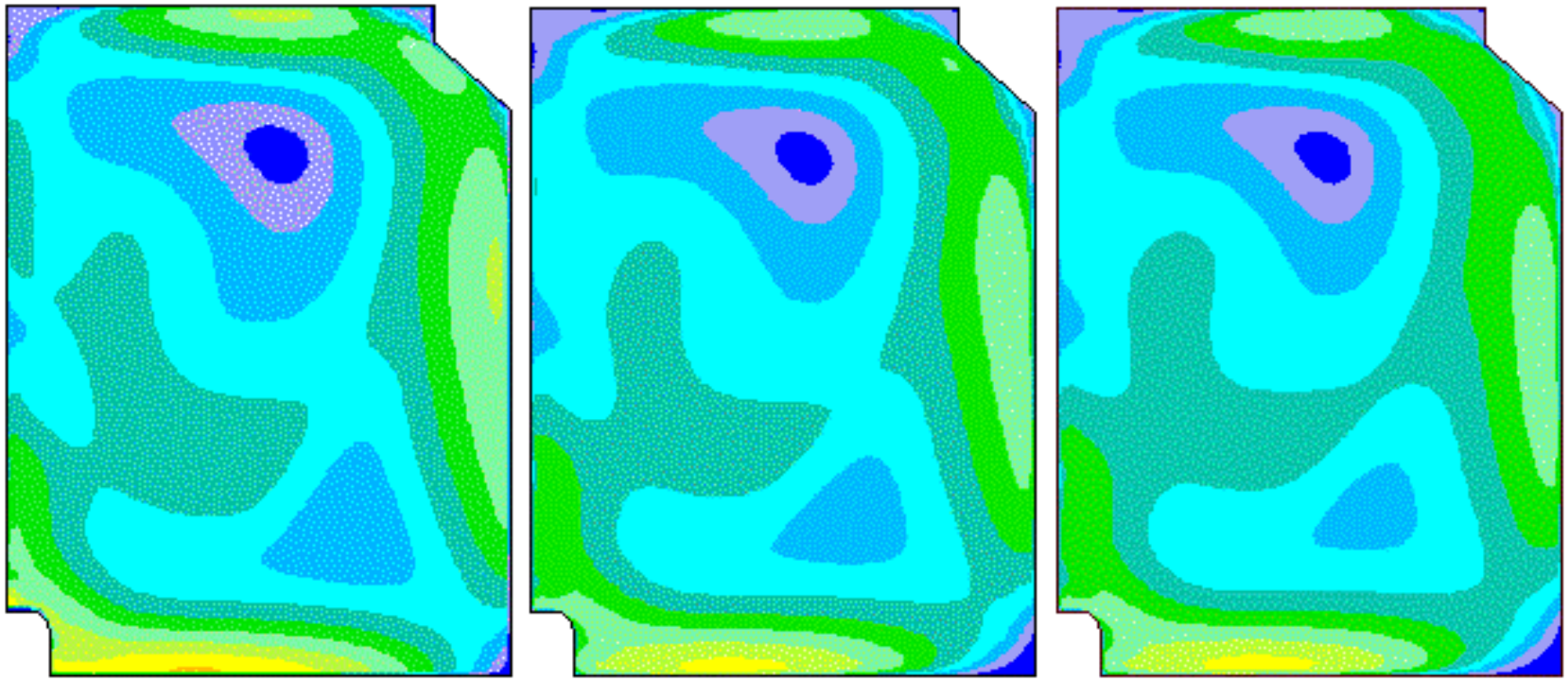

0.05 m 0.01 m 0.003 m

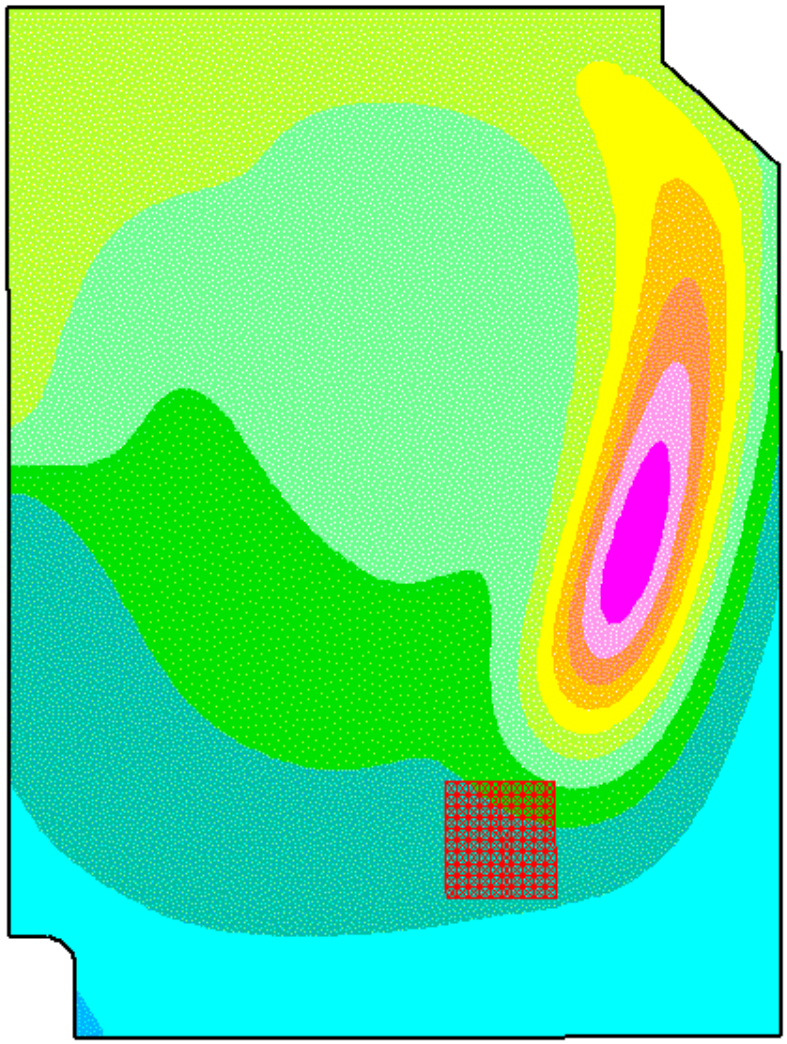

Figure 13 — Concentration profiles in the experimental plane of the isothermal flow with near wall resolution of 0.01 m.

VI. Summary and Acknowledgements

This report describes the status of our research at the beginning of calendar 2000. The thrust of this work is to develop an experimentally verified predictive capability for pollutant dispersion in large indoor spaces. This predictive capability will be based on computational fluid dynamics (CFD). We describe our experimental and computational efforts, during the year 2000, to advance this goal. The results will be relevant to the science of the indoor environment and its applications to indoor air quality protection.

We describe the establishment of a large, well-characterized indoor space, an atrium, to study the indoor dispersion of a pollutant. We describe the design, operation, installation and commissioning of a non-intrusive, rapid optical method to measure path-integrated concentrations of a surrogate pollutant (4% methane in nitrogen) released within the space. Each optical scan of the large space reports the path-integrated concentrations along all thirty optical paths. Each scan, at the breathing height (7 m by 9 m area), is completed in 7 seconds.

The path-integrated concentration data can be processed with a computed tomography algorithm, to calculate concentration as a function of location in the room. Standard algorithms from medical computed tomography yield poor results when applied to this problem. We describe our computed tomography algorithms that can produce maps of tracer gas concentration from the path-integrated concentrations measured with remote optical sensing. These maps are validated by comparison with several point-sampled tracer gas concentrations measured concurrently in the sampling plane. The development and validation of this technology is an engineering and scientific accomplishment that reflects the fruition of efforts stared in 1994 in this department with experimental and algorithmic development of computed tomography of airborne tracer gases.

To test computed tomography algorithms and to better design the large-scale facility, we first conducted experiments with an isothermal small-scale model of our large indoor space, using water as the working fluid. These experiments permitted us to study the dispersion of fluorescent dye release in the water, illuminated with a sheet of intense laser light, and quantitatively measured with a linear digital camera. We describe the theory behind the scaling of the experiment, the experimental apparatus, and show some of the results of our research. Insights generated from this research were useful in setting up the full-scale experiment described section 2.

The goal of the experiments, both in the large interior space and in the water scale model, is to experimentally validate Computational Fluid Dynamics (CFD) for indoor pollutant dispersion. CFD uses the mathematical equations governing the air flow and pollutant dispersion, including a mathematical model of turbulence generation and dissipation. Based on the solutions to these coupled partial differential equations, predictions can be obtained for indoor pollutant dispersion. For the past 20 years, we have been writing and using our own research computer codes, however the advantages of good mesh generation software and post-processing of the results available from commercial CFD packages are now generally considered to exceed the advantages of writing our own code. We describe our experience in selecting a commercial CFD

code. We then describe results obtained from applying CFD to simulate dye dispersion in the small-scale experiments, and compare these results with experimental data.

Our work on these various approaches described above has progressed further during calendar 2000 and beyond. More details of specific accomplishments can be found in the journal papers and LBNL reports published from time to time. You can find these references and others by clicking the publications button at the web site: http://eetd.lbl.gov/ied/

ACKNOWLEDGEMENTS
The authors would like to acknowledge the contributions of several others to this project. The computational work was done using the StarCD software program. Our work was accomplished with the help of the technical support staff at ADAPCO. William Fisk participated in the selection process for the gas monitoring instrument. Woody Delp and the Facilities Department at LBNL designed the air handling system for the chamber. Darryl Dickerhoff, Nance Matson, and Dennis Dibartolomeo provided advice and assistance with the temperature monitoring system.